Improving Performance and Energy Efficiency of Blast Freezing Systems

by

Tyler R. Young

A thesis submitted in partial fulfillment of
the requirements for the degree of

Master of Science
(Mechanical Engineering)
at the

UNIVERSITY OF WISCONSIN–MADISON, 2023

Abstract

Blast Freezing is a common operation in the production of frozen food products. Blast freezing systems principally rely on high velocity low temperature air flowing over the product(s) to be frozen including meat, poultry, fish, bread, fruits, vegetables, and dairy products. For most products that are frozen, short freezing times are essential to maintain high product quality and short freezing times translate into higher energy intensity since low air temperatures and high air velocities are the means used to rapidly freeze products.

Within the U.S. alone, there are approximately 3,200 facilities that use some form of blast freezing which results in 143 trillion Btu and growing of electricity consumption annually. Dynamic blast freezers, specifically spiral blast freezers, are the focus of this project. In this form of blast freezing, food products enter a large, insulated enclosure (the blast freezer) on a conveyor that is configured to travel along a spiral path within the refrigerated enclosure. The belt speed is controlled to ensure the product exiting the freezer has achieved its target end temperature/state. Blast freezing systems utilize refrigerant-to-air evaporators to lower the air temperature within the freezing system's enclosure. The evaporators are then connected to a house refrigeration. Within the spiral freezer's enclosure, several high-powered fans recirculate air within the enclosure to remove heat more effectively from the food products being frozen. Achieving low air temperatures requires even lower refrigerant temperatures and low refrigerant temperatures translates to high energy intensity.

The goal of this research is to improve product throughput and energy efficiency of low temperature air blast freezing systems by increasing air flow over the product using strategically placed baffling components. The primary focus of this project is spiral blast freezers. Existing spiral freezing systems operating within four food processing facilities were modeled with computational fluid dynamics (CFD) to analyze their baseline airflow performance. The CFD models were validated with

experimental heat transfer coefficient data collected using an instrumented surrogate food product, called the “Phantom.” Air-side design changes that aim to improve air-side performance were envisioned and performance evaluated. Air-side design options predominantly relied on the use of baffles to more efficiently direct air flow within the enclosure. Proposed design options were analyzed with CFD, and airflow performance was compared against existing configurations. A 1-D transient product model and a system energy consumption model were used together to predict throughput capacity and product normalized energy consumption to quantify improvements from design modifications.

Table of Contents

List of Figures

List of Tables

Nomenclature

Roman Letters

$a_{0:N}$: N^{th} order polynomial fan curve fit coefficients

$A_{1:2}$: 2^{nd} order polynomial porosity curve-fit coefficients

A: Top surface area of the Phantom

A_c: Cross-sectional area of wall

ACH: Air changes per hour

A_{fan}: Area of fan surface

A_{flow}: Area available for flow

A_i: Area for i^{th} term

A_{open}: Area open for flow

A_s: Surface area of wall

A_{tot}: Total area

C_2: Inertial resistance term

c: Skin friction coefficient

$c_e(T)$: Temperature dependent effective specific heat

$Cf_{turb,i}$: Turbulent skin friction coefficient for i^{th} point

c_{ice}: Specific heat of ice

c_j: Specific heat of j^{th} macronutrient

$\bar{C}_l$: Intermediate Prandtl number coefficient

COP: Coefficient of performance

Cp_i: Specific heat for i^{th} point

C_{plant}: CO_2 concentration inside plant at time t

C_{spiral}: CO_2 concentration inside spiral at time t

$C_{spiral,0}$: Initial CO_2 concentration inside spiral

$C_{t,U}$: Coefficient for detached flow turbulent

c_w: Specific heat of water

D: Hole diameter

d_i: Effective hole diameter for i^{th} term

EF: Efficiency factor

E_{prod}: Product normalized energy consumption

$E_{prod,i}$: Product normalized energy consumption for i^{th} fan rpm

EPY: Yearly Emissions

f_c: Belt coverage fraction

g: Gravity

h: Convective heat transfer coefficient

$h_{C,i}$: Convection heat transfer coefficient for i^{th} point

$h_{FC,i}$: Forced convection heat transfer coefficient for i^{th} point

$h_{freezer}$: Specific enthalpy of air in freezer

h_i: Overall heat transfer coefficient for i^{th} point

$h_{L,i}$: Head loss for i^{th} term

$h_{NC,i}$: Natural convection heat transfer coefficient for i^{th} point

$h_{r,i}$: Radiative convection heat transfer coefficient for i^{th} point

h_{room}: Specific enthalpy of air in processing room

I: Current drawn

I_t: Turbulent intensity

k: Thermal conductivity of wall material

k_a: Thermal conductivity of air

K_i: Head loss coefficient for *i* th term

k_i: Thermal conductivity for *i* th point

$L_{a,i}$: Length of a side for *i* th term

$L_{b,i}$: Length of b side for *i* th term

L_{char}: Characteristic length

L_w: Latent heat of fusion for water

L_{wall}: Length of wall

m: Mass of product

$\dot{m}_{air}$: Mass flow rate of air

$\dot{m}_{frost}$: Mass generation rate of frost

M_j: Molecular weight of *j* th macronutrient

M_w: Molecular weight of water

N: Number of levels of belt

N_1: Number of elements in present mesh

N_2: Number of elements in succeeding mesh

N_{layers}: Number of inflation layers

$\dot{N}_{prod}$: Product throughput rate

$\dot{N}_{prod,base}$: Product throughput rate for base fan rpm

$\dot{N}_{prod_i}$: Product throughput rate for *i* th fan rpm

N_r: Number of radial elements

$Nu_{FC,i}$: Forced convection Nusselt number for *i* th point

$Nu_{horizontal}$: Nusselt number for a horizontal wall

Nu_i: Nusselt number for *i* th wall direction

Nu_l: Nusselt number for laminar region

$Nu_{lam,i}$: Laminar Nusselt number for *i* th point

$Nu_{lam,l,i}$: Lower transition laminar Nusselt number for *i* th point

$Nu_{NC,i}$: Natural convection Nusselt number for *i* th point

$Nu_{trans,i}$: Transitional Nusselt number for *i* th point

Nu_{ts}: Nusselt number for turbulent separation region

$Nu_{turb,i}$: Turbulent Nusselt number for *i* th point

$Nu_{vertical}$: Nusselt number for a vertical wall

N_y: Number of axial elements in Y-direction

P: Perimeter

PPY_{base}: Base level annual product throughput

Pr: Prandtl number

Pr_i: Prandtl number for *i* th point

$\dot{Q}$": Measured heat flux

$\dot{Q}_{belt\ motors}$: Heat load from belt motors

$\dot{Q}_{coils}$: Heat load removed by coils

$\dot{Q}_{fans}$: Heat load from fans

$\dot{Q}_{floor}$: Heat load from floor

$\dot{Q}_i$: Heat load from *i* th source

$\dot{Q}_{infiltration}$: Sensible and latent heat load from infiltration

$\dot{Q}_{motor}$: Heat load from motors

$\dot{Q}_{products}$: Heat load from products

$\dot{Q}_{transmission}$: Heat load from transmission

$\dot{Q}_{wall,i}$: Heat load from i^{th} wall

R: Universal gas constant

Ra: Rayleigh number

R_{cond}: Conductive thermal resistance

R_{conv}: Convective thermal resistance

Re: Reynold's number

Re_i: Reynold's number for i^{th} point

Re_l: Lower transition Reynold's Number

r_f: Refinement factor

rpm_{base}: Base fan rpm

rpm_i: i^{th} fan rpm

$R_{total,i}$: Total thermal resistance of i^{th} wall

S_j: Source term for j^{th} cartesian direction

T: Temperature

t: Time

$t_{dwell,base}$: Dwell time for base fan rpm

$t_{dwell,i}$: Dwell time for i^{th} fan rpm

T_{end}: Product ending temperature

$T_{film,i}$: Film temperature at i^{th} point

$T_{freezer}$: Temperature of freezer

th: Thickness of wall material

T_{if}: Transition temperature

T_{∞}: Ambient temperature

$T_{\infty,i}$: Ambient temperature at *i* th point

T_{room}: Temperature of processing room

T_s: Surface temperature

$T_{s,i}$: Surface temperature at *i* th point

T_{start}: Product starting temperature

t_{year}: Yearly operation time

u: Normal velocity

u_i: X-velocity for *i* th point

$\bar{u}_i$: Velocity magnitude for *i* th point

u_j: Velocity for *j* th cartesian direction

V: Voltage supplied

$\dot{V}_{base}$: Volumetric air flow rate of fans at base fan rpm

$\dot{V}_{fan}$: Volumetric air flow rate of fans

$V_{freezer}$: Gross internal volume of the freezer

$\dot{V}_{frost}$: Volumetric generation rate of frost

$\dot{V}_i$: Volumetric air flow rate of fans at *i* th fan rpm

v_i: Y-velocity for *i* th point

$\dot{V}_{infiltration}$: Volumetric flow rate of air infiltration

$\dot{W}$: Electrical power

$\dot{W}_{belt\ motors}$: Electrical power supplied to run the belt motors

$\dot{W}_{fans}$: Electrical power supplied to run the fans

$\dot{W}_{floor}$: Electrical power supplied to underfloor heating system

$\dot{W}_i$: Electrical power supplied to i^{th} source

w_i: Z-velocity for i^{th} point

$\dot{W}_{motor,e}$: Electrical power drawn by a motor

$\dot{W}_{\%,i}$: Percent share of total electrical power consumption of i^{th} source

$\dot{W}_{refrigeration\ system}$: Electrical power supplied to run the refrigeration system

$\dot{W}_s$: Shaft power of motor

$\dot{W}_{s,base}$: Shaft power at base fan rpm

$\dot{W}_{s,i}$: Shaft power at i^{th} fan rpm

$\dot{W}_{supplied}$: Electrical power supplied to run the blast freezer

$\dot{W}_{supplied,i}$: Electrical power supplied to run the blast freezer at i^{th} fan rpm

y^+: Non-dimensional cell position

$y^+{}_{initial}$: Initial non-dimensional cell position

$y^+{}_{req}$: Non-dimensional cell position requirement

x_1: First layer cell height

$x_{1,initial}$: Initial first layer cell height

X_{bw}: Mass fraction of bound water

X_j: Mass fraction of j^{th} macronutrient

X_{tw}: Mass fraction of total water

Greek Symbols

$\frac{1}{\alpha}$: Viscous resistance term

γ: Inflation layer growth rate

ΔP: Pressure drop

ΔP_c: Pressure drop from contraction

ΔP_e: Pressure drop from expansion

ΔP_i: Pressure drop for i^{th} term

Δn: Length of flow path

$\Delta U_{product}$: Change of internal energy of a product

Δx_v: Volume mesh size

ε: Emissivity

η_p: Electrical efficiency of the motor

μ: Viscosity

μ_i: Viscosity for i^{th} point

ρ: Density

$\rho_{freezer}$: Density of ice at freezer operating conditions

ρ_i: Density for i^{th} point

ρ_{room}: Density of air in processing room

σ: Stefan-Boltzmann Constant

σ_a: Open area fraction

ϕ: Freezer unoccupied fraction

ω_{room}: Humidity ratio of air in freezer

ω_{room}: Humidity ratio of air in processing room

Chapter 1 INTRODUCTION

1.1 Blast Freezing

One of the most widespread methods for rapid food product freezing is through the utilization of low-temperature blast freezing systems. These systems operate with product exposed to air temperatures ranging from 244 K to 233 K (-20 °F to -40 °F) to achieve product freezing times that vary from 10 to 60+ minutes, depending on the product and desired exit temperature. The cold air temperatures are generated by low temperature air-cooling evaporators connected to a vapor compression refrigeration cycle. There are several types of blast freezers, classified as either static or dynamic, based on whether the product remains stationary or moves inside the enclosure during the freezing process [1].

The work in this thesis is focused on one type of dynamic freezing system, the spiral freezer, which is a specific configuration of a blast freezing system that utilizes a spiral conveying system to minimize the required footprint. These blast freezers consist of a large, insulated enclosure in which cold air is circulated by high-power fans to rapidly freeze food products that can either be packaged or unpackaged. Figure (1.1) depicts an internal view of a dynamic spiral blast freezer, with insulated walls removed for improved visibility.

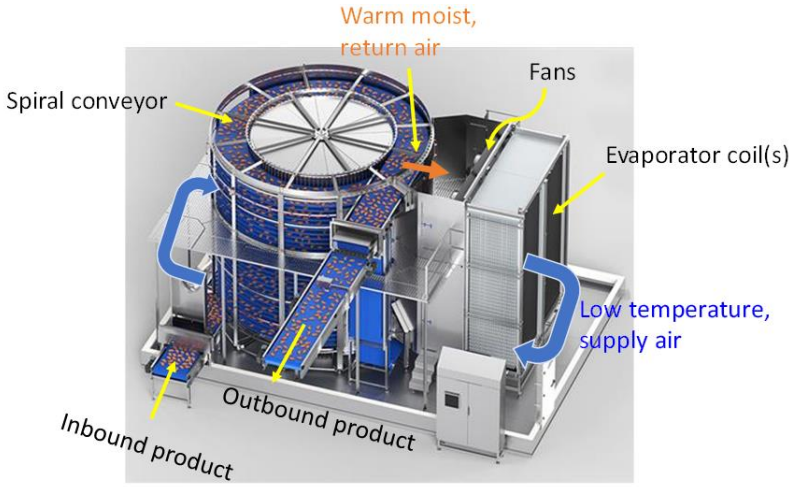

Figure (1.1): Inside look of a dynamic spiral blast freezer (insulated walls are omitted from the model). Adapted from GEA.

Within this blast freezer, warm products enter through an infeed conveyor located at the bottom left in Figure (1.1) and travels in a helical path on a spiral belt, exiting at an outfeed located near the top of the enclosure as shown in the upper middle of Figure (1.1). The air inside the blast freezer is continually flowing over the product at a high velocity to maximize the convective heat transfer coefficient on the surface of the product. During its dwell time within the blast freezing system, the high velocity low temperature air absorbs heat (and moisture for unpackaged products), which is transferred to the evaporator coils. Multiple fans are used to provide air circulation within the blast freezer's enclosure. The fans can be arranged in a pull-thru or push-thru configuration where the former places the fans on the leaving side of the evaporator coils and the latter places the fans on the entering side.

1.2 The Need for Improvement

Within the United States, the industrial sector is the second largest energy consumer, accounting for approximately 35% of end-use energy consumption, trailing closely behind the transportation sector [2]. The industrial sector's annual energy consumption has reached an astounding 33 quadrillion Btu and shows no signs of decline [3]. There are 15 subgroups classified within the industrial sector, shown in Figure (1.2), one of which is the food and beverage industry. Food and

beverage is the fourth largest energy consumer in the industrial sector, utilizing approximately 3,200 trillion Btu annually [4].

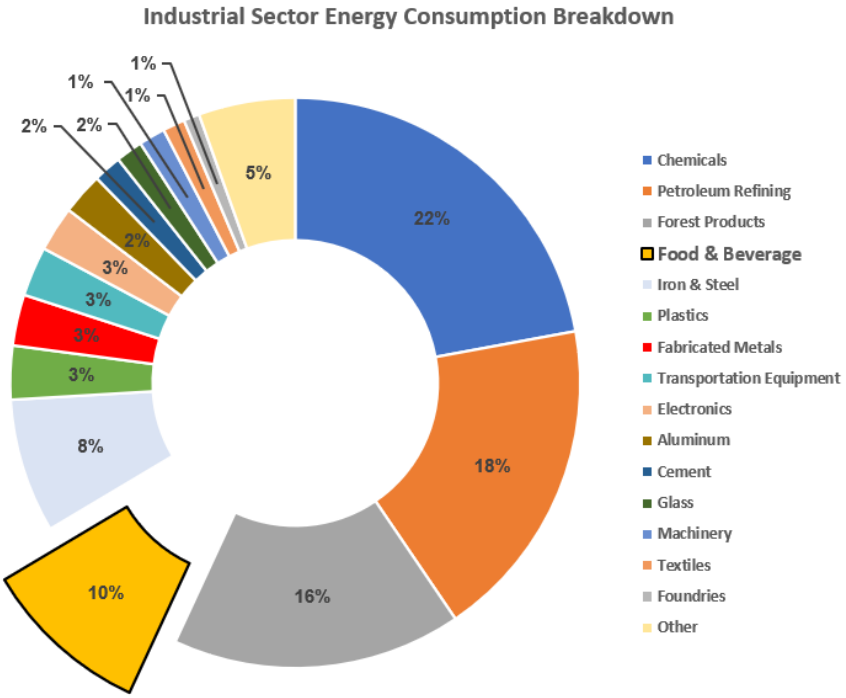

Figure (1.2): Breakdown of energy consumption within the industrial sector. Data from [4], graphic self-made.

Closer examination shows that nearly 40% of the energy utilized by the food industry is from onsite activities, as illustrated in Figure (1.3).

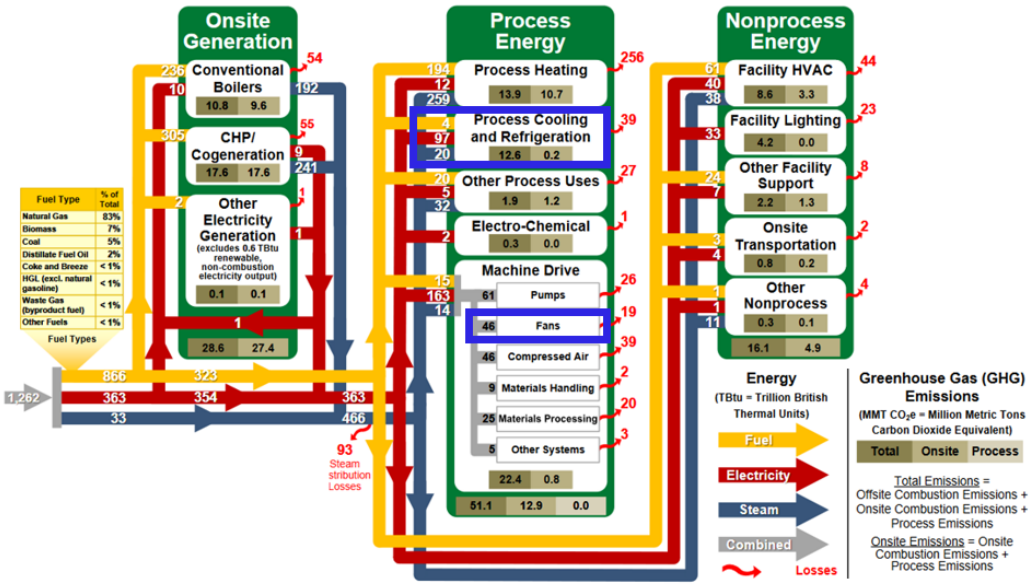

Figure (1.3): Energy breakdown of the Food and Beverage subsector [C]

This diagram highlights the energy roadmap for the food and beverage industry's onsite activities, with a focus on "Process Cooling and Refrigeration" and "Fans," which are highlighted as primary sources of energy consumption when operating blast freezers. Combined, these two end-uses constitute a staggering 11.3% of the total onsite energy consumption, resulting in an annual emission of 18.0 MMT CO_2e, which underscores the energy-intensive nature of the blast freezing process.

The specific energy demand and associated carbon emissions highlighted by the energy roadmap for blast freezing in the food and beverage industry have broader implications for global energy consumption and emissions. The food and beverage industry is a critical component to support and sustain an ever-increasing global population. The world's population surpassed 8 billion on November 15th, 2022, and the United Nations projects an additional 2 billion people by 2050 [5]. With a rapidly growing population, the food industry must increase its production capacity to meet the surging demand. Blast freezing is one strategy for maintaining high product quality and food safety, but it requires significant energy resources to support its operation. As evidenced by the findings in this research, there are real opportunities to improve the energy and thermal performance of the current

technologies used for blast freezing food products. Expanding the use of food freezing using existing blast freezing systems and technologies will perpetuate their inefficiencies and compound the consequences of a warming climate associated with a higher atmospheric CO_2 concentration, which is expected to increase 1.5℃ above pre-industrial levels by 2040 [6]. As such, efforts expended in this research aim to reduce the energy intensity of food freezing processes in order to support the industrial sector globally. Hence, the improvement in the efficiency and production capacity of blast freezing systems is not only a luxury resulting in reduced greenhouse gas emissions, but a necessity for the future health of the planet and its inhabitants.

1.3 Project Scope

This project, funded by the Environmental Protection Agency's Region 5, Pollution Prevention Grant 00E02908, aims to provide actionable strategies and approaches to enhance the energy efficiency and production capacity of low temperature blast freezing systems. The project includes evaluation of four blast freezing systems operating within four separate food processing facilities. A top-down analysis of each of the four plants' blast freezing systems seeks to provide tailored recommendations for specific changes that can be made to improve the energy and thermal performance of each blast freezing system. The 3D models in Figure (1.4) illustrate the four unique spiral blast freezers systems being investigated within this project.

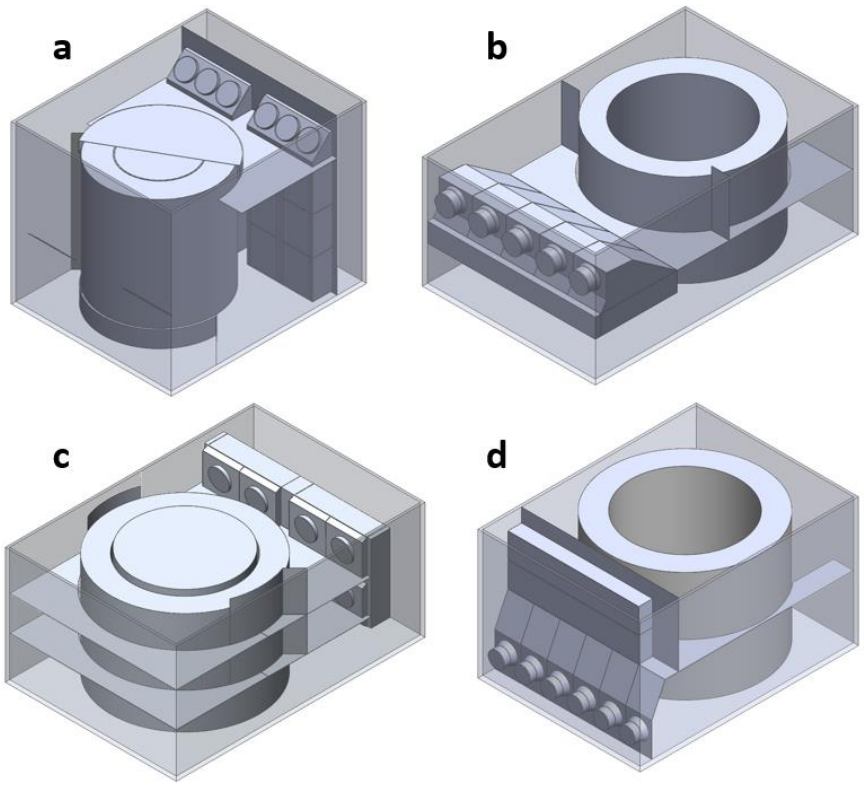

Figure (1.4): 3D models of the four freezers investigated in this project. a) Plant 1. b) Plant 2. c) Plant 3. d) Plant 4.

Despite all four plants utilizing dynamic spiral air blast freezing systems, the fundamental principles that underpin the recommended improvements included herein are applicable to other blast freezing systems as well and therefore are generally useful to the industry.

1.3.1 Objective

The objective of the project is to comprehensively evaluate all avenues for improving spiral blast freezing systems, with a particular emphasis on enhancing airside performance. The rationale for this emphasis will be expounded upon in **Section 2.3**. The research, centered on the analysis and improvement of airflow within these systems, will employ a multi-step approach. Five metrics will be initially established to quantify the performance of the four systems. Then, computational fluid dynamics (CFD) and energy balance models of the four existing blast freezers will be created to determine their base level performance. An experimental device will be developed and used to validate

the CFD models and energy balances; thereby, contributing to the confidence of the models' assumptions and simplifications. Design studies will be conducted using baffling additions to assess its impact on improving air-side flow and system performance and subsequently guiding design recommendations that are generally useful for spiral blast freezers. Finally, using insights garnered from the design studies, new blast freezer designs will be developed in order to maximize system performance.

1.3.2 Previous Work

Prior to initiating the preliminary work on this project, an investigation was conducted into existing research that has been performed on large industrial blast freezers commonly found in food processing facilities. The energy balance of a blast freezer, outlined in **Section 2.1**, indicates that the fans' combined parasitic heat and work load constitute almost half of a blast freezer's total energy consumption. Slowing down fan frequencies or using higher efficiency fans could reduce their contribution, but this approach also results in decreased air movement, leading to longer freezing times and decreased production capacity. On the other hand, increasing fan speed or fan power further exacerbates a blast freezer's energy consumption, as fan electrical power consumption increases with the cube of rotational speed. The only practical means to decrease electrical power consumption without adversely affecting production is to enhance the airflow inside the freezer, using the air movement provided by the fans more effectively. This assertion is corroborated by [7], wherein the authors applied airside modifications on a batch air blast freezer using strategic baffling and fan discharge vanes. With the modifications they were able to utilize smaller fan motors in conjunction with variable frequency drives to reduce fan power consumption from 8.7 kW to 4.0 kW. In another study researchers reduced ceiling-to-product clearance and added plywood sheets to prevent flow bypass in a batch blast freezer, resulting in higher average velocities, 15% shorter cooling times, and a 6% decrease

in fan power consumption [8]. Notably, these studies were limited to static batch freezers, and thus this work aims to expand their findings to dynamic spiral freezers, which are more widely used in food processing facilities.

The use of CFD in analyzing the design changes of a blast freezer offers a cost-effective and efficient solution compared to physical experimentation. CFD modeling also provides an opportunity to visualize the air flow patterns inside the freezer in order to identify features that enhance or hamper flow over the product, as well as features that can be added to better direct airflow. Nevertheless, modeling a full-scale blast freezer with CFD is a complex task that demands significant computational resources to achieve a high degree of accuracy due to the need for fine mesh sizes, especially in the presence of repeated small and intricate features. To make the computational problem tractable, the application of simplifications to the geometry is necessary. In this regard, one research group, [9], made initial progress in modeling a simplified spiral freezer. This study utilized a coupled flow-field and heat transfer simulation to model the airflow inside a 15-level spiral blast freezer containing pastry products. Each food item, based on its position along the spiral, was assigned a temperature in the model, as determined through physical data collection. The results obtained from the simulation offer a preliminary understanding of what the airflow inside a blast freezer might look like. The velocity data from the CFD model was compared against measurements captured by an anemometer and these results agreed to within 10%. While this study demonstrated promising results regarding the modeling and validation of CFD simulations for blast freezing systems, this current work aims to go further by developing baffling configurations that can enhance airflow performance, something these researchers did not investigate. New design configurations would alter the velocity inside the freezer and the system's pressure curve, therefore, the use of dynamic boundary conditions, like fan discharges that change with the changing velocity and system characteristics, is something that will be considered in this research .

1.3.3 Gaps in the Literature

The present state of research on the improvement of air blast freezers through physical experimentation or CFD analysis is still in the primary stages of progress. Some studies have focused on physical implementation of small baffling elements in static blast freezing systems, which consequently, may not be applicable to the dynamic blast freezing systems studied as part of the present research efforts. Conversely, prior CFD studies on dynamic spiral freezers did not provide concrete recommendations for enhancing production capacity and reducing energy consumption, as well as the accompanying dynamic boundary conditions. To address these gaps, this study aimed to use CFD to analyze the effects of strategic design modifications on airflow and energy consumption in spiral blast freezers and propose changes to improve system performance. This research builds on prior studies by utilizing fan curve data to dynamically account for varying system pressure drops associated with modified geometries. Additionally, a more robust modeling approach for the complex features of blast freezers was developed. The intention was to account for all complex components that may influence the flow fields, including evaporator coils, which have been overlooked in previous research.

1.3.4 Overview

The following sections of this thesis detail a comprehensive examination of the avenues for enhancing production and energy efficiency of blast freezing systems. In particular, **Chapter 2** provides an introductory energy balance case study on Plant 1's blast freezer to discern the sources of energy consumption that have the greatest potential for improvement. **Chapter 3** explains in detail the simplification methodology employed in the CFD models and justifies the chosen solver parameters. **Chapter 4** is dedicated to the validation of the CFD models utilizing both numerical and physical experimentation techniques. Furthermore, **Chapter 5** highlights the performance outcomes for the base models and proposed design modifications of the four plants, while **Chapter 6** explores prospective

new-build designs. Lastly, **Chapter 7** offers a concluding summary of the key findings and presents insightful recommendations for future research.

Chapter 2 INITIAL CASE STUDY

To determine the potential for improving freezing capacity and efficiency, an initial case study was conducted on Plant 1's spiral blast freezer. The objective of this study was to identify areas of improvement and to assess the applicability of any identified approaches to other types of blast freezing systems. In order to prioritize improvement efforts, the contributors to energy consumption were identified and their impact on system performance were evaluated.

2.1 Energy Balance

An energy balance was conducted on Plant 1's blast freezer, where the main contributors to energy consumption were identified and prioritized for further analysis. The balance was divided into two interdependent equations, one of which balanced the thermal loads removed by the refrigeration system, while the other considered the electrical energy supplied to power the necessary equipment. There are six main heat loads entering the freezer while in operation. **1)** The sensible heat removed from the product during its initial cooling and the latent heat removed during the freezing process. **2)** The heat generated from operating the fans used to circulate air. **3)** The heat generated from operating the motors used to drive the spiral's conveyor belt and belt-tensioning system. **4)** Sensible and latent heat from warm unwanted air infiltrating the freezer. **5)** Sensible heat due to transmission through the envelope of the enclosure. **6)** Heat gain through the floor of the blast freezer. Other sources of heat gain such as lighting loads within the blast freezer were omitted from the energy balance as their contributions are relatively small.

The refrigeration system plays a critical role in blast freezers by removing all heat loads entering the enclosure via the evaporator coils. This process requires an adequate supply of power to transfer heat energy out of the enclosure. The ratio of heat removed from the blast freezer to the electrical

power supplied to the refrigeration system is commonly referred to as the coefficient of performance (COP). The COP of the system depends on several factors such as the efficiency of the refrigeration components, compressor part-load operation, saturated suction temperature (pressure), and ambient conditions. Optimizing these parameters to provide the highest COP is essential for reducing energy consumption; however, the scope of this project is more narrowly focused on the blast freezer itself as a unit operation. The COP used for the energy balance of the blast freezers analyzed in this project are intended to be representative of the respective refrigeration systems under typical operating conditions. Figure (2.1) illustrates the various energy flows associated with blast freezers.

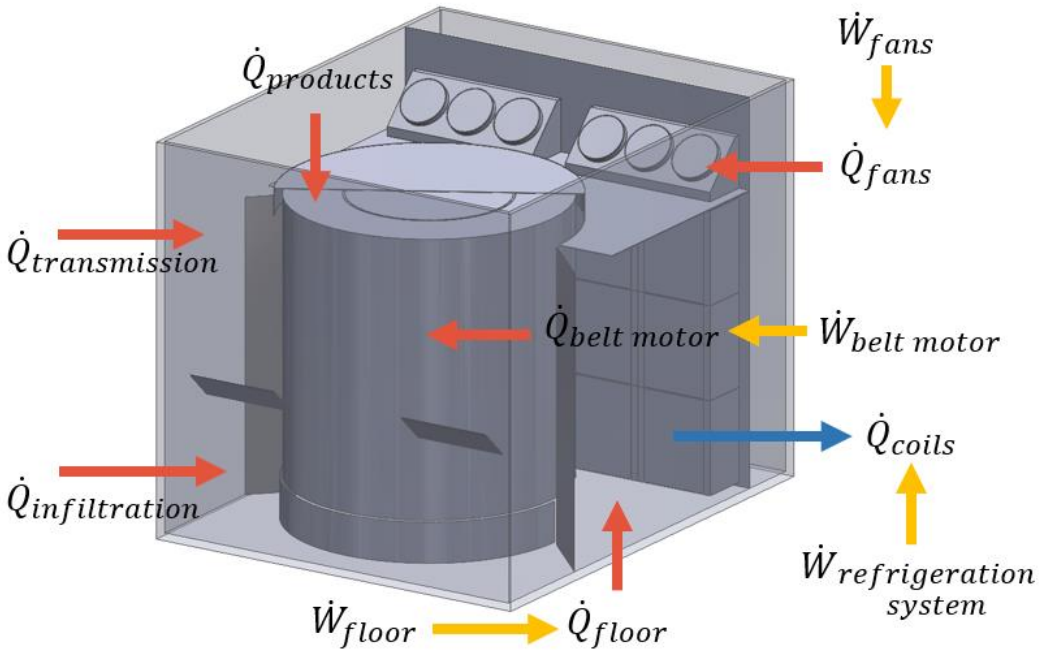

Figure (2.1): Energy balance conducted on sample blast freezing unit. Red arrows indicate heat entering the enclosure. The blue arrow represents heat removed from the enclosure. Orange arrows represent electricity required to power respective components.

The thermal and electrical energy balances are detailed in Equations (2-1) and (2-2) below,

$$\dot{Q}_{coils} = \dot{Q}_{products} + \dot{Q}_{fans} + \dot{Q}_{belt\ motors} + \dot{Q}_{infiltration} + \dot{Q}_{transmission} + \dot{Q}_{floor} \qquad (2\text{-}1)$$

$$\dot{W}_{supplied} = \dot{W}_{fans} + \dot{W}_{belt\ motors} + \dot{W}_{floor} + \dot{W}_{refrigeration\ system} \qquad (2\text{-}2)$$

where $\dot{W}_{supplied}$ is the total power supplied to the system to operate. A detailed explanation of how each of these terms were calculated follows.

2.1.1 Product Load

The rate of heat removed from the product is a function of the mass flow rate of products entering the freezer, $\dot{N}_{prod}$, and the difference in the internal energy of the product upon entering and exiting the blast freezer, $\Delta U_{product}$, as given by Equation (2-3).

$$\dot{Q}_{products} = \Delta U_{product}\, \dot{N}_{prod} \qquad (2\text{-}3)$$

In its simplest form, food products can be considered as a collection of individual components such as fats, carbohydrates, proteins, and water. Each of these macronutrients and water have their own temperature-dependent thermal properties. Therefore, an effective specific heat was used to represent the product. The effective property is summation of the individual macronutrient properties weighted by the mass fraction of each macronutrient. The products were assumed to be homogenous with isotropic properties. The effective specific heat for a given temperature, T, was calculated using Equation (2-4) below [10],

$$c_e(T) = \sum_j c_j X_j - [L_w + (c_w - c_{ice})T]\,(X_{tw} - X_{bw})\frac{T_{if}}{T^2} \qquad (2\text{-}4)$$

where c_j and X_j are the specific heats and mass fractions of the j^{th} macronutrient, L_w is the latent heat of fusion of water, X_{tw} and X_{bw} represents the mass fractions of total and bound water, and T_{if} is the temperature at which initial freezing occurs. The phase change of water in food products does often not occur at a single temperature but, rather, occurs over a temperature range. This temperature range is dependent upon the mass fraction compositions and the fraction of water solidified. The transition temperature, T_{if}, according to [10], can be calculated with Equation (2-5),

$$\frac{1}{T_{if}+273.15K}=\frac{1}{273.15K}-\frac{R}{M_w L_w}ln\left[\frac{(X_{tw}-X_{bw})/M_w}{(X_{tw}-X_{bw})/M_w+\sum_j\left(X_j/M_j\right)}\right] \quad (2\text{-}5)$$

where M_w and M_j represent the molecular weight of water and the j^{th} macronutrient, respectively. Using the temperature-dependent effective specific, $c_e(T)$, the change in product internal energy, $\Delta U_{product}$, can be predicted using Equation (2-6).

$$\Delta U_{product}=m\int_{T_{start}}^{T_{end}}c_e(T)dT \quad (2\text{-}6)$$

Table (2.1) below summarizes the relevant parameters for Plant 1's product load calculation.

Table (2.1): Product load parameters for Plant 1.

T_{start} [K]	T_{end} [K]	$\Delta U_{product}$ [J/prod]	Throughput [prod/min]	Dwell Time [min]
311	**261**	**133,932 (235,839 J/kg)**	**146.6 (83.25 kg/min)**	**26.5**

2.1.2 Fan and Belt Motor Loads

The circulating fans within the blast freezer and the drive belt motor are supplied with electrical energy. In most cases, the motors driving the fans and belt reside inside the blast freezer and, in this case, all of the electrical energy supplied becomes a thermal load on the evaporator. In some blast freezer designs, the electric motor driving the circulating fans resides outside of the freezer's enclosure. In this case, the thermal load within the blast freezer is reduced by the inefficiency of the electric motor. The electric motors in the blast freezers actually contribute twice to the overall energy balance; first as the electric power needed to run the fan and belt motors and then again as additional electric power required to operate the refrigeration system to remove the heat given off by these internal components. The heat given off by fans is dependent upon the power supplied to the motor and its location with

respect to the enclosure. The parasitic heat load for motors situated inside the enclosure were calculated using Equation (2-7),

$$\dot{Q}_{motor} = \dot{W}_{motor,e} = \frac{\dot{W}_s}{\eta_p} \tag{2-7}$$

where $\dot{W}_{motor,e}$ is the electrical power that the fan or belt motor is drawing, $\dot{W}_s$ is the shaft power required to operate the motor at a given condition, and η_p is the electrical efficiency of the motor. If the motor sits outside the enclosure, then the inefficiency of the electrical motor (1-η_p), is removed from Equation (2-7) and Equation (2-8) is then used for the parasitic heat load.

$$\dot{Q}_{motor} = \dot{W}_s \tag{2-8}$$

Plant 1's spiral freezer has six fan motors and one spiral belt drive motor all rated at 15 kW. Ammeters were used to determine the electrical current each motor was drawing. With the motors using 3-phase 480 V lines, the power draw was determined using Equation (2-9) and are shown in Table (2.2).

$$\dot{W}_{motor,e} = \sqrt{3}VI \tag{2-9}$$

where $\sqrt{3}V$ represents the RMS voltage supplied and I is the electrical current being drawn.

Table (2.2): Power consumption of Plant 1's six fans and single belt drive motor

Fan_1 [kW]	Fan_2 [kW]	Fan_3 [kW]	Fan_4 [kW]	Fan_5 [kW]	Fan_6 [kW]	Belt Motor [kW]
24.2	**23.8**	**22.2**	**23.8**	**23.2**	**22.9**	**23.3**

Slight differences in the power draw for each fan is noted and is likely due to variations in the static back-pressure associated with the fans being placed in different locations as well as physical construction. It is important to note that the power rating on the motor is dependent on the operating temperature. Lower temperatures allowed the motors to draw more power than their 15-kW rating.

2.1.3 Infiltration Load

Dynamic blast freezing systems require an opening to convey the products being frozen into and out of the freezing system. As such, these openings can inadvertently allow warm air from the plant to infiltrate the low temperature environment within the blast freezer. The underlying mechanisms that drive infiltration are affected by a combination of factors. Air can be entrained behind the product as it enters the freezer. If the infeed and outfeed are located in separate rooms or zones within the plant, a pressure imbalance can develop which will drive infiltration through the blast freezer. The rate of air entering the freezer can be quantified by the number of air changes per hour (ACH). An ACH of one means that every hour the entire internal volume of the blast freezer is replaced by outside air. Because the ambient air is warmer and more humid, infiltration puts parasitic sensible and latent load on the blast freezer. Plant air that infiltrates the blast freezer rapidly cools as it mixes with the much colder air within the freezer or when it makes contact with cold surfaces such as evaporator coils, support structures, or the frozen product being conveyed within the freezer. Water moisture that infiltrates the enclosure rapidly freezes forming ice crystals that precipitate out of the air stream or when impinging on solid surfaces. This results in frost building up on evaporator coils, fan guards, and product.

High infiltration rates and large temperature differences between the plant and the blast freezer can result in a significant parasitic heat load on the blast freezer. The summation of sensible and latent infiltration load can be calculated using Equations (2-10) and (2-11).

$$\dot{m}_{air} = V_{freezer}\ ACH\ \rho_{room}\ \phi \qquad (2\text{-}10)$$

$$\dot{Q}_{infiltration} = \dot{m}_{air}\left(h_{room} - h_{freezer}\right) \qquad (2\text{-}11)$$

where $V_{freezer}$ is the gross internal volume of the freezer, ρ_{room} is the density of the air within the plant where air infiltration originates, ϕ fraction of the freezer unoccupied by equipment, and h_{room} and

$h_{freezer}$ are the specific enthalpy of the air inside the plant room and blast freezer. In addition to determining the heat load infiltration adds, it is also important to calculate the volume of frost that accumulates every hour due to the infiltration, Equation (2-12) and Equation (2-13),

$$\dot{m}_{frost} = \dot{m}_{air}\left(\omega_{room} - \omega_{freezer}\right) \quad (2\text{-}12)$$

$$\dot{V}_{frost} = \frac{\dot{m}_{frost}}{\rho_{freezer}} \quad (2\text{-}13)$$

where ω_{room} and $\omega_{freezer}$ are the humidity ratio of the air inside the plant room and blast freezer, respectively, and $\rho_{freezer}$ is the density of frost formed at the freezer's operating temperature and pressure.

To determine the heat load and frost accumulation, temperature and humidity measurements were taken, and an infiltration test, which will be further detailed in **Section 2.3.1.1**, was conducted on Plant 1's spiral freezer; the results are summarized in Table (2.3).

Table (2.3): Temperature and relative humidities measurements and average infiltration test measurement for Plant 1's spiral freezer, measured in ACH.

T_{room} [K]	$T_{freezer}$ [K]	RH_{room}	$RH_{freezer}$	Avg. ACH	$\dot{Q}_{infiltration}$ [kWt]	$\dot{V}_{frost}$ [L/hr]
294	**241**	**0.74**	**0.95**	**2**	**56.11**	**30.22**

Plant 1's blast freezer had relatively high levels of infiltration, which can be seen in the amount of frost buildup inside the freezer, Figure (2.2).

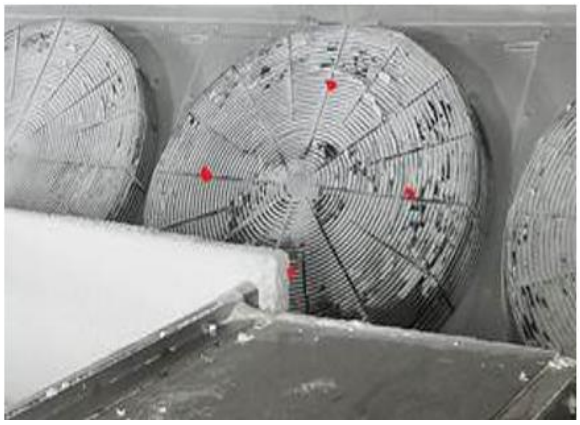

Figure (2.2): Frost accumulation seen on guards located at the outlet of the fans in the Plant 1's spiral freezer.

Frost buildup can cause considerable back pressure on the fans, translating into decreased air flow rates. Evaporator coils will also commonly experience similar levels of frost buildup while operating between successive evaporator coil defrost cycles. It is worth noting that frost buildup is not solely from moisture in the infiltrating air, but also from the moisture released by unpackaged products during the freezing process.

2.1.4 Transmission Load

While the walls of blast freezers are well insulated, heat from the warmer plant environment will be conducted into the freezer. The amount of heat that makes its way into the freezer is a function of the temperature difference between rooms and the material construction of the enclosure. A simple resistance network can be used to estimate the steady state transmission heat load, as seen in Figure (2.3).

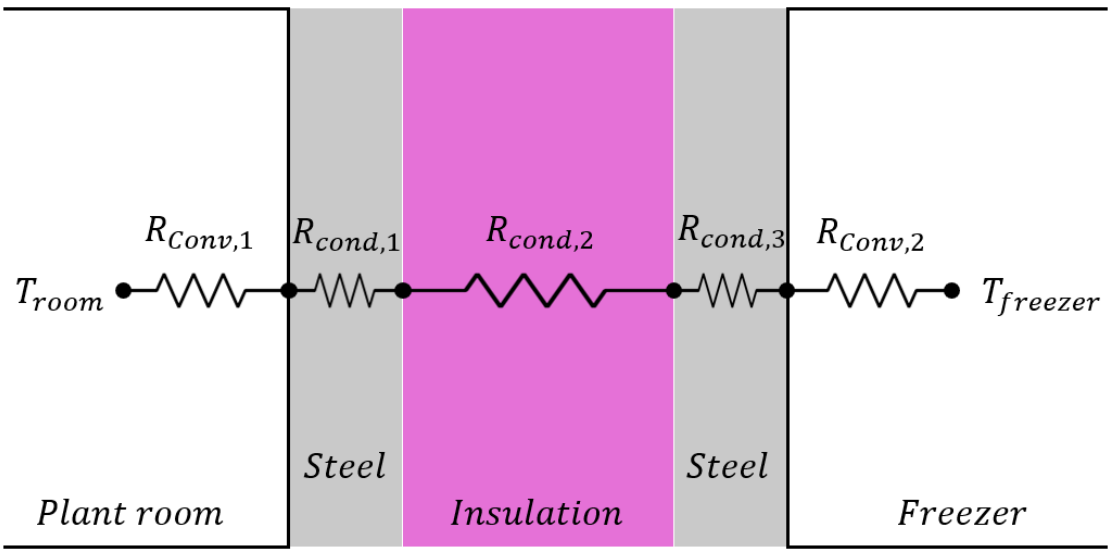

Figure (2.3): Resistance Network of a typical blaster freezer enclosure comprised of an insulated core sandwiched between two stainless steel sheets. Thicknesses are not-to-scale, image self-made.

The convection and conduction resistances can be calculated using Equations (2-14) and (2-15).

$$R_{conv} = \frac{1}{h\,A_s} \tag{2-14}$$

$$R_{cond} = \frac{th}{k\,A_c} \tag{2-15}$$

where h is the convective heat transfer coefficient, A_s is the surface area of the exposed wall, A_c is the cross-sectional area of the exposed wall, th and k are the thickness and conductivity of the different wall materials. It was assumed that there was natural convection on the exterior of the enclosure, and the heat transfer coefficients were calculated using Equations (2-16) and (2-22) for the vertical walls [11], and Equations (2-17) through (2-21) and (2-22) for horizontal walls [12].

$$Nu_{vertical} = \left[0.825 + 0.387\frac{Ra^{(1/6)}}{\left[\left(1+\frac{0.492}{Pr}\right)^{(9/16)}\right]^{(8/27)}}\right]^2 \tag{2-16}$$

$$\bar{C}_l = \frac{0.671}{\left[\left(1+\frac{0.492}{Pr}\right)^{(9/16)}\right]^{(4/9)}} \tag{2-17}$$

$$C_{t,U} = 0.14\left[\frac{1+0.0107\cdot Pr}{1+0.01\cdot Pr}\right] \quad (2\text{-}18)$$

$$Nu_l = \frac{1.4}{ln\left[1+\frac{1.4}{0.835\cdot \bar{C}_l\cdot Ra^{(1/3)}}\right]} \quad (2\text{-}19)$$

$$Nu_{ts} = C_{t,U}\cdot Ra^{(1/3)} \quad (2\text{-}20)$$

$$Nu_{horizontal} = \left(Nu_l{}^{10} + Nu_{ts}{}^{10}\right)^{(1/10)} \quad (2\text{-}21)$$

$$h = \frac{Nu_i\cdot k_a}{L_{wall}} \quad (2\text{-}22)$$

where Pr and Ra are the Prandtl and Rayleigh numbers, k_a is the thermal conductivity of air, L_{wall} is the length or height of the investigated wall, and Nu_i are the respective vertical or horizontal Nusselt numbers. $\bar{\mathrm{C}}_l$, $\mathrm{C}_{t,U}$, Nu_l, and Nu_{ts} are an intermediate Prandtl coefficient, coefficient of detached turbulent flow, and laminar and turbulent Nusselt numbers. The convection coefficient on interior surfaces was assumed to be 25 W/m^2-K as those were comparable to the convection coefficients later identified in **Section 4.2.2**. Table (2.4), below, details the thermal resistances of the side walls, as labeled in Figure (2.3), for Plant 1's insulated enclosure.

Table (2.4): Side wall thermal resistances of Plant 1's enclosure.

$R_{conv,1}$ [W/K]	$R_{cond,1}$ [W/K]	$R_{cond,2}$ [W/K]	$R_{cond,3}$ [W/K]	$R_{conv,2}$ [W/K]
3.396E-03	**1.665E-06**	**2.92E-02**	**1.665E-06**	**8.204E-03**

As expected, the thermal resistance of the insulated core is the largest inhibitor of heat transmission into the freezer. From the results of the resistance network the transmission heat loads from the sides and ceiling of the enclosure, and thereafter total load, were calculated using Equations (2-23) – (2-25),

$$R_{total,i} = \sum R_{conv,i} + \sum R_{cond,i} \quad (2\text{-}23)$$

$$\dot{Q}_{wall,i} = \frac{T_{room} - T_{freezer}}{R_{total,i}} \quad (2\text{-}24)$$

$$\dot{Q}_{transmission} = \sum \dot{Q}_{wall,i} \quad (2\text{-}25)$$

where "i" is the i^{th} distinct exposed wall. For example, Plant 1's enclosure was situated between two separate stories of the plant and operating at different temperatures. Therefore, in this case the vertical walls were split up and the values for A_s, A_c, and T_{room} were chosen accordingly.

2.1.5 Floor Load

Cold storage facilities that use low temperature freezing systems and cold storage rooms often rely on sub-floor heating systems to prevent ground heaving caused by freezing moisture in the ground. Despite its counterintuitive nature, underfloor heating is crucial for protecting the floor beneath the blast freezing system [13]. Failure to maintain appropriate ground temperature can result in heaving of the concrete floor and subsequent facility damage, which can cost millions of dollars in repairs. A resistance network is used to calculate the parasitic heat load from underfloor heating, taking into account the typical ground temperature, soil conductivity, and materials used for the freezer floor and foundation. The underfloor heating system itself can be comprised of resistance heating elements encased in conduit, air ducts, or glycol circulating in tubing under the blast freezer, and is inserted between layers of gravel above the bare ground. The design of the blast freezer, including insulation, concrete, and stainless-steel components, varies by manufacturer and installer. Figure (2.4) illustrates a generalized resistance network for a blast freezer.

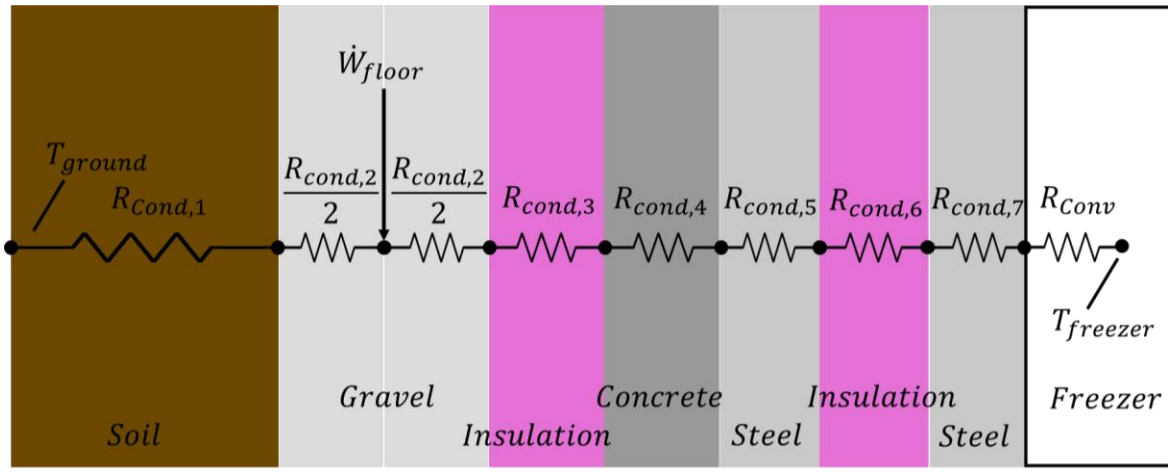

Figure (2.4): Underfloor heating resistance network of a typical blaster freezer enclosure (orientated horizontally).

where $\dot{W}_{floor}$ is the power supplied to the heaters, assuming they are resistive. Once each of the thermal resistances have been determined, Equations (2-23) through (2-25) can be used again to predict the underfloor heat entering the freezer.

2.1.6 Energy Consumption Breakdown

Using the information collected from Plant 1's spiral freezer and the methods described to determine each of the heat load components, a program was developed to solve the overall energy balance and calculate the electrical power required to operate the blast freezer, $\dot{W}_{supplied}$. The results shown here are specific to Plant 1; however, the program was designed to be flexible and is therefore useful to analyze any blast freezing system. Table (2.5) and Table (2.6) below summarize the thermal and electrical loads for Plant 1's system. The COP of Plant 1's refrigeration system is estimated at 1.675.

Table (2.5): Heat loads entering Plant 1's spiral blast freezer. Negative values represent heat removed from the freezer. Values shown in kWt.

$\dot{Q}_{products}$	$\dot{Q}_{fans}$	$\dot{Q}_{belt\ motors}$	$\dot{Q}_{infiltration}$	$\dot{Q}_{transmission}$	$\dot{Q}_{floor}$	$\dot{Q}_{coils}$
337.07	**151.23**	**18.74**	**56.11**	**5.13**	**1.67**	**-569.94**

Table (2.6): Electrical loads required to power Plant 1's spiral blast freezer. Values shown in kWe.

$\dot{W}_{fans}$	$\dot{W}_{belt\ motors}$	$\dot{W}_{floor}$	$\dot{W}_{refrigeration\ system}$	$\dot{W}_{supplied}$
180.03	**23.28**	**2.00**	**340.33**	**545.64**

From the tables, one can begin to see where the bulk of the energy consumption comes from. Each of the six terms' individual contributions to $\dot{W}_{supplied}$ were calculated to give an energy consumption breakdown using Equation (2-26).

$$\dot{W}_{\%,i} = \frac{\frac{\dot{Q}_i}{COP} + \dot{W}_i}{\dot{W}_{supplied}} 100\% \qquad (2\text{-}26)$$

Products, infiltration, and transmission have no associated $\dot{W}$ term, as they are only contributing a heat load. The breakdown of energy consumption is summarized in Table (2.7).

Table (2.7): The energy consumption breakdown. Represents each terms' percentage to the overall required power.

Products	Fans	Belt Motors	Infiltration	Transmission	Floor
36.9%	**49.5%**	**6.3%**	**6.1%**	**0.6%**	**0.6%**

Upon observing the data presented in the table, one may be surprised to discover that fans make up half of the entire energy consumption. In perspective, the amount of energy expended to operate the fans and remove the heat they generate surpasses the energy consumption required to freeze the product by 34%. Interestingly, the contributions made by the transmission and floor elements towards the overall energy consumption are relatively negligible. This outcome can be attributed to the well-insulated construction of the enclosures. While the percentages outlined in this analysis are specific to Plant 1's freezer, they can be reasonably extrapolated to apply to a standard blast freezer. Therefore, the findings of this study provide valuable insight into how the energy efficiency of these systems can be enhanced by focusing on attacking the largest components.

2.2 Load Components Omitted from Further Investigation

In the interest of improving the overall efficiency of the blast freezer, certain components of the freezer load have been excluded from further investigation. These components include floor heat gain, transmission heat gain through walls and ceiling, product load, and belt motor load. Reducing floor, transmission, and belt motor load were deemed unworthy of investigation, while reducing product load was not thoroughly investigated within the scope of this project.

Both floor and transmission heat loads have a relatively minor contribution to the overall thermal load imparted on the blast freezer. Hence, any substantial improvements made to either of these terms would have a negligible effect on the system's overall energy consumption. For instance, doubling the amount of insulation used in Plant 1 could decrease the transmission load from 5.1 kW to 2.7 kW, resulting in a mere 0.27% reduction in overall energy consumption.

Spiral belt and belt-tensioning motors do result in a meaningful contribution to the internal heat load in a blast freezer. Selecting a higher efficiency motor would result in a slight decrease in parasitic load. Additionally, altering the speed at which the belt operates reduces the mechanical load and thereby power of the motor. However, modifying the belt speed affects the freezing process and the amount of product that a single blast freezer can manage. As such, further investigation into reducing heat and power loads associated with belt motors was not considered.

Another approach to reducing the overall energy consumption of a blast freezer is to modify the food product manufacturing process. For instance, if a cooked product is being frozen, adjusting the time between the cooking and freezing processes can enable the warm and moist product to cool down before entering the spiral freezer. While this can effectively limit the load on the system and minimize frost accumulation on surfaces, modifications to the production process were not within the view of this project's scope.

2.3 Load Components to Consider

In order to achieve efficiency gains, the primary focus of the present research was on reducing the fan load, and to a lesser extent, the infiltration load. These two components were further analyzed to identify potential opportunities for improvement, as they were found to be the most significant and manageable contributors to the overall energy balance.

2.3.1 Infiltration

In a dynamic blast freezer, complete elimination of infiltration is infeasible. The warmer plant air will inevitably find its way into the freezer, either entrained with the entering product or due to pressure imbalances between adjacent rooms. Nevertheless, there are methods to reduce infiltration, and the first step is to identify the extent of infiltration and its entry points. Infiltration tests were conducted at all four plants, which yielded valuable insights into the strategies and equipment that each plant was using to mitigate infiltration.

2.3.1.1 Facility Measurements

The infiltration tests used CO_2 as the tracer gas to determine the rate that plant air entered the freezer. A large cannister of CO_2 gas was opened and allowed to slowly empty inside the freezer while two sensors connected to data loggers monitored the now higher CO_2 concentration within the freezer and the plant background concentration. Figure (2.5) below shows the equipment used for the infiltration test.

Figure (2.5): Equipment used to conduct onsite infiltration tests.

Once the concentration inside the freezer reached a level considerably higher than what was recorded outside, the CO_2 cannister was closed and removed. Data were collected every 60 s for approximately an hour, while the spiral freezer operated as normal. The rate of CO_2 concentration decay over time is proportional to the air infiltration rate. Using the concentration data collected and Equations (2-27) and (2-28), the infiltration rate, ACH, could be calculated according to:

$$\dot{V}_{infiltration} = \frac{V_{freezer}\,\phi}{t} ln\left[\frac{C_{spiral,0}-C_{plant}}{C_{spiral}-C_{plant}}\right] \quad (2\text{-}27)$$

$$ACH = \dot{V}_{infiltration}\frac{60min}{V_{spiral}} \quad (2\text{-}28)$$

where $C_{spiral,0}$, C_{spiral}, and C_{plant} are the CO_2 concentrations of the spiral at time 0, time t, and the plant at time t, respectively. Figure (2.6) shows the calculated ACH over the duration of infiltration test that was initially performed on Plant 1's spiral freezer.

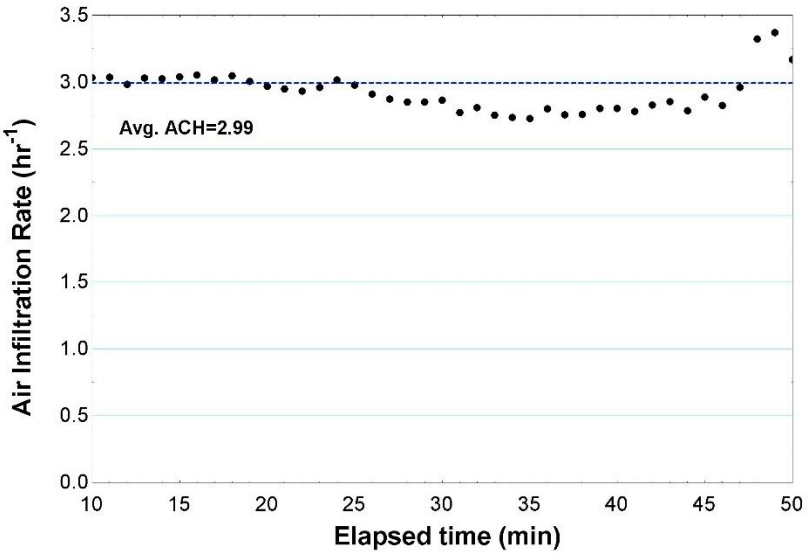

Figure (2.6): ACH vs. time from Infiltration test. Data gathered from Plant 1's freezer.

Data at the beginning of the test (i.e., less than 10 minutes) are ignored as the CO_2 concentration is initially equilibrating inside the freezer. The remaining data can be curve-fit to provide an average ACH. According to [14], an infiltration rate in excess of 1.25 for blast freezers is considered poor. Plant 1's initial ACH of approximately 3 was well above this value and therefore required further investigation. The infeed and outfeeds for this specific spiral are located in two different processing rooms. Pressure measurements within each room showed that infiltration into the spiral was likely the result of pressure driven flows. It was later determined that the plant's pressure imbalance was due to make-up air units positively pressurizing the zone where product was entering the blast freezer relative to the zone where product was exiting. In addition, there were doors in areas adjacent to the zone where the product exited the blast freezer that exacerbated zone air pressure imbalances. Pressure differences between infeeds is a common problem in which blast freezer manufacturers will use an Automatic Pressurization System (APS) which attempts to balance the pressure between the freezer and the adjacent rooms. Plant 1's freezer did have an APS; however, it was shut off at the time of the first infiltration test. Three additional infiltration tests were conducted to determine the effectiveness of the APS system while closing all doors previously left open, as shown in Figure (2.7).

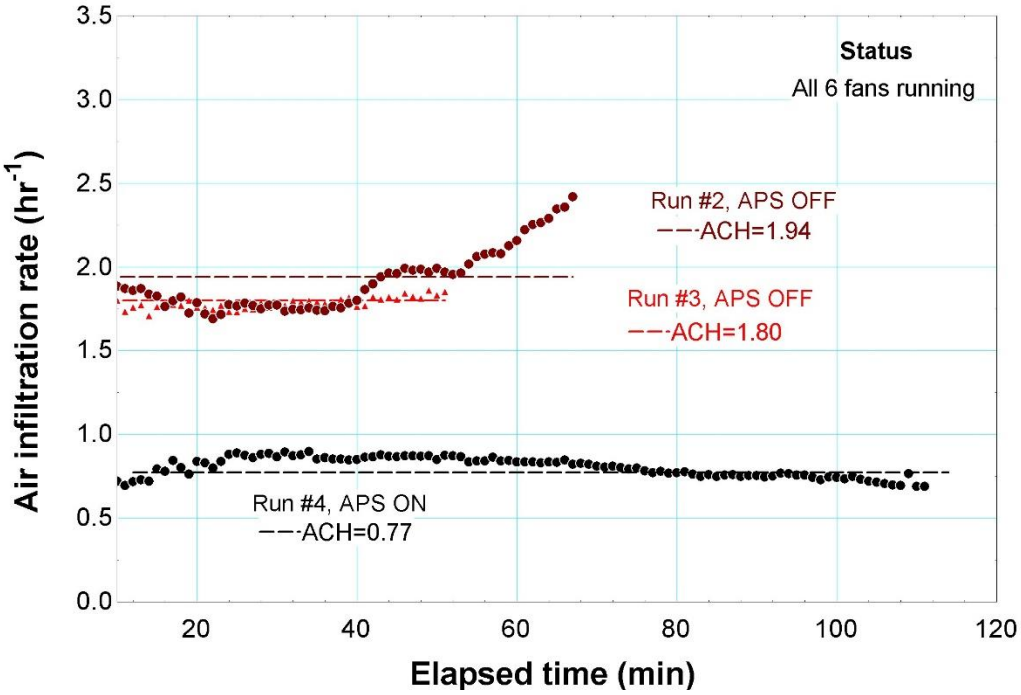

Figure (2.7): Infiltration experiment testing APS system and plant pressure imbalance.

While infiltration was still substantial in runs 2 and 3, closing the processing room doors to reduce pressure imbalances resulted in a 35%+ reduction in air infiltration relative to the original test. With the APS system on and the doors closed, infiltration was reduced by approximately 75%.

Infiltration tests were also performed on Plant 2, 3, and 4's blast freezers. At least two runs were completed on each freezer, and more were conducted when results needed confirmation. Table (2.8) summarizes the results of all infiltration tests conducted at each plant.

Table (2.8): Infiltration tests conducted at Plants 1 through 4.

Infiltration Rate ACH [1/hr]					
Plant	**Run 1**	**Run 2**	**Run 3**	**Run 4**	**Run 5**
1	**2.99**	**1.94**	**1.8**	**0.77**	**0.66**
2	**0.41**	**0.38**	**-**	**-**	**-**
3	**0.08 (Up-runner)**	**0.54 (Down-runner)**	**0.13 (Up-runner)**	**0.20 (Down-runner)**	**-**
4	**0.75**	**0.79**	**-**	**-**	**-**

Plant 4 has what is considered to be “good” levels of infiltration [14]. Plants 2 and 3 are considered “excellent”, with Plant 3 specifically having some of the lowest levels of infiltration that the research team had ever observed. Because Plants 2 through 4 had such low levels of infiltration, no further investigation into infiltration mitigation strategies was pursued.

2.3.1.2 Best Practices for Minimizing Infiltration

As seen by the findings from Plant 1’s infiltration study, reducing the amount of unwanted air entering a blast freezer can often be a simple solution for energy reduction. It is recommended that facilities take pressure measurements within the rooms that are adjacent to their freezers when the infeed and outfeed are in physically segregated zones of the plant. This will determine whether infiltration into the blast freezer is being driven by zone air pressure imbalances. If a significant difference is observed, then zone pressures should be balanced. Minimizing the size of the opening of the infeed/outfeed will also reduce the net area for infiltrating air to flow, disrupting the air entrained by entering and exiting product. Therefore, it is recommended that openings should be sized for a minimal clearance above the maximum expected product height.

2.3.2 Fan Load

Reducing the fan load can be done in several ways including: the use of more efficient fans, slowing the fans down, improving the air flow patterns so the fans are more effectively cooling the product, or any combination of the three. The former, similar to non-fan motors, falls under the category of improvements that are not being investigated under the scope of this project. Nonetheless, any improvement of the fan’s mechanical and or electrical efficiency would result in a two-fold benefit as less electricity is consumed and therefore less heat is produced inside the enclosure.

2.3.2.1 Effect of Lowering Fan Speed

Fans with variable frequency drives (VFDs) are able to adjust their speed to produce variable flow rates. VFDs allow for more flexible operation as the flow can be modulated depending upon need, adding a boost in energy efficiency. It was hypothesized that adjusting fan speed could potentially lead to a performance increase. A parametric study was conducted using the energy balance model to determine how performance was affected by changing fan speeds. Using the fan affinity laws [15], Equations (2-29) and (2-30), and an approximate relationship between velocity and throughput, Equations (2-31) and (2-32), a link between rpm, shaft power, product throughput, and dwell time was derived.

$$\dot{V}_i = \frac{rpm_i}{rpm_{base}}\ \dot{V}_{base} \tag{2-29}$$

$$\dot{W}_{s,i} = \left(\frac{rpm_i}{rpm_{base}}\right)^3\ \dot{W}_{s,base} \tag{2-30}$$

$$\dot{N}_{prod_i} = \left(\frac{\dot{V}_i}{\dot{V}_{base}}\right)^{0.8}\ \dot{N}_{prod_{base}} \tag{2-31}$$

$$t_{dwell,i} = \frac{\dot{N}_{prod_{base}}}{\dot{N}_{prod_i}}\ t_{dwell,base} \tag{2-32}$$

Here $\dot{V}$ is the volumetric flow rate produced by the fans, the subscript "base" represents the values of Plant 1's existing conditions and "i" represents the i^{th} different value of rpm_i. In Equation (2-31), it was assumed that a linear relationship existed between volumetric flow rate and the velocity that the product observes. The heat transfer coefficient for flow over a flat plate (and other similar objects) approximately scales with velocity to the 0.8$^{\text{th}}$ power [16], therefore an increase in flow rate and subsequently velocity, would result in greater throughput capacity. Fan speed was varied from base operating speed, 1750 rpm, to 875 rpm. The value of each speed's product normalized energy

consumption, as fully defined in **Section 5.1.4**, was calculated using Equation (2-33) and plotted as a function of rpm.

$$E_{prod,i} = \frac{\dot{W}_{supplied,i}}{\dot{N}_{prod,i}} \qquad (2\text{-}33)$$

Product throughput and dwell time were also plotted as a function of fan speed.

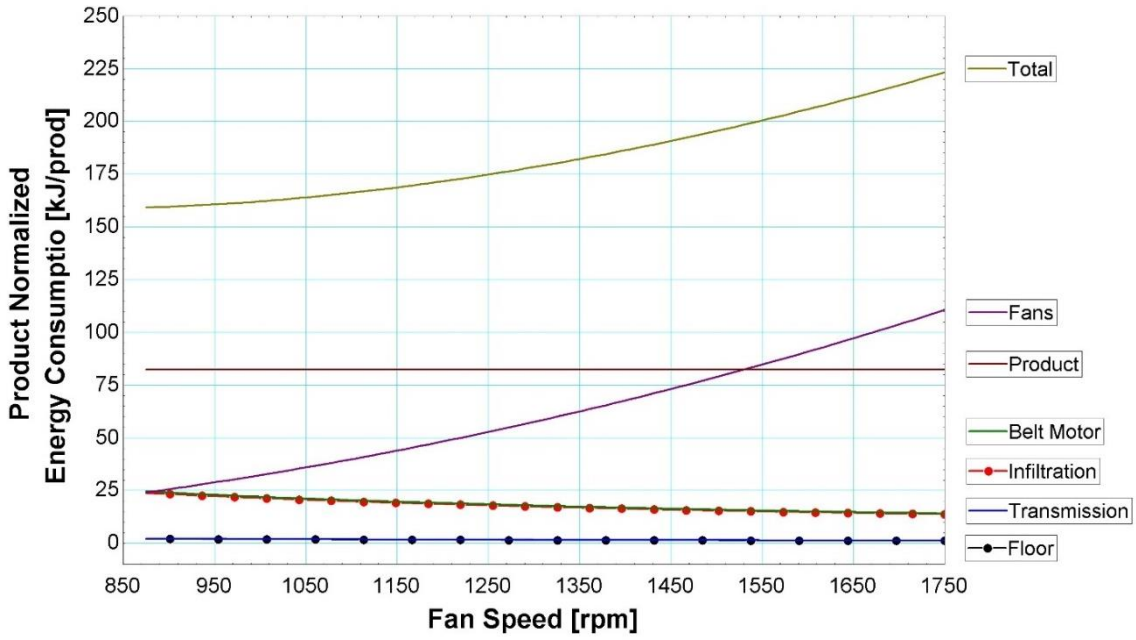

Figure (2.8): Product normalized energy consumption for each contributor plotted vs fan speed.

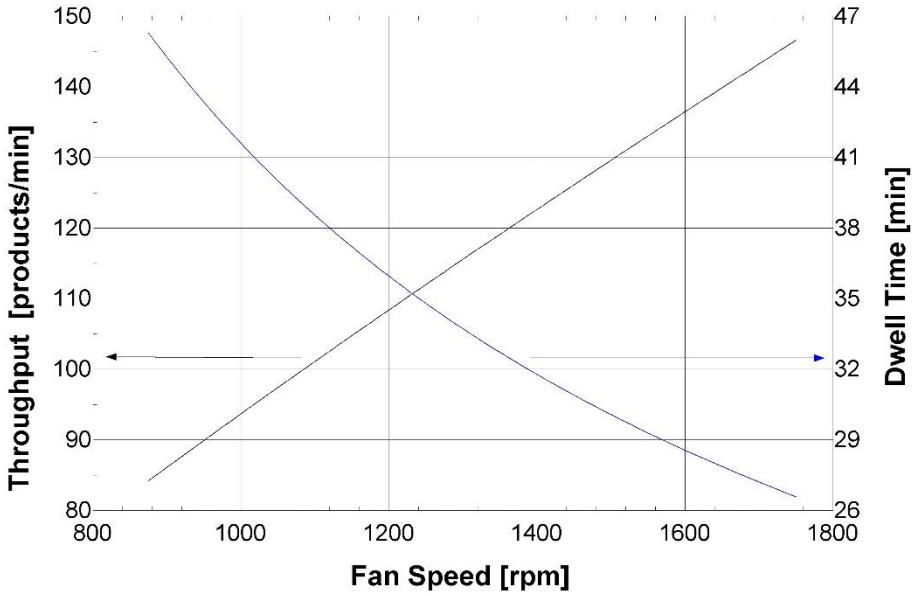

Figure (2.9): Product throughput and dwell time vs fan speed.

The load from belt motors, infiltration, transmission, and floor heating were assumed to be unaffected by throughput. Therefore, as throughput decreased with fan speed, the per product energy consumption increased as seen in Figure (2.8). More importantly, reducing the fan speed results in a significant decrease in the energy they use, bringing down total consumption as well. Unfortunately, as shown by Figure (2.9), we see more than a 40% reduction in product throughput due to the airflow being cut in half. The Food and Agriculture Organizations predicts that by the year 2050 food production will need to increase by 60 percent to accommodate the growing population [17]. As such, food processing plants are looking to maximize product throughput. While slowing down the fans may enhance energy efficiency, it comes at the cost of reduced processing capacity, rendering it an unsatisfactory solution to the issue at hand.

2.3.2.2 Increasing Fan's Utilization

Improving the fan's effectiveness by better utilizing produced airflow in blast freezers presents a significant opportunity for energy savings. Fans play a crucial role in facilitating heat transfer between the warm product and cold refrigerant by generating airflow. Improving airflow over the product leads to faster cooling rates, allowing for more product to be processed in a shorter time period, ultimately reducing the overall energy consumption of the system. One promising approach to enhancing airflow is to modify the blast freezer's geometry. This concept, similar to the use of baffles in shell and tube heat exchangers, can be employed to improve heat transfer in blast freezers. By leveraging full-scale CFD models, it is possible to assess the current airflow performance and identify areas for improvement. Through this approach, companies can maximize their product throughput while minimizing energy consumption, contributing to sustainable and efficient food processing practices.

Chapter 3 MODELING BLAST FREEZERS WITH CFD

Modeling a spiral blast freezer using computational fluid dynamics (CFD) is a daunting task that demands careful choice of assumptions and simplifications. The complex geometry of the freezer is due, in part, to the significant range of length scales that must be resolved over the entirety of the flow field. For example, the enclosure of a blast freezer can be several thousand cubic feet in internal volume with finer details such as the spacing of fins in air-cooling evaporators measured in tenths of an inch. Beyond fins in the evaporators, blast freezing systems have millions of small features, each of which influences the flow field. Therefore, the cumulative effect of all features on the flow within the enclosure need to be considered. Because computational expense increases exponentially with the number of elements, it is infeasible to model the small individual features in the same simulation as the entire freezer; this approach would require hundreds of billions of elements. Therefore, simplifications of the geometry within the computational domain are required to make the problem tractable while balancing complexity and computational cost. This chapter outlines the simplifications made and the assumptions involved, as well as the construction, meshing, solving, and analysis process of the CFD models used to simulate blast freezing systems.

3.1 3D Modeling of Spiral Blast Freezers

In order to conduct a CFD simulation, it is necessary to define a computational domain. As the investigation of the whole flow field inside the freezer is of interest, the interior of the enclosure walls serves as the domain's boundary. All the components located inside the enclosure contribute to shaping the computational volume.

To decrease the computational cost of running a CFD simulation for a blast freezer, simplifications were necessary for the geometry. Two types of simplifications were implemented:

physical components were either excluded from the model or represented using porous media modeling techniques. If an object inside the freezer was anticipated to have minimal impact on the flow or would overly complicate the geometry, it was removed from the 3D model. Examples of omitted objects include stairways, ladders, small structural elements, refrigeration lines, lights, and safety wiring. These components were regarded as insignificant flow disruptors since their surface areas were relatively small.

Components that were deemed vital for accurately modeling the flow, such as the evaporator coils, spirals, fans, walkways, and baffling, were included in the model. However, due to their intricate design it is impossible to resolve each separate flow channel. Therefore, these components were modeled using a simplified, porous media modeling technique. For example, the evaporator coils, which contain multiple rows of tubing with thousands of fins, were represented by porous rectangular prisms, as illustrated in Figure (3.1).

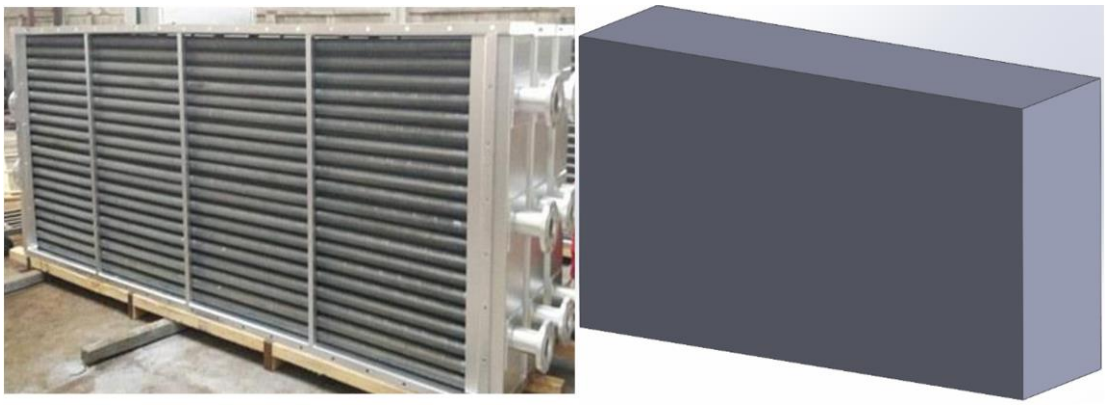

Figure (3.1): Industrial fin-on-tube evaporator coil (left), simplified coil (right). From VRCooler (left).

The spiral belt, which contains N levels in a helical pattern, typically 30 to 40 levels, was modeled as a porous annulus, as seen in Figure (3.2).

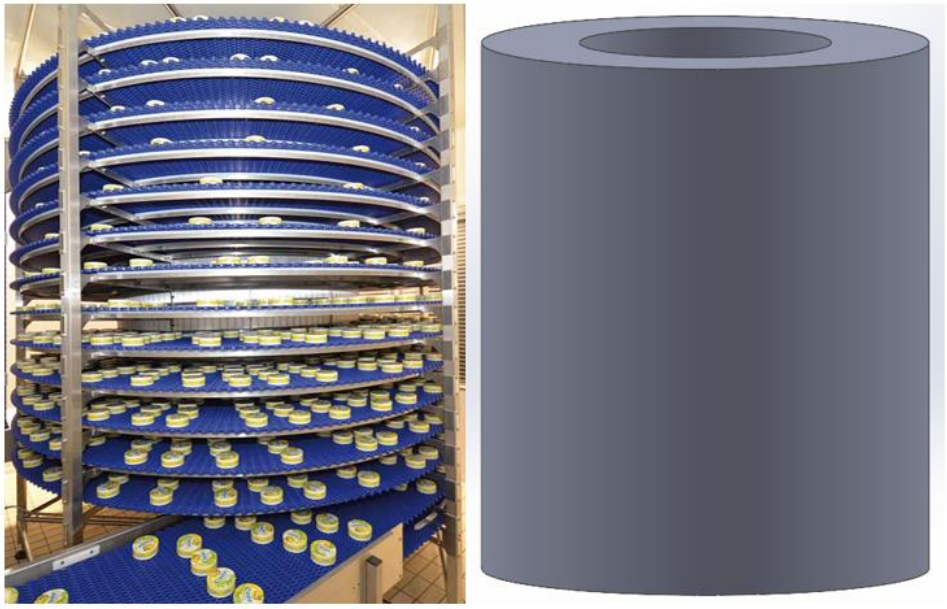

Figure (3.2): Small-scale spiral belt (left), simplified spiral (right). From Standard Tech (left).

The belt shown in Figure (3.2) is a nylon belt made of interlocking sections. This type of belt along with stainless steel belts are the two most commonly used varieties. A closer look at the belt's interlocking mesh can be seen below.

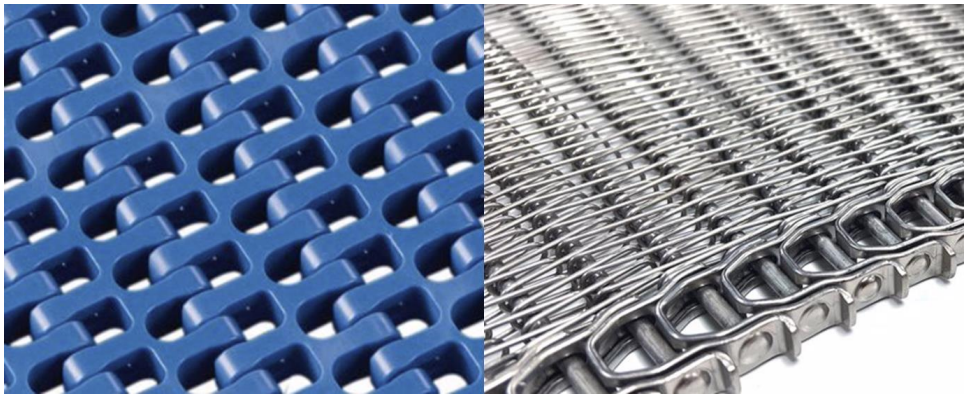

Figure (3.3): Close up view of two commonly used belt materials, nylon (left) and stainless steel (right). From Ashworth.

Both of the designs' interlocking pieces allow the belt to expand tangentially to conform to the curved spiral structure. Additionally, some spirals will have a support structure at the interior radius made of tightly packed vertical bars. Such structures will cause a significant disruption to flow and were therefore modeled. The support structures were simplified as a thin, porous annulus, as seen in Figure (3.4).

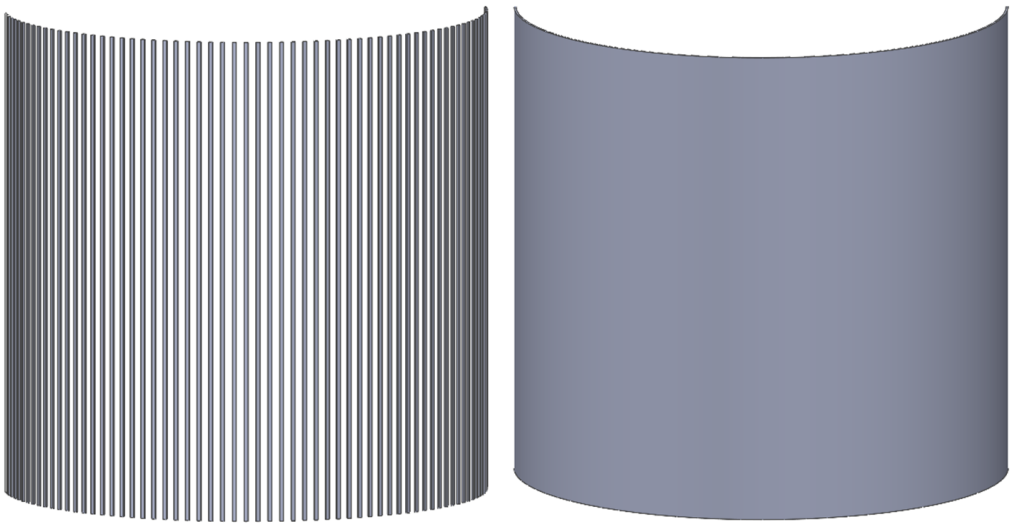

Figure (3.4): 3D model representation of spiral support structure (left), simplified structure (right), section view shown.

The support structure sits coincident with the interior radius of the simplified spiral annulus in Figure (3.2).

The fans used to circulate freezing air inside the freezer are either axial fans or centrifugal plug fans. In the simulation, these were modeled without resolving the rotating fan blades or centrifugal vanes; rather, they were modeled in a manner that captured the fan's general shape and provided a volumetric flow rate and velocity normal to the fan's discharge surface that was consistent with the measured performance of the fan, as given by its fan curve. Two 3D components were used to model each fan: an enclosure and a volume. The enclosure component represents the solid walls of the fan's geometry while the volume component represents the free space within the fan where air can flow. It was necessary to identify a volume inside the fan distinct from the remaining volume of the freezer to create a surface on the outlet of the fan, as further explained in **Section 3.2.2.2**. An example of a simple centrifugal plug fan and its corresponding enclosure can be seen in Figure (3.5). A similar process was used for the blast freezing systems using axial fans.

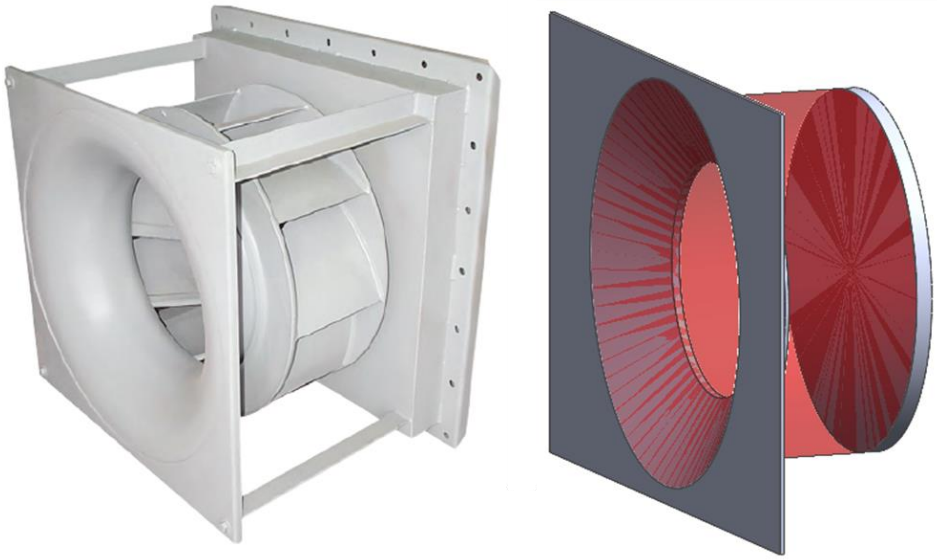

Figure (3.5): Centrifugal plug fan (left) and modeled two component simplified fan (right). Fan enclosure (grey) and volume (transparent red). From Twin City Fan (left).

Walkways and baffling components needed minimal simplification. Walkways, whether physically solid or perforated, were modeled as thin structures that were either porous or solid, with supports being omitted from the model. Similarly, baffling components were simplified by removing any fasteners, supports or welds that held them in place.

The 3D models of the freezers were created using SolidWorks® modeling software, with the shape and location of all components determined from the blast freezer manufacturers' drawings. Additional measurements were taken on-site for dimensions that were not detailed in the drawings. Figure (3.6), shows Plant 1's fully-simplified spiral blast freezer 3D model used as the computational domain of the CFD simulation.

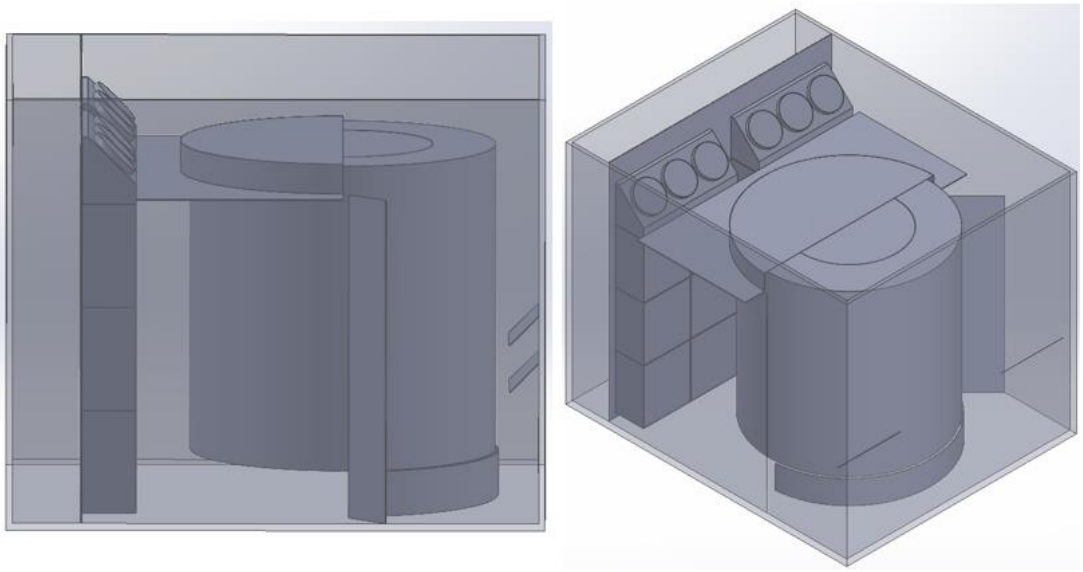

Figure (3.6): Plant 1's simplified spiral freezer for subsequent CFD simulation.

3.1.1 Porous Media Model Parameters

In order to simulate the evaporator coils, spiral belt, and interior porous surfaces such as walkways, these components were treated as porous media in the CFD simulation. The CFD solver treated these regions as volumes of air that experienced an internal resistance to flow. Regions given this treatment have an extra momentum source term given by Equation (3-1), that is added to each of the three conservation of momentum equations [18],

$$S_j = -\left(\frac{\mu}{\alpha}u_j + C_2\frac{1}{2}\rho|u_j|u_j\right) \qquad (3\text{-}1)$$

where $\frac{1}{\alpha}$ and C_2 are user-specified porous media parameters that capture viscous and inertial resistance, respectively, and u_j is the cell velocity for a given cartesianal direction. Equation (3-1) can be more simply viewed as the pressure drop caused by the porous medium's resistance to flow in each respective direction. In the CFD simulation, the resistance to flow depends on both the velocity and the two user-defined porous media resistance terms. Equation (3-2) illustrates how these parameters impact the pressure drop throughout the porous media region [18].

$$\Delta P = \frac{\mu}{\alpha} u + C_2 \frac{1}{2} \rho u^2 \quad (3\text{-}2)$$

To determine the porous media parameters, it is necessary to obtain pressure drop versus velocity data for the given component being modified. This data can then be fitted to a 2nd order polynomial, as demonstrated by Equation (3-3)

$$\Delta P = A_1 u + A_2 u^2 \quad (3\text{-}3)$$

using curve-fit coefficients A_1 and A_2. The viscous and inertial resistance terms can then be calculated using Equations (3-4) and (3-5),

$$\frac{1}{\alpha} = \frac{A_1}{\mu \Delta n} \quad (3\text{-}4)$$

$$C_2 = \frac{2A_2}{\rho \Delta n} \quad (3\text{-}5)$$

where Δn is the length of flow through the component being modeled. The porous media values are anisotropic and were calculated in cartesian or cylindrical coordinates depending on the given component being modeled. For example, in Figure (3.1), the left coil would experience similar resistance (inside the core) with flow perpendicular to the front face as it would with flow perpendicular to the top face. However, flow perpendicular with the side faces is restricted by the fins that span vertically throughout the evaporator coil's core. Therefore, two separate resistances would be used to define this porous region. To reiterate, the resistance terms for this coil in the X and Z directions would be equal while the Y direction is set as a large value resulting in high flow resistance.

3.1.1.1 Determination of Coil Porosity Values

Porosity coefficients for the coils investigated in this project were all determined using the proprietary software developed by the evaporator coil manufacturer. The following parameters were inputs required by the software: number of rows of tubes, tube and fin material, entering air properties,

entering air velocity, tube diameter and pattern, length and height, fin spacing by rows, and fin thickness and surface pattern. The entering velocity was varied from 1.5 to 7 m/s, or as large of a range as the evaporator analysis program would allow, and the manufacturer's predicted pressure drop data was recorded. The data was plotted and curve-fit as shown in Figure (3.7).

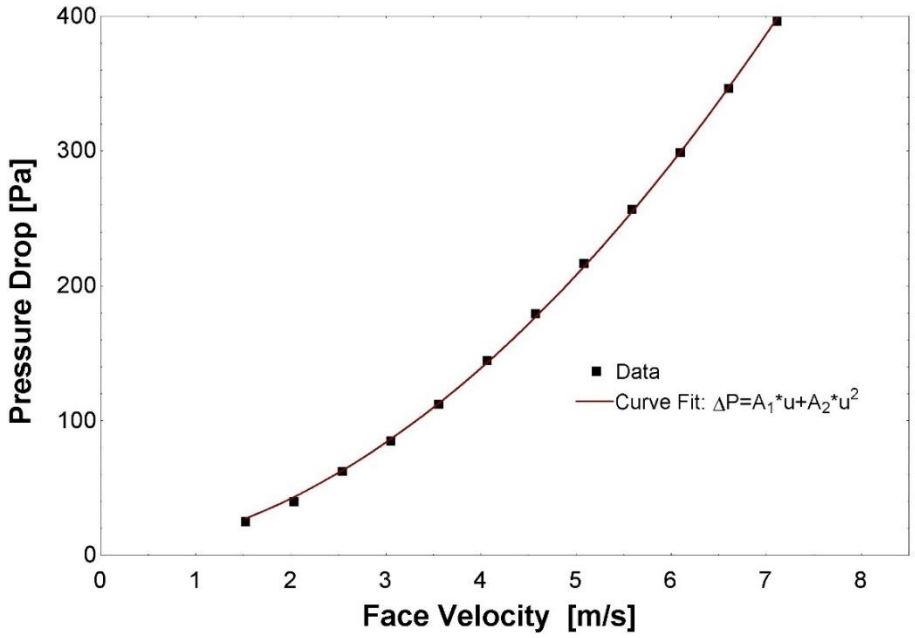

Figure (3.7): Pressure drop versus velocity data for Plant 1's evaporator coils.

Using the curve-fit coefficients, the resistance terms can be solved using Equations (3-4) and (3-5), where ρ and μ are evaluated at the freezer's operating conditions, **Appendix A** Table (A.1). Table (3.1) presents the values of the porous media coefficients of Plant 1's blast freezer. Porosity coefficients for Plant 2 though 4's blast freezers can be located in Table (A.2).

Table (3.1): Porous media resistance coefficients for all plants' evaporator coils.

Plant	Resistance Term	x-dir	y-dir	z-dir
1	Viscous [1/m^2]	411,073	411,073	0
	Inertial [1/m]	8.143	8.143	1,000

For the direction perpendicular to fins, where resistance would be infinite, the inertial resistance was set to an arbitrarily large value, ca. 1,000. The present analysis assumes the porosity remains constant in a

given direction, resulting in a consistent resistance to flow along the path of travel. However, in practice, the fin spacing of blast freezer coils are often varied by tube rows, becoming progressively denser in the direction of air flow through the coil. This variable fin spacing is a strategy evaporator coil manufacturers use to avoid excessive frosting of coil surfaces. As a result, the initial rows are designed with ample space between fins such that significant frost accumulation will not clog airflow. In actuality, this means that the coils would experience varying degrees of resistance along the direction of flow. Nonetheless, the assumption of constant porosity is deemed acceptable as the investigation of flow patterns through the evaporator coils themselves is not a focal point for the present investigation. Rather, the bulk effect of flow passing through the evaporator coils and the resulting total pressure drop is of greater importance. Regardless of whether the flow resistance changes along the path of travel or remains constant, the resulting pressure drop will be the same.

3.1.1.2 Determination of Spiral Porosity Values

To obtain the porosity values of the spiral belt, pressure drop correlations of flow through similarly shaped geometry were utilized. The airflow characteristics of the spirals vary significantly depending on whether the flow is between two levels or is perpendicular to the belt. This distinction is highlighted in Figure (3.8), which illustrates the two different flow paths.

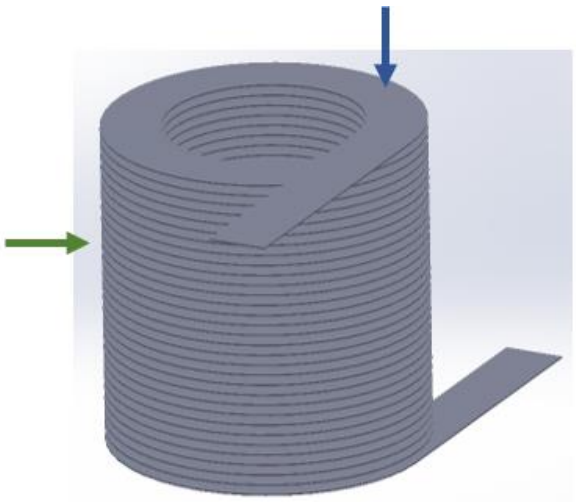

Figure (3.8): The two different flow paths through a spiral: between two levels (green arrow) or perpendicular to the belt (blue arrow).

In the absence of specific correlations or manufacturers' programs, pressure drop correlations of similarly shaped flow channels were used. Specifically, the pressure drop for flow between levels of the spiral, green arrow in Figure (3.8), was calculated using the correlation for square duct flow as described by [19], illustrated in Figure (3.9),

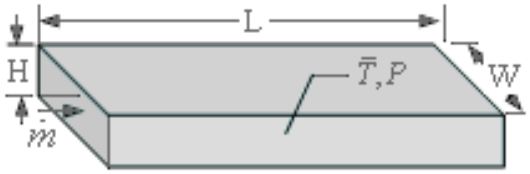

Figure (3.9): Square duct geometry used to model flow between levels of the spiral belt. From EES.

where, H represents the height difference between the average height of the product being conveyed on the spiral belt and the next level of the spiral belt, L indicates the radial width of the spiral belt, while W is an arbitrary value that does affect the result. It is essential to acknowledge the limitations of this geometry approximation as the duct flow correlation assumes solid walls, whereas the spiral belt is not purely duct flow with solid surfaces.

Flow perpendicular to belt was modeled using correlations of contraction and expansion head loss coefficients through circular tube headers as calculated by [20] and [21], shown in Figure (3.10).

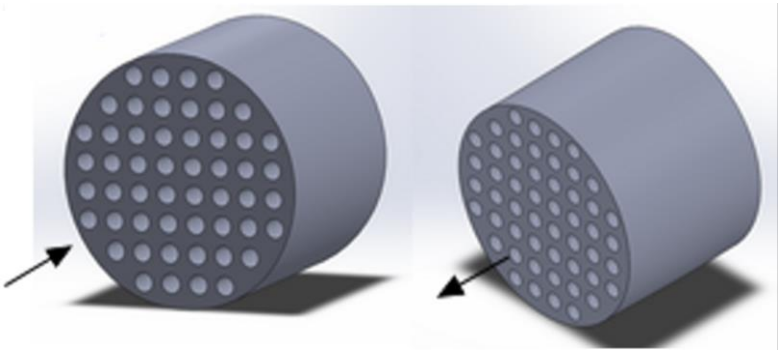

Figure (3.10): Contraction (left) and expansion (right) of circular tube headers used to model flow through the belt. From EES

The correlations use the Reynold's number inside the holes, defined in Equation (3-6), an $\frac{L}{D}$ ratio, and an open area fraction σ_a to calculate the coefficients. Where $\frac{L}{D}$ is the ratio of the length of the hole over its diameter. The open area fraction accounts for product coverage of the belt and openness of the belt itself is calculated using Equation (3-7),

$$Re = \frac{\rho u D}{\mu} \tag{3-6}$$

$$\sigma_a = \frac{A_{open}(1-f_c)}{A_{total}} \tag{3-7}$$

here f_c is the fraction of the belt covered with the product being conveyed, A_{open} is area of the belt that is open to flow, and A_{total} is the total belt area. The former was determined qualitatively, while the latter two were calculated from the dimensions of the belt. Pressure drop was then calculated using Equations (3-8) and (3-9) for both flow contraction and expansion,

$$h_{L,i} = \frac{K_i\, u^2}{2g} \tag{3-8}$$

$$\Delta P_i = \rho g h_{L,i} \tag{3-9}$$

K_i is the respective head loss coefficient and $h_{L,i}$ is the respective head loss. Flow traveling through the belt material will experience the minor effects of both contraction and expansion, therefore the summation is taken. To model the pressure drop through the entire height of the spiral, the effect of one level is multiplied by the total number of levels, N, as seen in Equation (3-10).

$$\Delta P = N \sum(\Delta P_c + \Delta P_e) \tag{3-10}$$

Velocity was varied from 0 to 20 m/s in 0.5 m/s intervals to generate and results that could be curve-fit in the same manner as Figure (3.7). The porosity coefficients are then solved using Equations

(3-4) and (3-5). The belt coverage percent used in the calculation along with the resistance coefficients is given in Table (3.2) for Plant 1's spiral, and Table (A.3) in **Appendix A** for Plants 2 through 4.

Table (3.2): Porous media coefficient for Plant 1's spiral.

Plant	Belt Coverage [%]	Resistance Term	x-dir	y-dir	z-dir
1	50	Viscous [1/m2]	92.64	68801	92.64
		Inertial [1/m]	0.3631	5.618	0.3631

3.1.1.3 Determination of Walkway and Spiral Structure Porosity Values

The walkways and spiral belt's structural supports for the revolving belt itself lack manufacturer-provided data and documented correlations that can be utilized to obtain pressure drop as a function of velocity. Therefore, pressure drop correlations for flow through a similarly shaped geometry is assumed. There are three distinctive styles of semi-open walkways encountered in this research project: circularly perforated, grated, and squarely perforated, as displayed in the following figure.

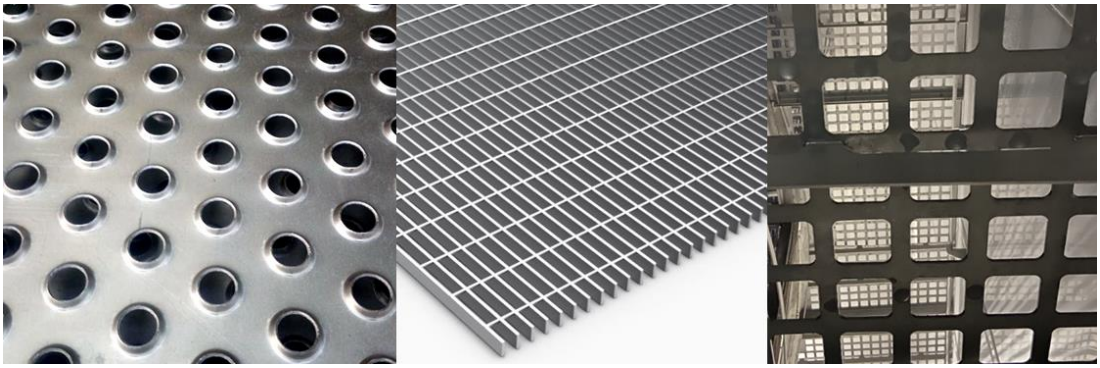

Figure (3.11): Three styles of semi-open walkways: circularly perforated (left), grated (center), and squarely perforated (right) From Dong Jie (left) and Yeti Civil Products (center) .

The circularly-perforated will employ the same circular tube header contraction and expansion coefficient correlation and Equations (3-6) through (3-10), where the fraction covered, f_c, is zero and number of levels, N, is one. For the latter two styles as well the flow through the spiral support

structure, correlations for flow through a sudden contraction and expansion, as shown in Figure (3.12) were used,

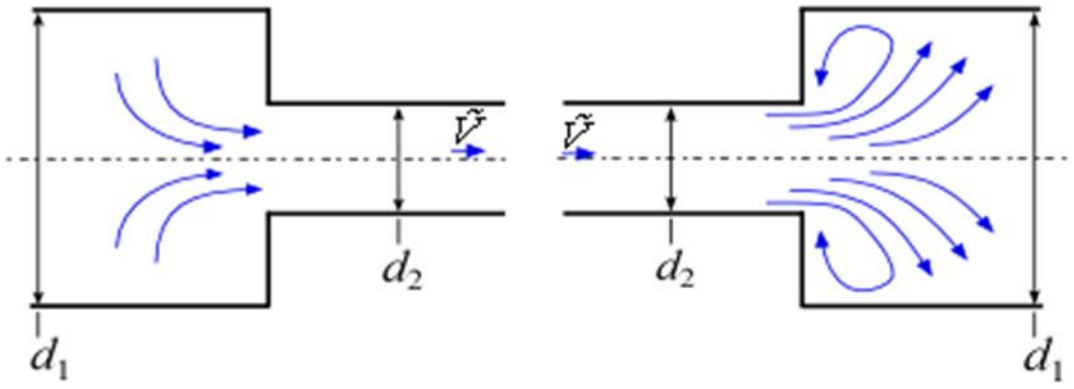

Figure (3.12): Flow through a sudden contraction (left) and expansion (right).

where d_1 and d_2 represent the effective diameter of the area above/below the contraction and inside the contraction, respectively. Effective flow area and diameter, Equations (3-11) and (3-12), are used as the physical rectangular contraction is being modeled via the correlation as a circular contraction.

$$A_i = L_{a,i}\, L_{b,i} \tag{3-11}$$

$$d_i = \sqrt{\frac{4A_i}{\pi}} \tag{3-12}$$

where $L_{a,i}$ and $L_{b,i}$ represent the side lengths of the rectangular area above/below and inside the contraction. Equations (3-8) through (3-10), with N set to 1, were then used to calculate the pressure drop through the walkways and support structure. For the spiral support structure, resistances were established in cylindrical coordinates, wherein the sudden contraction and expansion coefficients were indicative of the radial flow through the vertical support bars. Flow tangential to the bars was treated as a solid wall, thereby leading to arbitrarily large resistance. Conversely, flow in the axial direction, both upward and downward along the vertical bars, was presumed to encounter no flow resistance. Plant 1's porosity coefficients for the open walkways and support structure are presented in Table (3.3), with the corresponding values for Plants 2 through 4 being included in **Appendix A** in Table (A.4).

Table (3.3): Walkway and spiral support structure porosity coefficients for Plant 1.

Component		Walkway			Spiral Support Structure		
Plant	Resistance Term	x-dir	y-dir	z-dir	θ-dir	r-dir	z-dir
1	Viscous [1/m^2]	0	2.056E+06	0	0	115,610	0
	Inertial [1/m]	1000	153.1	1000	1000	11.55	0

Upon examining Table (A.4), it is apparent that there exists a substantial variation in resistance between Plant 1 and Plant 3, as well as between Plant 3 and Plants 2 and 4. Such differences can be attributed to the utilization of different walkway designs across the plants. Specifically, Plant 1's implementation of a circularly perforated walkway with limited airflow capacity stands in stark contrast to Plant 3's employment of a squarely perforated design that facilitates improved airflow. Meanwhile, Plants 2 and 4's usage of grated walkways results in even lower levels of airflow resistance in comparison to their counterparts.

3.1.2 Validation of Porous Media Models

In order to ensure the accuracy of the resistance terms in capturing the relationship between pressure drop and velocity, a CFD validation simulation was developed. This “numerical experiment” involved a comparison of data calculated from a hypothetical evaporator coil [19], a curve-fit model, and the CFD data that resulted from modeling a coil of identical size as a porous media. The calculated data was curve-fit, and the porosity parameters needed as input to the CFD simulation were calculated.

The digital test section utilized in the numerical experiment consisted of two elongated square channels, with a porous media coil positioned in the middle. A "velocity Inlet" boundary condition was applied to the front face of the first channel, while a "Pressure Outlet" was applied to the back face of the second channel, as illustrated in Figure (3.13).

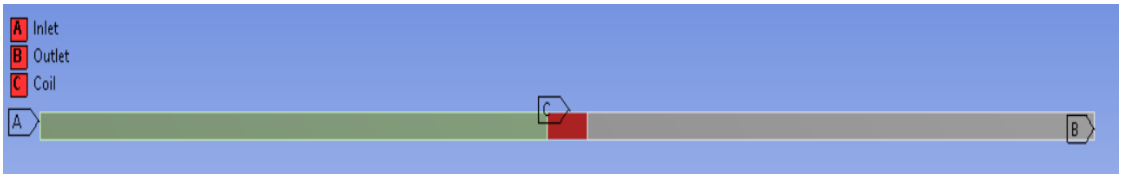

Figure (3.13): Front view of digital test section used to determine pressure drop of porous media coil (red rectangle).

To mitigate the possibility of wall friction interfering with pressure, "symmetry" boundary conditions were employed on the perimeter walls of the two channels in the domain. Conversely, a "wall" condition was implemented on the sides of the porous coil since the calculated values take into account viscous wall effects. The pressure drop between the front and back face of the coil was recorded for four different inlet velocities. Fluid properties remained consistent with those utilized in hypothetical values. The results of this experiment have been tabulated in Table (3.4).

Table (3.4): Results of the CFD porous media validation experiment. Pressure drop data at various velocities.

Inlet Velocity [m/s]	CFD ΔP [Pa]	Calculated ΔP [Pa]	Curve-fit ΔP [Pa]
1	**159.45**	**146.54**	**159.46**
2	**496.88**	**498.83**	**496.80**
3	**1012.10**	**1016.20**	**1012.00**
4	**1705.30**	**1685.20**	**1704.90**

Upon close examination of the table, it is evident that the CFD pressure drop is consistent with both data sets, particularly with the curve fit values. This outcome is to be expected, given that the curve fit determined the appropriate resistance terms to employ in the simulation. Consequently, the accuracy of porous media modeling, when contrasted with actual geometry, is restricted by the goodness of the data fitting. Based on this numerical experiment, it was determined that modeling components as porous media is appropriate when the correlations being used are representative, and data sufficiently fitted.

3.1.3 Fan Curves

To reproduce the flow circulation within a spiral blast freezer, Ansys® Fluent's CFD simulation software utilizes designated surfaces identified as "fans". These surfaces are subjected to fan curve boundary conditions that induced a pressure rise, ΔP, related to the fan surface normal velocity, u. The equations used to describe the fan's performance were derived from the fan manufacturer's data, as shown in Equations (3-13) and (3-14),

$$u = \frac{\dot{V}_{fan}}{A_{fan}} \tag{3-13}$$

$$\Delta P = a_0 + a_1 u + a_2 u^2 + a_3 u^3 + \ldots + a_N u^N \tag{3-14}$$

where $\dot{V}_{fan}$ and A_{fan} represent the volumetric flow rate leaving the "fan" and the area of the "fan" surface in the simulation, respectively. Then, a_0 through a_N represent the derived coefficients of the Nth order curve-fit polynomial. The curve-fit coefficients retained a high number of significant digits as slight rounding would lead to considerable deviations from the data. Piece-wise curve fitting for different ranges throughout the fan's operating spectrum was performed to yield equations most consistent with the fan data. The fan curve used in Plant 1's CFD simulation and the general equation used to define the fan boundary conditions are illustrated in Figure (3.14).

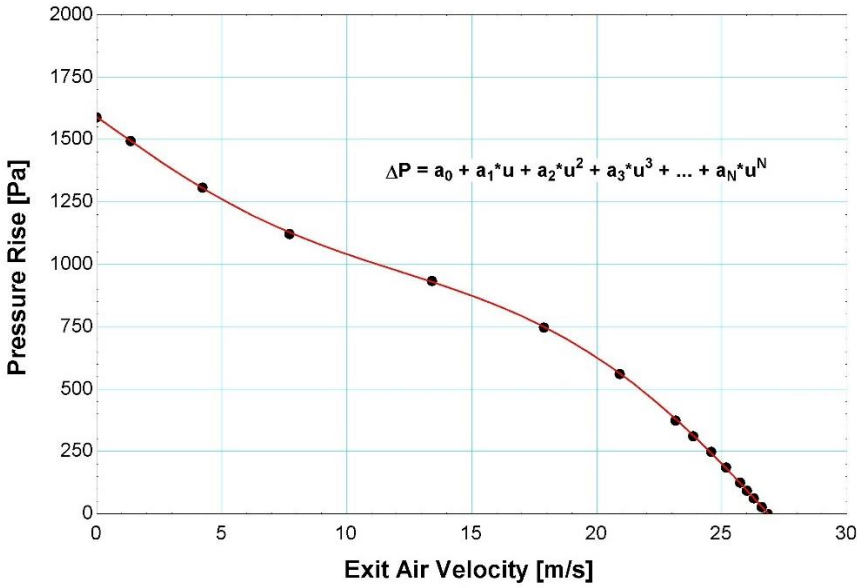

Figure (3.14): Sample fan curve-fit and the points calculated from the manufacturer's given data. Data from Airfoil Impellers.

Utilizing a fan curve instead of a fixed pressure rise or velocity provides significant advantages as it allows for the CFD solver to accurately match the pressure drop of the simplified fan model to the actual performance consistent with the fan in real-world scenarios. This is particularly crucial for subsequent iterations involving modified geometries within the blast freezer interior and the resulting effects added features would have on the pressure drop external to the fan, ensuring the model remains consistent and valid in a dynamic environment. The coefficients for Plant 1's fan curve are given in the subsequent table, additional information for Plants 2 through 4 can be found in Table (A.5).

Table (3.5): Fan curve-fit coefficients with correspond lower and upper velocity bounds for Plant 1.

Plant	a_0	a_1	a_2	a_3	a_4	a_5
1	1589.89634	-71.6094163	-0.16975422	0.36175799	-0.0209997577	0.000313021173
	Lower Limit [m/s]			**Upper Limit [m/s]**		
	0			**26.8608913**		

The fan curves were given lower and upper velocity limits within the solver such that non-physical phenomena, negative pressure rise through the fan, would not occur.

3.2 Meshing and Solving Process

3.2.1 Mesh

The meshing process plays a crucial role in CFD simulations. It determines the accuracy of the solution and the computational effort required to advance iterations of the simulation. Smaller elements generally lead to reduced computational errors; however, smaller mesh sizes comes at the expense of increased computational costs. To strike a balance between accuracy and efficiency, it is essential to carefully control the mesh density in areas of interest and regions with strong flow gradients. Additionally, to generate a suitable mesh for a CFD simulation, it is essential to have some understanding of the CFD solver that will be employed. This is because each solver has its unique mesh requirements, which must be adequately met for accurate simulation results. The following section provides a detailed account of the coupled meshing and solving process along with the rationale for the selection of each method.

In the case of a blast freezer, the flow inside is expected to exhibit high levels of turbulence due to the use of high air velocity blowing over blunt features to achieve the desired product cooling effect. As a result, the selection of an appropriate turbulence model is crucial for accurately predicting the fluid flow behavior. In this study, the realizable $k-\in$ turbulence model with enhanced wall treatment was deemed suitable due to its capability in accurately predicting turbulent flow away from the wall, its capacity to manage adverse pressure gradients, flow separation, and recirculation phenomena [22], which are typically encountered in blast freezers.

Compared to the widely used $k-\omega$ SST turbulence model, the $k-\in$ model was preferred due to its near-wall treatment approach. The $k-\omega$ SST model resolves the boundary layer down to the viscous sub-layer, necessitating a fine discretization with y^+ values less than 1. Where y^+ represents the

dimensionless position away from the wall of the first node. Conversely, the $k-\in$ model employs wall functions to account for the boundary layer effects. Considering the fact that blast freezers consist of large walls and baffles, the $k-\in$ model proved to be less computationally demanding. For the near-wall treatment, the enhanced wall function were utilized with the CFD solver. The enhanced wall function has been shown to model the boundary layer in regions outside the buffer zone, y^+ less than 5 and or between 30 and 200, more accurately than the standard [23]. Hence, the selected turbulence model was deemed appropriate for the blast freezer application under consideration. Mesh refinement in the form of "inflation layers," were utilized to capture dynamic viscous phenomena that occur in proximity to solid boundaries. An illustration of inflation layers is given in Figure (3.15).

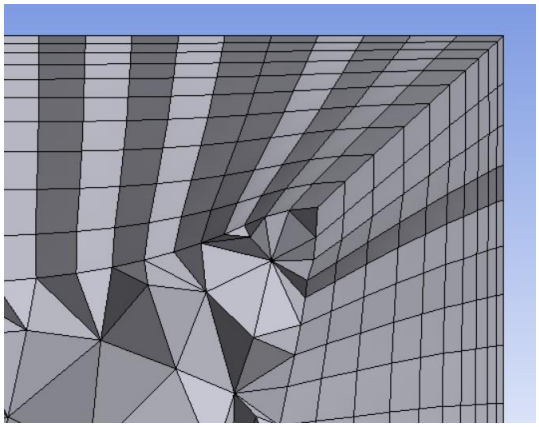

Figure (3.15): Mesh inflation layers applied to all key wall boundary conditions within the model.

Inflation layers were applied to all walls within the CFD model. This mesh refinement technique was implemented through the Ansys® meshing software, which allowed for the specification of a first layer cell height, x_1, cell growth rate, γ, and number of inflation layers, N_{layers}, in route of discretizing the domain. Each surface included ten inflation layers; the growth rate was calculated such that the last inflation layer was the same size as the mesh, Δx_v, the elements were inflating into, Equation (3-15).

$$\gamma = \left[\frac{\Delta x_v}{x_1}\right]^{\left(\frac{1}{N_{layers}+1}\right)} \qquad (3\text{-}15)$$

The height of the first layer, x_1, is selected such that it is consistent with the y^+ requirements of the $k-\in$ enhanced wall treatment model, within 30 and 200 and or less than 5. However, determining the y^+at a specific location requires knowledge of the velocity. Because velocity is not known a priori, an initial mesh and model was constructed and simulated, prior to the final iteration, to predict velocities near wall boundaries. The initial mesh was given a first layer inflation height of 7.5 mm, which was found to satisfy y^+ requirements with little manipulation from initial to final mesh iterations. Additional forms of mesh refinement were then applied to the model. Each surface of the volume was meshed at a one-half reduction of global element size as the mesh near walls, which experience greater velocity and pressure gradients, should be finer. A global, or default, mesh size of 125 mm was applied, i.e., any surface or volume not explicitly sized would default to that value. The global mesh size was determined from the mesh sensitivity analysis shown in **Section 4.1**. In addition, fan and coil volumes were meshed with a one-half reduction, while the "fan" surfaces were meshed to a one-quarter reduction.

The volume of air upstream and downstream of the fans will experience the largest pressure and velocity gradients. As such, spherical regions located at the center of the fans were meshed at a one-half reduction, as well. Additionally, annular shaped components, such as the spiral and its support structure, were meshed using the sweeping method, a technique characterized by the number of radial and axial elements, N_r, and N_y, respectively, and bounded angularly by the element size of a one-half global reduction. The fine mesh elements of the spiral and support structure are illustrated below.

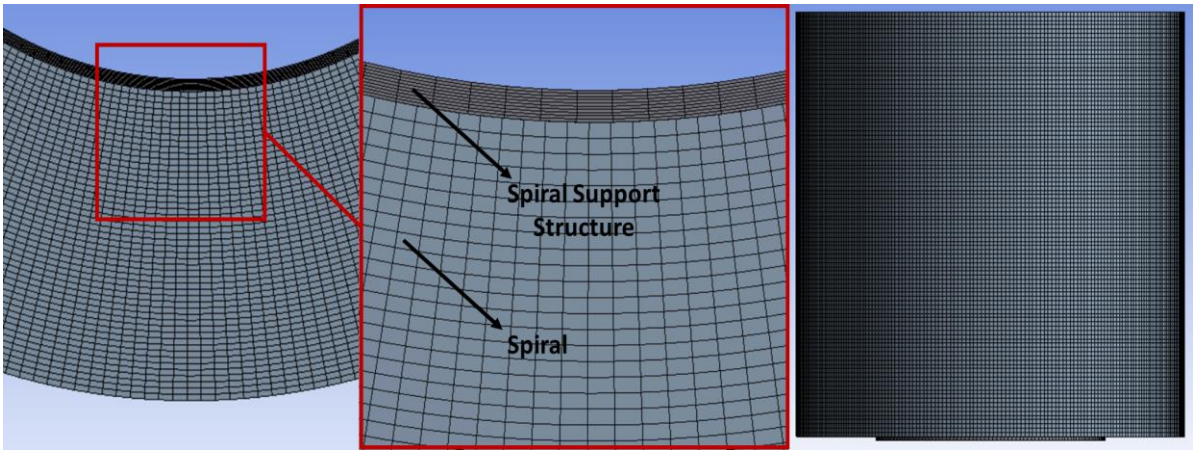

Figure (3.16): Top view of radial elements (left), close-up (center), view of axial elements (right).

The radial element size of the support structure is further reduced, ensuring the pressure distribution through the thin feature is represented with sufficient elements, N_r. Applying the mesh refinements mentioned, Figure (3.17) highlights the cross-section of Plant 1's spiral freezer.

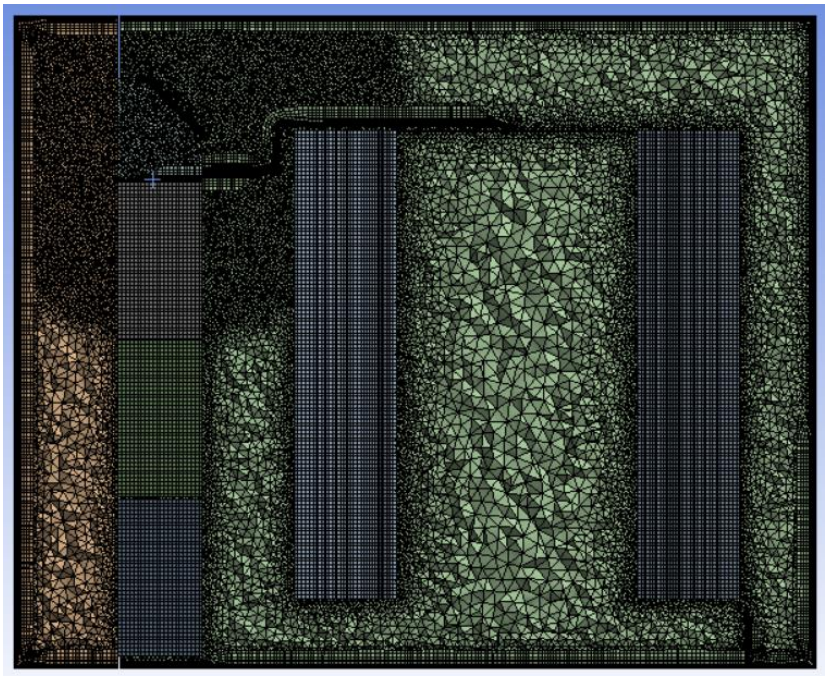

Figure (3.17): Mesh cross-section of spiral blast freezer for Plant 1.

From the figure, one can see the relative coarseness in the mesh in regions far from surfaces or regions of interest. This was applied intentionally to provide a reduction in overall element count. Inflated surfaces, component volumes, and surfaces of interest were given named selections, for subsequent

data exportation. Using the method that will be described in **Section 3.2.2**, the initial mesh is solved. Using Ansys®'s post-processing software, average y^+values were recorded at each surface, as illustrated in the figure, below.

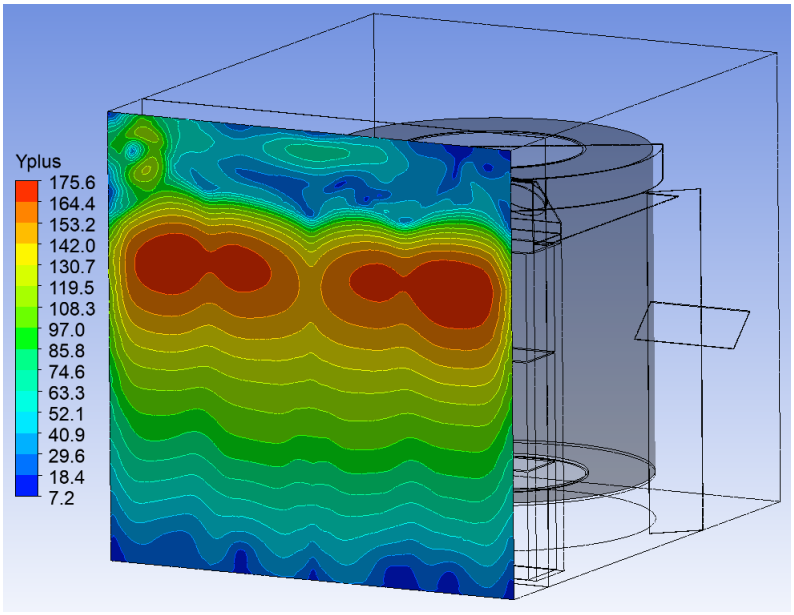

Figure (3.18): y^+contours generated at each surface to determine necessary adjustment of first layer mesh size.

The height of the first inflation layers were then adjusted such that the expected y^+ values would be within the 30 to 200 requirement, as shown by Equation (3-16).

$$x_1 = x_{1,initial} \frac{{y^+}_{req}}{{y^+}_{initial}} \qquad (3\text{-}16)$$

Final versions of each mesh were then constructed with the updated first inflation layers and sent to Ansys® Fluent's CFD software to be solved and analyzed.

3.2.2 Solver Methods

The CFD simulations were solved using the realizable $k-\epsilon$ turbulence model, which employs enhanced wall functions, in conjunction with the three Navier-Stokes conservation of momentum

equations and the conservation of mass equation. The $k-\epsilon$ turbulence model is a Reynolds Averaged Navier-Stokes (RANS) model, which utilizes two closure terms, namely the turbulent kinetic energy (k) and the rate of dissipation of turbulent kinetic energy (ϵ). RANS models separate flow variables into mean and fluctuating components. Taking the temporal average of turbulent fluctuations, RANS models can predict the mean flow field. Unlike the Large Eddy Simulation (LES) or the Direct Numerical Simulation (DNS) methods, RANS models do not resolve large or small turbulent eddies. However, LES and DNS simulations requires an orders of magnitude reduction in element size, such that computational cost will exceed available resources.

For industrial-scale flows, such as those present in a spiral blast freezer, RANS predictions of temporally averaged field variables are sufficient, as they provide a good representation of the flow behavior [24].

3.2.2.1 Employing the Simulation

The selection of a CFD solver for the present project was made with consideration for the physical nature of the flow being simulated as well as the computational resources and user control requirements. The commercial software Ansys® Fluent was utilized due to its wide range of capabilities and user control options. The pressure-based steady-state Navier-Stokes equations were employed without the conservation of energy equation, utilizing a coupled pressure-velocity scheme with 2nd order pressure and 2nd order upwind momentum discretization, and a 1st order upwind turbulent kinetic energy and dissipation rate discretization.

The selection of the pressure-based solver was based on the fact that it is better suited for incompressible flows or flows with weakly changing density [25]. The model used a pressure-velocity coupling scheme as opposed to a segregated scheme. Coupled schemes solve the pressure and velocity field simultaneously as opposed to the segregated schemes which employ an iterative predictor

corrector approach. The former results in a slight increase in computational expense per iteration but reduces convergence time significantly [25]. A steady-state solver was chosen due to the longer time-scale of the freezing process of products within the blast freezer in comparison to any transient effects from internal transients such as belt stoppages or coil defrost cycles. While the energy equation was not explicitly modeled, the omission was deemed acceptable as volumetric generation terms could not be accurately applied to the coil and spiral porous mediums. The default selection of 2^{nd} order pressure and 2^{nd} order upwind momentum discretization, and 1^{st} order upwind turbulent kinetic energy and dissipation rate discretization were deemed sufficient and left unchanged, as the increase in computational expense associated with higher order differencing was deemed to be outweighed by the increase in accuracy with regards to the momentum and pressure gradient, while 1^{st} order differencing was deemed sufficient for the turbulent kinetic energy and dissipation rate [26].

3.2.2.2 Input and Output Information

The information calculated in **Section 3.1** was integrated into the Ansys® Fluent CFD software and plays a crucial role in accurately modeling the flow field within a spiral blast freezer. The entire volume of the blast freezer, along with its individual components, were assigned densities and viscosities that corresponded to the operating temperature and pressure conditions of the respective freezing system, found in Table (A.1) in **Appendix A**. Additionally, the cell zone conditions, as referred to by Ansys® Fluent, represent the physical properties present in their respective regions. As such, porosity values determined from the computations in **Sections 3.1.1.1**, **3.1.1.2**, and **3.1.1.3**, were subsequently implemented into the cell zone conditions of each component, respectively, Table (A.3) and Table (A.4). Walls within the model were given no-slip boundary conditions, while the interfaces between non-solid components, such as the outer surface of the spiral and volume or the front face of the coils and volume, were left at their default settings, resulting in no wall effects. Furthermore, the curve-fit

equations derived in **Section 3.1.3** were applied to the previously identified "fan" surfaces, thus ensuring the dynamic effect of the fan were being captured, Table (A.5).

The simulation process was iterated until the results were considered to have reached a state of convergence, which was determined based on the point when the residuals of the six governing equations and the average coil volume velocity reached a plateau. Residual reduction of two orders of magnitude or greater were deemed sufficiently small. Throughout the simulation, several other parameters were closely monitored, including the average coil face velocity, average spiral volume velocity, and the total flow rate out of the fans. The final values obtained for these monitored data quantities were duly recorded and were subsequently used as the foundational criteria for evaluating the overall performance of the spiral blast freezer, as demonstrated in **Section 5.1**.

3.2.2.3 Post-Processing

Post-processing results of the CFD simulations represents a crucial stage in evaluating the performance of individual models. This is facilitated by the generation of several visual aids and datasets, enabled by Ansys®'s advanced post-processing software. With the visual aids, problem areas can be qualitatively identified, and subsequent baffling modifications can be proposed.

Velocity streamlines, which start from the fan outlets, were utilized to analyze bulk airflow patterns within the freezer. Figure (3.19) captures the intricate airflow distribution within the spiral freezer of Plant 1.

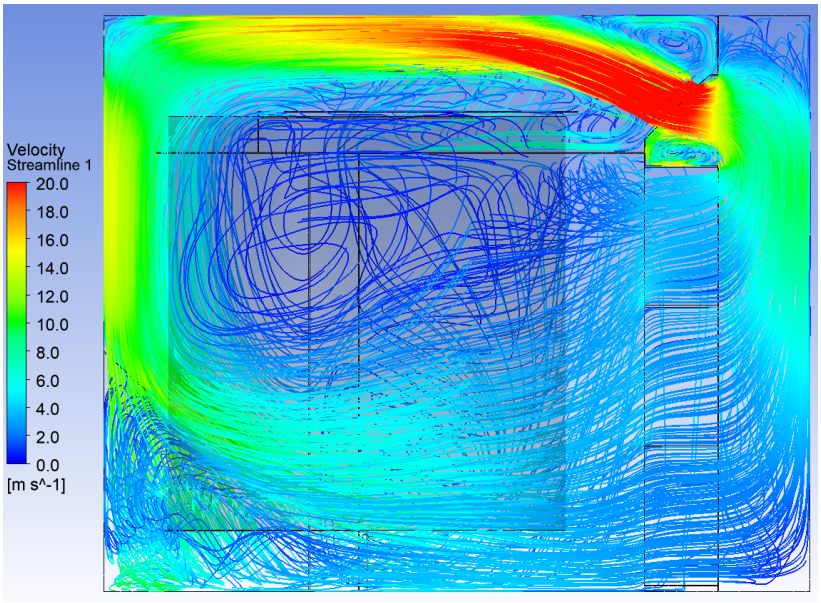

Figure (3.19): Velocity streamlines detailing airflow distribution inside Plant 1's freezer.

With the velocity streamlines, issues with the airflow patterns throughout the freezers become visually apparent. For example, there is a large recirculation zone near the top of the spiral. Additionally, there is a significant quantity of air flowing below the spiral belt bypassing the product. These and other opportunities for air-side performance improvement will be covered in more detail in **Chapter 5**.

To further facilitate the investigation, a spiral "point cloud," shown in Figure (3.20), was generated for each blast freezing system analyzed. The point cloud represents the trajectory of the product during its stay in the blast freezer.

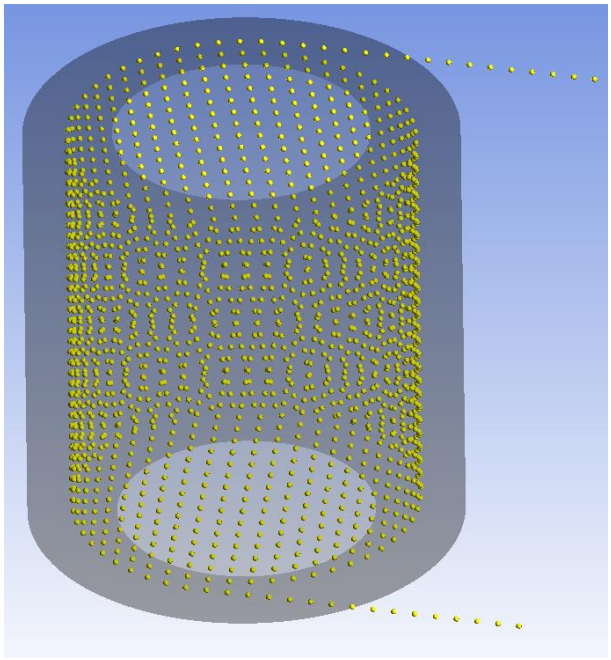

Figure (3.20): Spiral point cloud used in post-processing.

Notably, the point cloud is composed of points situated equidistantly from the inner and outer radii, i.e., those that correspond to the middle lane of products. Straight lines jetting off tangentially represent the linear sections of belt near the infeed and outfeeds. The number of points is determined by the length of the experimentally collected data, which will be discussed further in **Section 4.2.1**, approximately representing the dwell time of the product inside the freezer. By extracting velocity vectors and magnitudes from the point cloud, the velocity magnitude as a function of time in the freezer can be plotted, as demonstrated in Figure (3.21).

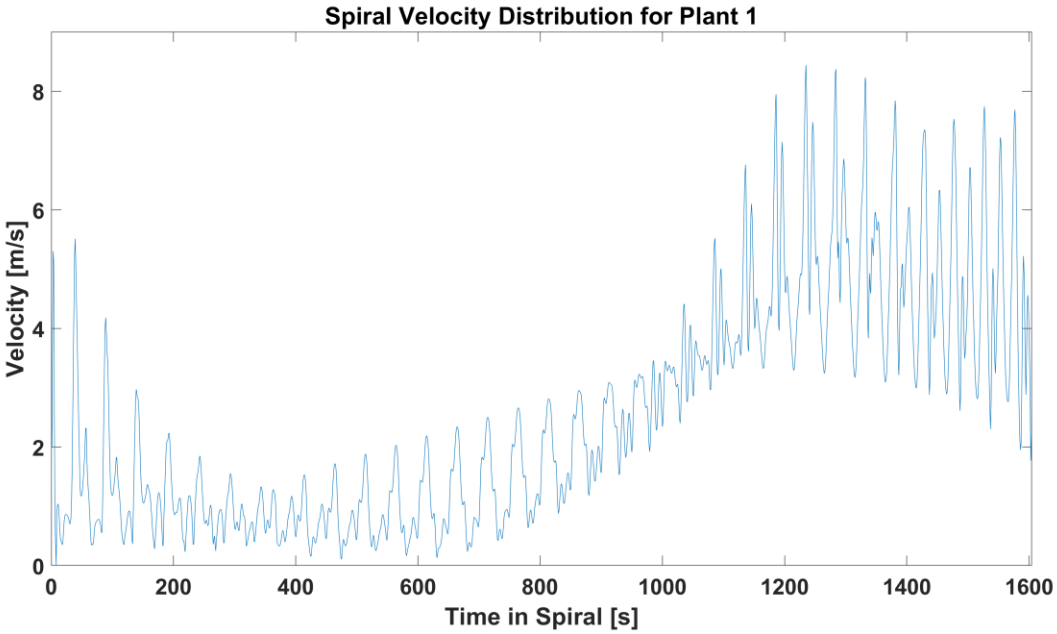

Figure (3.21): Spiral velocity distribution throughout products' dwell time.

Utilizing the data obtained from the spiral velocity plots, it is possible to quantitatively assess the performance of the freezer. To aid in the visualization of the velocity distribution within the spiral, 3D quiver plots originating at the point cloud were also created, as shown in Figure (3.22).

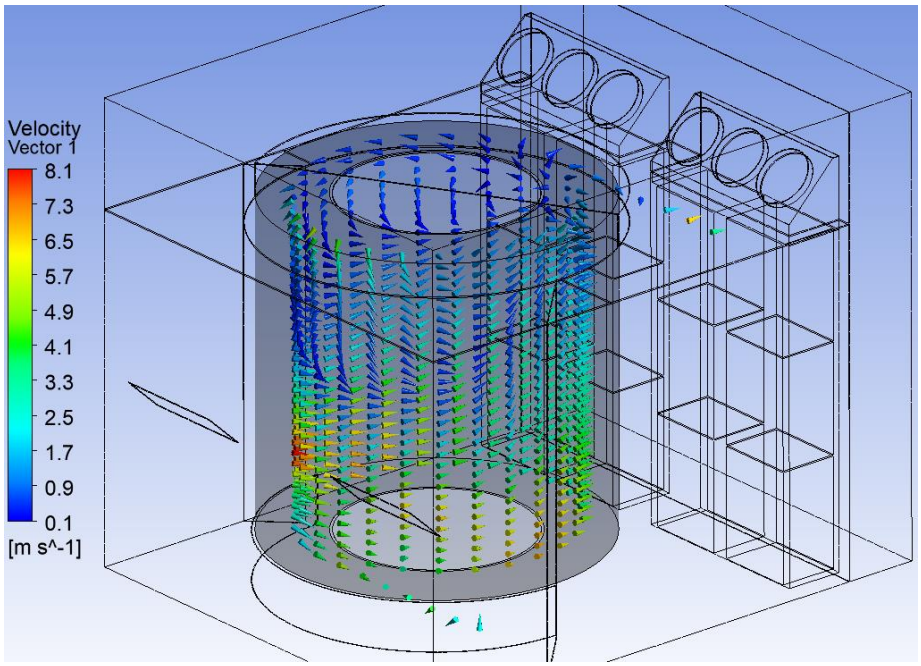

Figure (3.22): 3D quiver plots used to analyze airflow patterns within spirals.

While these quiver plots are not shown for each model, they were a useful visual aid in discerning key features of the spiral velocity distributions and streamline figures.

Overall, the above-mentioned methodologies enable a comprehensive evaluation of the airflow performance of the spiral freezer. The data obtained from this analysis was used in the validation studies discussed in the following chapter.

Chapter 4 MODEL VALIDATION

Validation of any numerical model is an integral step to establish confidence in its predictability and dependability. This is particularly critical in the case of using CFD for numerical modeling of blast freezers, where simplifications and assumptions were required to represent the complex domain in a computationally reasonable way. The validation of the CFD model and methods utilized was accomplished in a two-step process. First, a mesh sensitivity analysis was conducted to ensure the mesh density was sufficient to accurately represent the flow behavior within the computational domain. Second, in operando, experimental data on multiple industrial-scale blast freezing systems were obtained and compared with the simulation results to verify the fidelity of the model.

4.1 Mesh Sensitivity Analysis

Mesh sensitivity analyses were performed on the CFD models for the blast freezers found in both Plants 1 and 2, with the objective of ensuring consistency in the simulations. The sensitivity analyses also served the additional purpose of identifying the appropriate mesh size, which is essential for accurately capturing the effects of the intricate features and the observed air velocities in each respective system. While it would be ideal to conduct a mesh sensitivity analysis for all future plants and design iterations, the number of distinct models and, consequently, the number of simulations associated with this particular project renders this an impossibly time-intensive process.

Each sensitivity analysis consisted of four separate simulations with increasingly finer mesh resolutions. The grid refinement factor, r_f, of 1.25, as prescribed by [27], was implemented for the analysis, Equation (4-1)

$$N_2 = {r_f}^3 \, N_1 \qquad (4\text{-}1)$$

where N_1 and N_2 are the number of elements for current and succeeding meshes. This resulted in subsequent mesh having roughly twice the number of elements as its predecessor. Volume-average measurements of predicted spiral air velocity and coil air velocity, as well as total fan flow rate data obtained from the simulation, served as a benchmark for comparing the four meshes. Each mesh was given a global, or default, mesh size, i.e., any surface or volume not explicitly sized would default to that value. The one-half and one-quarter global mesh refinements for specific surfaces and volumes were applied in the same manner as described in **Section 3.2.1**. The number of radial and axial elements, N_r, and N_y, respectively, where increased by the grid refinement factor for each successively finer mesh. Upon achieving a state of sufficient convergence in the simulation, as described in **Section 3.2.2.1**, the values of the three comparative criteria were recorded at each iteration. 100 iterations were then ran, thereby enabling the determination of both the average value and range of values for each criterion across the converged iterations. A summary of the results obtained from the four different mesh sizes employed in Plant 1's sensitivity analysis, is presented in Table (4.1). The results of Plant 2's mesh sensitivity analysis can be found in **Appendix B** in Table (B.2).

Table (4.1): Mesh Sensitivity Analysis for Plant 1. Criteria cells represent the average and range of recorded values.

Mesh	Global Mesh Size [mm]	Element Count	Avg. Spiral Velocity [m/s]	Avg. Coil Velocity [m/s]	Total Fan Flow Rate [m^3/s]
Coarse	**156.25**	**7,575,811**	**2.663 ± 0.267**	**2.852 ± 0.058**	**104.7 ± 2.81**
Medium	**125**	**12,933,027**	**2.646 ± 0.025**	**2.879 ± 0.022**	**105.6 ± 0.05**
Fine	**100**	**22,381,892**	**2.617 ± 0.062**	**2.879 ±0.026**	**105.5 ± 0.05**
Very Fine	**80**	**39,575,137**	**2.595 ± 0.094**	**2.881 ± 0.021**	**105.8 ± 0.04**

Although the values of the three metrics under consideration are relatively consistent throughout, the degree of variability in the results reveals the crucial differences between the simulations. Specifically, the coarse mesh exhibited significant fluctuations in the average spiral velocity during the simulation due to a lack of convergence, as depicted in Figure (4.1). This indicates that the coarse mesh was not

sufficiently refined to provide stable and accurate results and underscores the importance of employing an appropriate mesh resolution in CFD simulations.

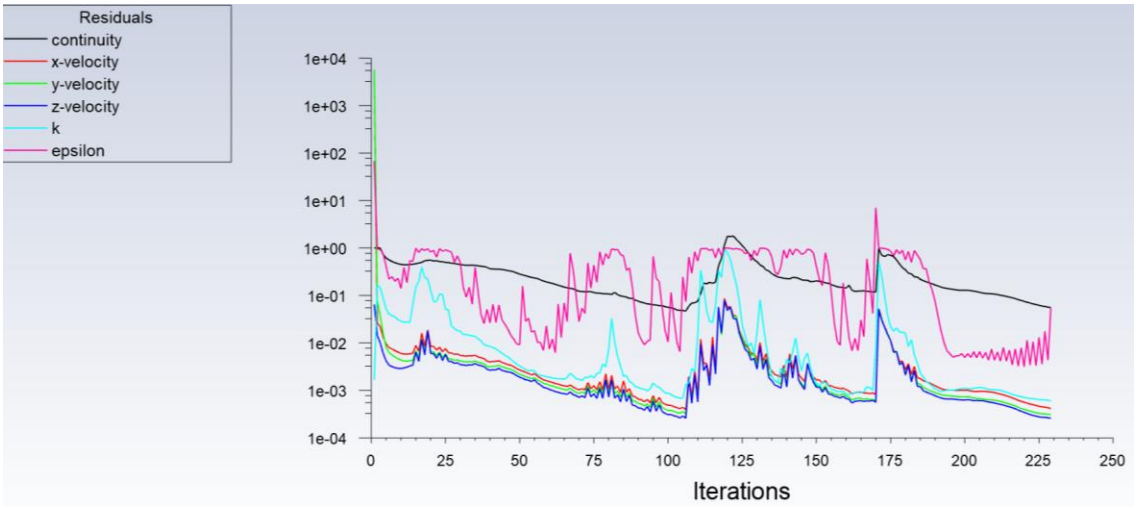

Figure (4.1): Residuals vs. iteration for the coarse mesh.

The convergence behavior of the residuals, which indicate the error between the left and right-hand sides of the respective governing equations, provide insight into the adequacy of the mesh resolution. In the coarse mesh case, the residuals begin to converge before abruptly spiking, following this pattern several times. This likely indicates that the mesh is too coarse to resolve the relevant flow phenomena and or the element quality associated with the coarse mesh is poor, causing numerical instability and the variance in spiral velocity observed in Table (4.1). Surprisingly, as the mesh resolution is further refined, the variability in spiral velocity increases. This phenomenon can likely be attributed to an overly fine mesh resolution, in which the model is fine enough in certain areas to resolve the turbulent eddies that the RANS model is attempting to model [28]. This, in turn, results in the average velocity fluctuating in the spiral region. This observation is not evident in the average coil velocities because the turbulent equations are not modeled in this region, and thus no temporal averaging is competing against resolved turbulent eddies. This effect stresses the need for an optimal mesh resolution in CFD simulations, which should be carefully chosen to balance the competing requirements of resolving the flow field and temporally averaging the turbulent fluctuations. The results of the grid sensitivity analyses revealed that

the medium density mesh provided the best combination of precision, stability, and computational efficiency. Therefore, it was concluded that a global element size of 125 mm would be satisfactory for subsequent plant models and their design iterations.

4.2 Experimental Validation

4.2.1 The Phantom

In order to maintain a high level of consistency between the computational models and the underlying physical systems, an instrument referred to as the "Phantom" was designed and fabricated to collect heat transfer data within the spiral freezer [29]. The experimental results from running the Phantom through a plant's blast freezer were then compared against predictions obtained from the respective CFD simulation. The Phantom is depicted in Figure (4.2).

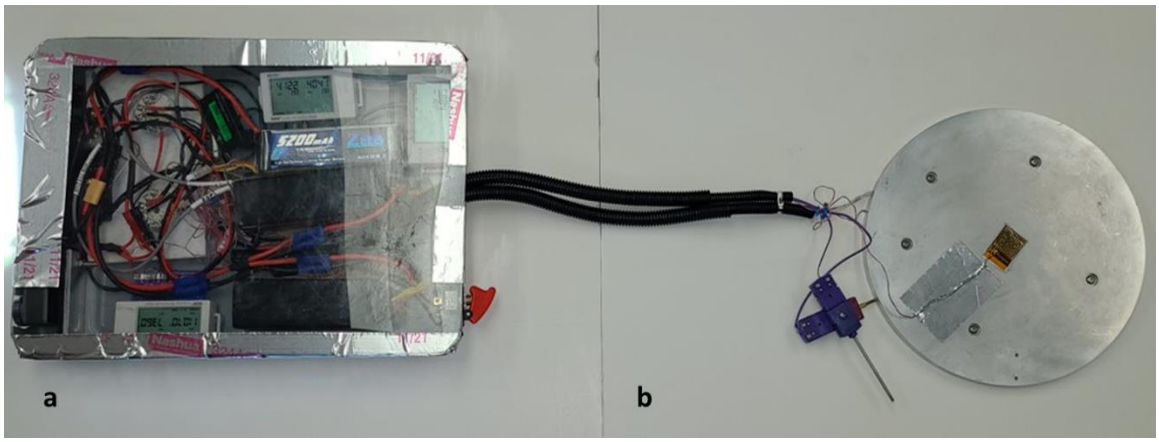

Figure (4.2): Phantom device (b) and data collection tote (a) used to experimentally validate CFD results.

The Phantom is comprised of two distinct units - a power and data collection tote, shown in Figure (4.2a), and a measurement device, shown in Figure (4.2b). The measurement device consists of two mirror image 11.5 in diameter disks made of 5/16 in thick 6061 aluminum fastened together with stainless steel hardware. The disks have an internally recessed cavity that houses a 180 W square pad heater, which ensures an elevated temperature for the entire duration of the experiment. Heat flux

sensors with built-in thermocouples are situated on the outer surface of the disks to measure surface temperatures, while additional thermocouples are positioned inside and outside the disks to record internal and ambient temperatures, respectively. The power tote houses two 22.2 V lithium-ion batteries, connected in parallel, that provide the necessary power to the heater. Additionally, the tote contains three data collection devices that record temperature, heat flux, and power supplied to the heater. The data gathered from temperature and heat flux measurements are used to calculate an effective heat transfer coefficient, h, through Equation (4-2),

$$h = \dot{Q}" \, (T_s - T_\infty) \qquad (4\text{-}2)$$

where $\dot{Q}"$ is the measured heat flux and T_s and T_∞ are the surface and ambient temperatures, respectively. For more information on the Phantom instrumentation and the associated errors in the measurements see [29].

For a given experimental run, the Phantom was situated upon the plant's operating spiral conveyor belt at the center of the system's infeed, tracking the trajectory of the product throughout the spiral prior to its eventual capture at the outfeed. The Phantom traverses through the blast freezer on the spiral belt simultaneously with food product being frozen. Data are collected at a rate of 1 Hz; thereby, enabling the mapping of heat flux values within the spiral structure, both spatially and pseudo-temporally (referring to the fact that each spatial point inside the structure is represented by a single instant in time during the travel). The total number of data points collected during the experiment determines the number of data points present in the CFD spiral point cloud, as mentioned in **Section 3.2.2.3**. It is important to note that the starting point for the "point cloud" is synchronized to correspond to the Phantom's physical location at the onset of data collection. This synchronization process ensures the "point cloud" information provided by the CFD model accurately reflects the spatial location of the Phantom within the freezing system for model comparison.

4.2.2 Phantom − CFD Comparison

Because the governing energy balance equation, conservation of energy, was not solved as part of the CFD simulation, as outlined in **Section 3.2.2**, only velocity information could be exported from the CFD model for comparison with the Phantom. Because the Phantom provided operational heat flux data, a method of bridging the gap between the velocity data obtained from the CFD simulation and the heat flux data measured by the Phantom was developed.

The Phantom is subject to three modes of heat transfer with the surroundings of the freezer, namely, forced convection with the recirculating airflow, natural convection when observed flow is low, and radiation with cold surfaces. The design of the Phantom, which is in the form of a flat disk, makes it possible to apply correlations associated with flow over a flat plate independent of direction. As such, the correlation for flow over a flat plate with turbulence, developed by [31], was utilized to predict the forced convection contribution to the measured heat transfer coefficient. This correlation is illustrated in Equations (4-3) through (4-15),

$$Re_l = 3.6E5\ {I_t}^{-5/4} \tag{4-3}$$

$$c = 0.9922\ log_{10}(Re_l) - 3.013 \tag{4-4}$$

$$T_{film,i} = \frac{T_{s,i} + T_{\infty,i}}{2} \tag{4-5}$$

$$\bar{u}_i = \sqrt{{u_i}^2 + {v_i}^2 + {w_i}^2} \tag{4-6}$$

$$Re_i = \frac{\rho_i\, \bar{u}_i\, L_{char}}{\mu_i} \tag{4-7}$$

$$Pr_i = \frac{Cp_i\, \mu_i}{k_i} \tag{4-8}$$

$$Nu_{lam,i} = \frac{0.3387 {Re_i}^{1/2} {Pr_i}^{1/3}}{\left(1+(0.0468/Pr_i)^{2/3}\right)^{1/4}} \quad (4\text{-}9)$$

$$Nu_{lam_l,i} = \frac{0.3387 {Re_l}^{1/2} {Pr_i}^{1/3}}{\left(1+(0.0468/Pr_i)^{2/3}\right)^{1/4}} \quad (4\text{-}10)$$

$$Nu_{trans,i} = Nu_{lam_l,i} \left(\frac{Re_i}{Re_l}\right)^c \quad (4\text{-}11)$$

$$Cf_{turb,i} = \frac{0.455}{(log_{10}(0.06\, Re_i))^2} \quad (4\text{-}12)$$

$$Nu_{turb,i} = \frac{Re_i\, Pr_i \left(\frac{Cf_{turb,i}}{2}\right)}{1+12.7({Pr_i}^{2/3}-1)\sqrt{\frac{Cf_{turb,i}}{2}}} \quad (4\text{-}13)$$

$$Nu_{FC,i} = \left({Nu_{lam,i}}^5 + \left({Nu_{trans,i}}^{-10} + {Nu_{turb,i}}^{-10}\right)^{-1/2}\right)^{1/5} \quad (4\text{-}14)$$

$$h_{FC,i} = \frac{Nu_{FC,i}\, k_i}{L_{char}} \quad (4\text{-}15)$$

where "i" represents the i^{th} data point and thermal physical properties were calculated at the film temperature, $T_{film,i}$. A function was developed in MATLAB® to calculate the forced convective heat transfer coefficients from inputs of velocity magnitude, temperature, characteristic length, and turbulent intensity. The uvw velocity magnitude, $\bar{u}$, obtained from the CFD results, was used of a strictly parallel flow, uw velocity magnitude, as the small vertical component, v, was expected to contribute to heat transfer and was thus taken into account. Surface and ambient temperatures were obtained from the Phantom instrumentation, as temperature data cannot be directly obtained from the simulations. The characteristic length, L_{char}, used in the correlation was based on the radius of the Phantom. The turbulent intensity, I_t, which reflects the percentage of velocity fluctuation over the mean velocity and indicates how turbulent the flow is, was assumed to be 17%, a typical value observed in the simulations. The natural convection component of the overall heat transfer coefficient was calculated with a natural

convection correlation for a flat plate [12], using Equations (2-17) through (2-21) from **Section 2.1.4**, as well as Equation (4-16),

$$h_{NC,i} = \frac{Nu_{NC,i}\, k_i\, P}{A} \qquad (4\text{-}16)$$

where P and A represent the perimeter and top surface area of the Phantom and $\mathrm{Nu}_{NC,i}$ is $Nu_{horizontal}$ at the *i* th point. With the forced and natural convection coefficients a total convective heat transfer coefficient could be computed at each point via Equation (4-17) [16].

$$h_{C,i} = \left(max\left(h_{FC,i}\,, h_{NC,i}\right)^3 + min\left(h_{FC,i}\,, h_{NC,i}\right)^3\right)^{1/3} \qquad (4\text{-}17)$$

Lastly, the radiation heat transfer coefficient was determined using a manipulation of the Stefan-Boltzmann law, Equation (4-18),

$$h_{r,i} = \varepsilon\, \sigma \left({T_{s,i}}^2 + {T_{\infty,i}}^2\right)\left(T_{s,i} + T_{\infty,i}\right) \qquad (4\text{-}18)$$

where the emissivity, ε, was that of the heat flux sensor itself, which was determined to be 0.83 via an infrared temperature gun. The convective and radiative terms were then summed together to produce the overall heat transfer coefficient, Equation (4-19).

$$h_i = h_{C,i} + h_{r,i} \qquad (4\text{-}19)$$

Using the velocity data from the CFD simulation and the Phantom data from the experimental run conducted on Plant 1, a comparison was made as depicted in the following figure.

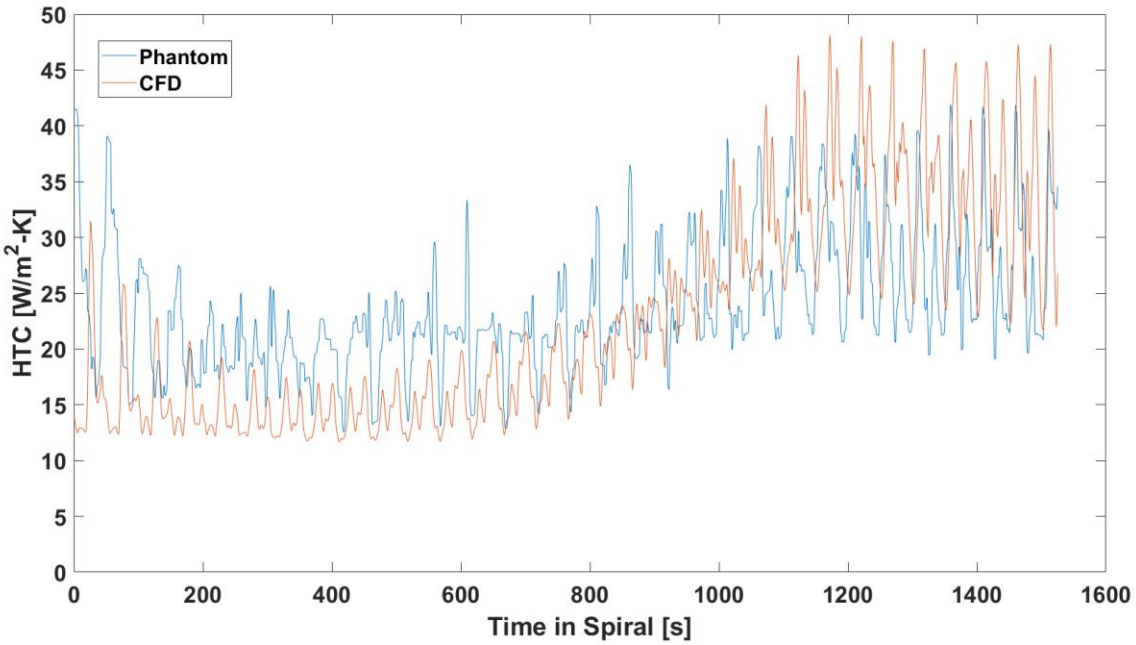

Figure (4.3): Heat transfer coefficient comparison between Phantom and CFD results for Plant 1.

Upon inspection of Figure (4.3), a cyclic pattern is observed in the data, which can be attributed to the variation in local velocity experienced on the spiral belt during each revolution of the spiral. As the position of each point gets closer or further away from a high velocity region, the heat transfer will increase or decrease, accordingly. Furthermore, there is qualitatively good agreement between the heat transfer coefficients predicted by the CFD simulation and those measured by the Phantom. However, a slight under-prediction is observed, on average, during the initial half of the data and a slight over-prediction in the latter half. While the exact cause of this discrepancy is unknown, it is possible that under-predicted porosity coefficients for flow through the levels of the spiral could be a contributing factor. An increase in resistance in the spiral belt's structure could be redistributing air flow to the upper portion of the spiral, which would result in the higher predicted heat transfer coefficients in the first half of the data since the product enters at the top of the spiral (time = 0 s) and exits at the bottom of the spiral (time = 1,604 s).

Heat flux data was also collected at the remaining three plants using the Phantom in a process as-described above. The respective CFD velocity results for each spiral freezer simulation were used to calculate heat transfer coefficients throughout the point cloud and compared against the heat flux data measured by the Phantom. The subsequent figure presents a comparative analysis of the data for Plant 2.

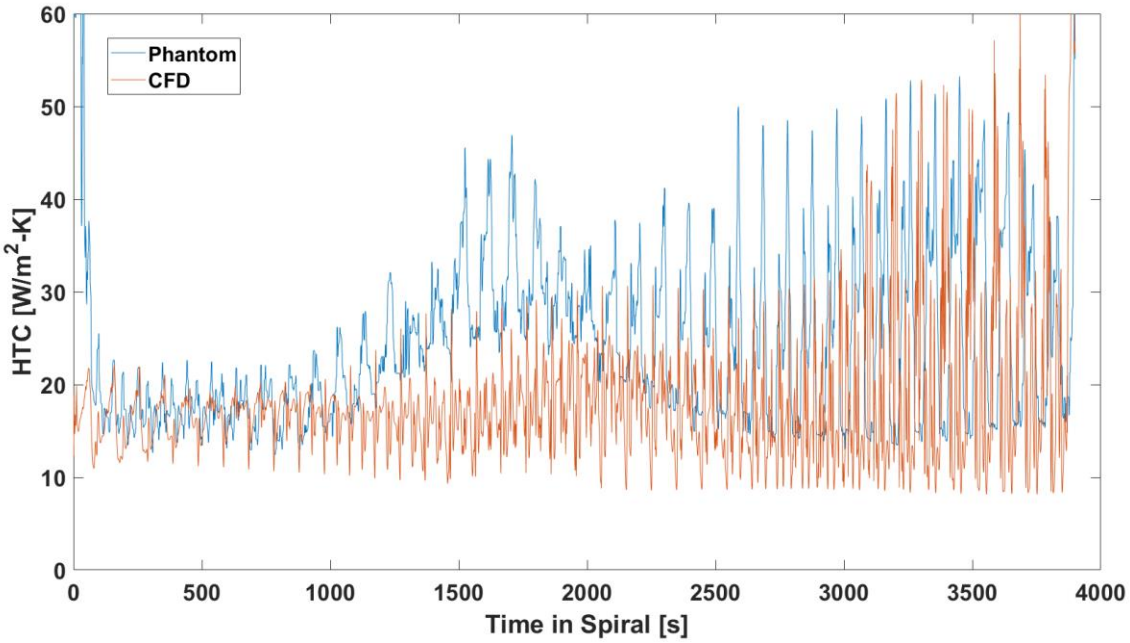

Figure (4.4): Heat transfer coefficient comparison between Phantom and CFD results for Plant 2.

From inspection of Figure (4.4), there is a dramatic reduction in the degree of agreement between the heat transfer coefficients obtained from the Phantom and CFD datasets. Both distributions exhibit a comparable general shape characterized by initially low heat transfer followed by a small peak, which rapidly decays before increasing toward the end of the dwell time in the freezer. Numerous factors could account for the differences between the CFD model-predicted heat transfer and the Phantom-measured heat transfer. For instance, it is possible that the removal of specific equipment components from the model resulted in flow disruptions that went unaccounted for in the CFD simulation. Moreover, while measurements were made for the non-dimensioned items in the detailed drawings, it is conceivable that some dimensions were subsequently altered during the construction of the spiral. For

example, if the distance from the floor to the walkway in the freezer differed from the provided drawing dimensions, the small peak in heat transfer occurring near the walkway opening would be displaced to the left for the Phantom, as depicted in Figure (4.4). Another probable source of error could be the use of 2D fan boundary conditions on the 3D surface of the centrifugal plug fans [32]. The 2D boundary conditions assume uniform flow normal to the surface, which could potentially result in an under-prediction of flow rates if applied to the outlet of a centrifugal fan. The outcome of a lower-than-expected flow rate would subsequently lead to decreased spiral velocities, as evidenced in the CFD data. Experimental comparisons for Plants 3 and 4 in **Appendix B**, as seen in Figure (B.3) and Figure (B.4), corroborate this finding. Notably, CFD models for Plants 1 and 3, with axial fans modeled by 2D surfaces, showed more consistent agreement with experimental results, while CFD models for Plants 2 and 4, with centrifugal plug fans modeled with 3D surfaces, exhibited less overall consistency with experimental results.

It should be acknowledged that there are certain limitations to the approach utilized here, as the heat transfer correlations employed do not perfectly align with the conditions experienced by the Phantom. Despite the CFD solver's ability to predict turbulent fluctuations, with the simplifications applied to the domain, it is unable to resolve micro-, small-, and even larger-scale turbulent eddies, potentially resulting in under-prediction of the heat transfer coefficients using the method herein. Additionally, the heat transfer correlation assumes that air is flowing parallel over the flat plate which disregards the vertical velocity components that actually exist in the spiral and are also seen in the CFD simulations. If the entering air angle has a considerable influence on heat transfer, the shallow air angles predicted by the CFD simulations may impact their comparison to the Phantom results. Furthermore, the Phantom measures real-time heat flux on the surface of the Phantom while the CFD model calculates temporally-averaged velocities. As a result, the velocity fluctuations experienced by the Phantom as it traverses through the physical spiral freezer could lead to more sporadic behavior in

recorded measurements, as observed in both Plant's comparisons. Lastly, the heat flux measurements being recorded by the Phantom is not without its own error. That being said, the comparisons being made are qualitative in nature, with emphasis placed more on the overall distribution shape rather than the specific numerical values themselves. Therefore, the level of agreement between the Phantom and CFD provides confidence that the methods and assumptions employed when modeling these systems are generally applicable.

Chapter 5 AIRSIDE MODIFICATIONS

Upon successful validation of the CFD models and their as-constructed baseline performance, research proceeded towards the exploration of strategies that aim to enhance airside performance. The outcomes of **Section 2.1.6** have demonstrated that the efficiency of a blast freezer can be enhanced primarily by incorporating more effective geometries that enable improved airflow over the product. In this regard, this chapter is focused on a comprehensive account of the principal design study conducted on the Plant 1 blast freezing system, alongside the corresponding models of each plant. The outcomes of proposed modifications via strategic placement of baffling elements for each plant's blast freezing system are compared both qualitatively and quantitatively with the as-constructed (baseline) blast freezing system.

5.1 Performance Criteria

To assess the airside performance and resulting operational efficiency, a set of five metrics were identified including: the average air velocity throughout the spiral (point cloud), the average face velocity of air across the evaporator coils, product throughput, unit product energy consumption, and the resulting annual CO_2 emissions. While additional metrics such as fan pressure rise and fan load were also predicted through the CFD simulations, their relative performance was not broken out separately; rather, their influence was incorporated within the calculations of the aforementioned performance metrics. Benchmark performance measures are established for the existing infrastructure for each plant and then proposed baffling modifications for each plant evaluated with a goal of identifying design modifications that would yield enhanced freezing system performance and efficiency. Details of each performance metric are introduced in the sections that follow.

5.1.1 Average Spiral Velocity

The "average spiral velocity" represents the magnitude of air velocity averaged across each of the points within the spiral's point cloud. All three component velocities for each point in the spiral's point cloud are exported from the converged CFD solutions, the magnitude of the velocity calculated, and average determined. The average spiral velocity is then reported as one of the overall performance metrics for airflow and a proxy for cooling performance for comparing the various design alterations. The cooling performance of a blast freezer is enhanced by higher average air velocity due to its increased surface convection across the product. Furthermore, comparing the average spiral velocity provides a rapid assessment of whether performance will undergo improvement or decline, and thus provides valuable insights for enhancing system design.

5.1.2 Average Coil Face Velocity

Despite the absence of a direct relationship between the average coil face velocity and product cooling performance, this metric provides a means for evaluating the ability of the evaporator to support increased product throughput when higher average spiral velocities are predicted. Lowering the average coil face velocity will tend to reduce the cooling capacity of the evaporator coils. Therefore, if a design leads to significantly lower coil face velocities, further evaluation would be needed to ensure the capacity of the evaporator coils do not become the limiting factor in the efficacy of the freezing system. Although the precise coil capacity was not calculated within the scope of this project, the effect of varying face velocities was qualitatively taken into consideration.

5.1.3 Product Throughput

The metric of "product throughput," $\dot{N}_{prod}$, represents the number of products, or pounds of product, the blast freezer can process per unit of time. Clearly this measure of performance is of prime

interest to food processing plants as it is a direct means of assessing the freezing capability of this energy-intensive process. Estimating product throughput requires considering not only average air velocity, but also the specific air velocity distribution flowing across the product as it progresses from the infeed to the outfeed of the blast freezing system. This is because a higher average air velocity does not necessarily translate to proportionally increased product throughput. Furthermore, estimating product throughput can aid companies in justifying the cost of design changes to their blast freezers, as it provides insight into the volume of product that can be processed and the potential for increased profitability. Calculating the "product throughput" relies on the use of a 1D transient numerical model with nonconstant thermal properties [30] along with velocity data from the CFD-predicted spiral point cloud. Results from the 1D product model are then input to a "spiral belt speed optimizer program" that is capable of determining the maximum belt speed to achieve the desired exit product temperatures based on prescribed product entering conditions [30]. By utilizing this methodology, companies can optimize product throughput to ensure products exit the freezer at the specified temperature while improving freezing efficiency and cost-effectiveness.

5.1.4 Product Normalized Energy Consumption

The "product normalized energy consumption," E_{prod}, represents energy consumed through the process of freezing food products. It reflects the total amount of electrical energy necessary to operate the freezer, including the house refrigeration system, in order yield a finished (frozen) single unit of product or kg of product. It is an important metric that aims to quantify the energy efficiency of a blast freezer while processing specific products. The per-product energy consumption is calculated using Equation (5-1),

$$E_{prod} = \frac{\dot{W}_{supplied}}{\dot{N}_{prod}} \qquad (5\text{-}1)$$

where $\dot{W}_{supplied}$ is the total power consumption to operate the freezer as calculated from the system energy balance given in **Section 2.1.6**. Lower normalized energy consumption means a blast freezer uses less energy to freeze a given product. Or alternatively, more product can be frozen while supplying the freezer with the same amount of energy.

5.1.5 Normalized Annual CO_2e Emissions

The "normalized annual CO_2e emissions" is metric intended to capture the environmental impact of blast freezers as a consequence of their electrical energy consumption. Estimates of the CO_2e that a freezer would emit in a year to process a fixed amount of product production, represented by, PPY_{base}, provides a measure of performance for the freezing systems "carbon footprint." The fixed amount of food production is determined from the plant's current product overall annual throughput, $\dot{N}_{prod,base}$, as calculated with Equation (5-2),

$$PPY_{base} = \dot{N}_{prod,base}\, t_{year} \qquad (5\text{-}2)$$

where t_{year} is the number of minutes the freezer is expected to operate in a typical year. The time is assumed to reflect a production operating period of 20 hours per day and six days per week for 50 weeks per year. To calculate the annual CO_2e emissions, EPY, Equation (5-3) is used,

$$EPY = PPY_{base}\, E_{prod}\, EF \qquad (5\text{-}3)$$

with EF representing the regional emissions factor for the given plant location [[33]. This factor considers the region's electricity product resource mix and reflects the effective CO2 emissions per unit electrical energy delivered. Emission factors are higher in regions that, primarily, rely on coal-based fossil fuels for electricity production. Table (5.1) details the emissions factor for each plant based on the fuel mix used for electricity production in the plant's specific geographic region.

Table (5.1): Emissions Factor for each plant, data from [33].

Plant	Plant 1	Plant 2	Plant 3	Plant 4
Emissions Factor [lb CO_2e/MW-hr]	**1,052.5**	**1,592.3**	**1,592.3**	**1,003.1**

It should be noted that the exact resource breakdown for each plant's electricity consumption is not explicitly known but assumed to be equal to reported aggregate values for the region.

The significance of the normalized annual emissions is highlighted by the fact that a design capable of handling higher product throughput rates would require fewer minutes of operation to process the same annual production total, resulting in lower overall emissions and increased environmental sustainability, contributing to the ultimate goal of this research.

5.2 Plant 1

5.2.1 Base Model

The bulk of this research has focused on Plant 1's blast freezer, which not only served as the initial case study for the energy balance model but also the initial design study that laid the groundwork for future proposed airside modifications that also informed options for the remaining three plants.

Plant 1's blast freezer is a single-pass configuration, wherein, from the discharge of the freezer's fans to the face of evaporator coils, air travels across product being conveyed on the spiral belt only once. Within the Plant 1 blast freezer are six axial fans that pull air through the evaporator coils and discharge the air across the top of the spiral belt receiving in-fed product to be frozen. Access to the product infeed inside the freezer is via. a second story walkway. The walkway is partitioned, with the half towards the fans being solid and the other half being circularly-perforated, Figure (5.1a). However, to minimize airflow restrictions, the perforated portion was removed by the plant before the

development of the initial baseline CFD simulation of the blast freezer, as can be seen in Figure (5.1b). As a result, Plant 1 was modeled without the perforated section as the base model and for all subsequent design simulations.

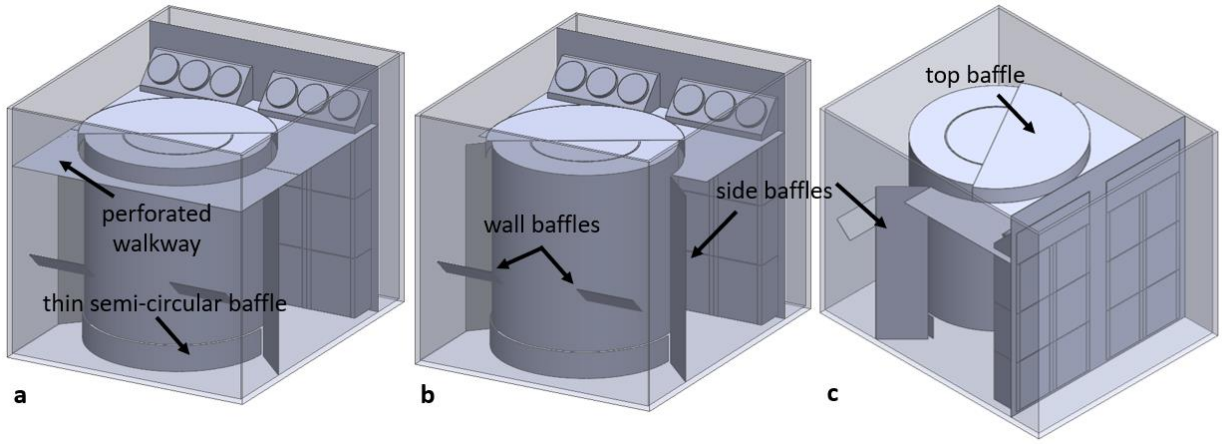

Figure (5.1): 3D model of Plant 1's spiral blast freezer, front-side view, before and after walkway removal (a) and (b), and back-side view (c).

From the figure, one can see that there are several baffling elements, namely, the two side and wall baffles, and a thin semi-circular baffle underneath the spiral. Additionally, a baffle covering the top of the spiral was added by the plant early in the start-up of the freezing system to prevent the dough product from being blown off the belt due its exposure to the high velocity air being discharged from the fans. It should be noted that this freezer's product flow is configured such that the entering product starts at the top of the spiral, with the frozen product exiting at the bottom.

The product that Plant 1 processes within this specific blast freezer is a partially baked flat circular shaped dough product. The corresponding table provides details on the entering and desired exiting temperatures, as well as the amount of internal energy that needs to be extracted from the product to achieve those temperatures, and the current product throughput capacity.

Table (5.2): Product and throughput information for Plant 1.

Food Product	Start Temp. [K]	End Temp. [K]	Internal Energy to Cool [J/prod] (J/kg)	Current Throughput [prod/min]
Dough Product	**311**	**261**	**133,932 (235,839)**	**146.6**

By utilizing the porous media resistances found in **Appendix A** outlined in Table (A.2) through Table (A.4) for Plant 1, along with the fan curve coefficients tabulated in Table (A.5), and the fluid properties for air described in Table (A.1), the CFD simulation for Plant 1's base configuration was solved. The resulting velocity streamlines were subsequently obtained from the Ansys® post-processor as shown in Figure (5.2). The spiral air velocity distribution, expressed as a function of time, for this simulation is also displayed in Figure (5.3) for further analysis. The temporal nature of this velocity distribution is related to the physical position of the product within the spiral enclosure since the belt runs at a constant speed.

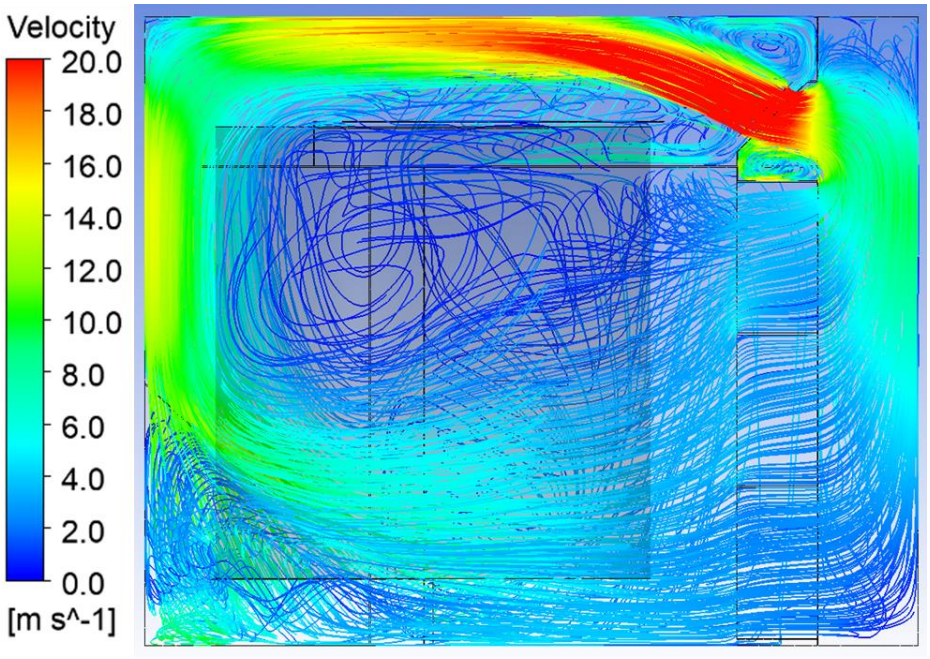

Figure (5.2): Velocity streamlines for Plant 1's base model.

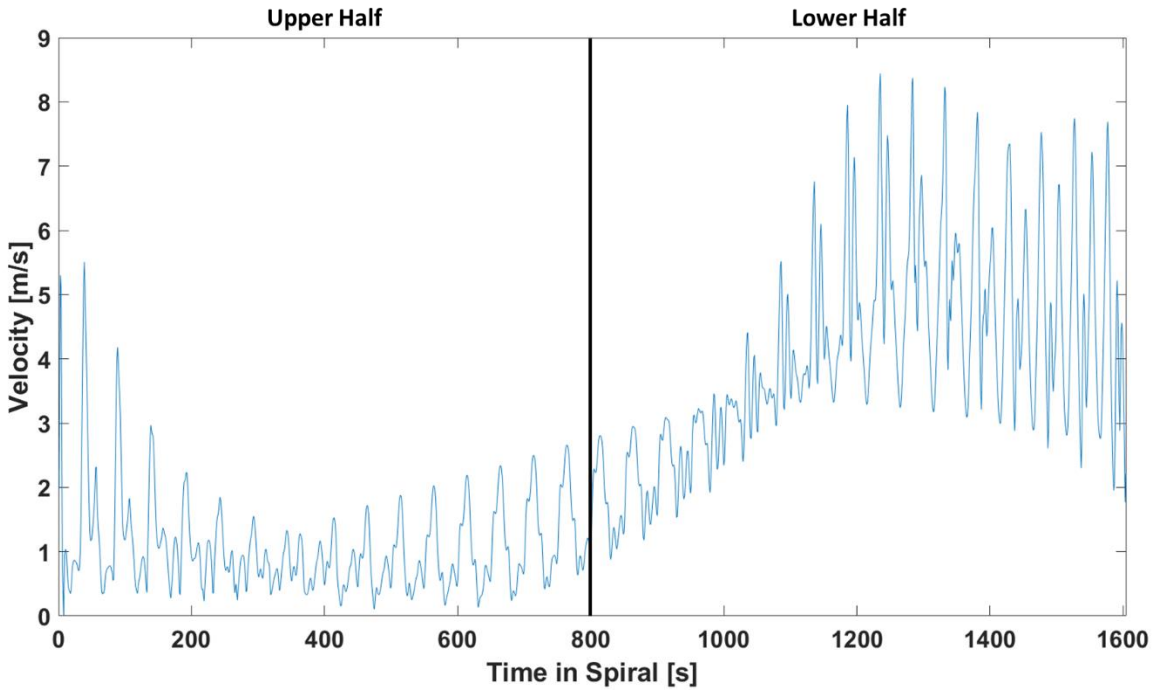

Figure (5.3): Spiral velocity distribution inside Plant 1's base model, lower and upper half of spiral labeled.

Based on the presented figures, it is evident that the velocity distribution within the spiral exhibits a significant variance between the upper portion of the spiral vs. the lower portion of the spiral. Specifically, the lower portion of the spiral, spanning from the 1,000 to 1,600 sec mark, displays a higher airflow rate, almost three times greater than that of the upper section. Table (5.3), summarizes the performance metrics resulting from the CFD simulation and the results from the 1D product model used to calculate product throughput and the energy balance program used to calculate normalized product energy consumption and annual emissions.

Table (5.3): Summary of performance metrics for Plant 1's base model.

Spiral Velocity [m/s]	Coil Face Velocity [m/s]	Product Throughput [prod/min]	Energy per Product [kJ/prod]	Annual Emissions [lb CO_2e/year]
2.56	**2.90**	**146.6**	**223.3**	**3,446,000**

5.2.2 Design Study

After further examination of the base model results of Plant 1, several areas for potential improvement of air-side flow were hypothesized. One area that initially stood out was the hard 90-degree corners present in the upper edges of the spiral enclosure. Similar to large pressure drop through a hard bend in a pipe, it was theorized that reducing these sharp corners could facilitate turning the air flow and conserve its momentum.

Another issue was the significant disparity in air flow distribution between the upper half and lower half of the spiral. For this particular freezing system, warm product enters at the top of the spiral; therefore, it would be beneficial if product in this region is exposed to higher air velocity to achieve an increased heat transfer rate in contrast to the current air velocity distribution. From a fluid dynamic perspective, pressure drop through the spiral belt structure approximately scales with velocity squared; therefore, an uneven distribution of velocity increases the overall pressure losses across the spiral.

With further inspection of the streamlines, it was discovered that a sizable proportion of the air flow was bypassing the spiral, which in turn led to energy wastage. It requires energy to move air around the freezer; therefore, every time the air flow circulated around the freezer without coming into contact with the product, energy is lost.

Lastly, air recirculation zones and air flow separation occurring in empty regions within the freezer, such as the left and right of the side baffles, and below the two baffles on the back wall, can further degrade freezing performance. These regions, which can be seen in Figure (5.4), cause the flow to lose momentum, resulting in a significant decrease in local velocity. Additionally, these regions generate turbulent eddies, which dissipate momentum and convert kinetic energy into heat that further needs to be removed by the evaporator coils, thus negatively affecting performance two-fold. While

free space is essential for adequate access to equipment, minimizing these regions could lead to more efficient flow.

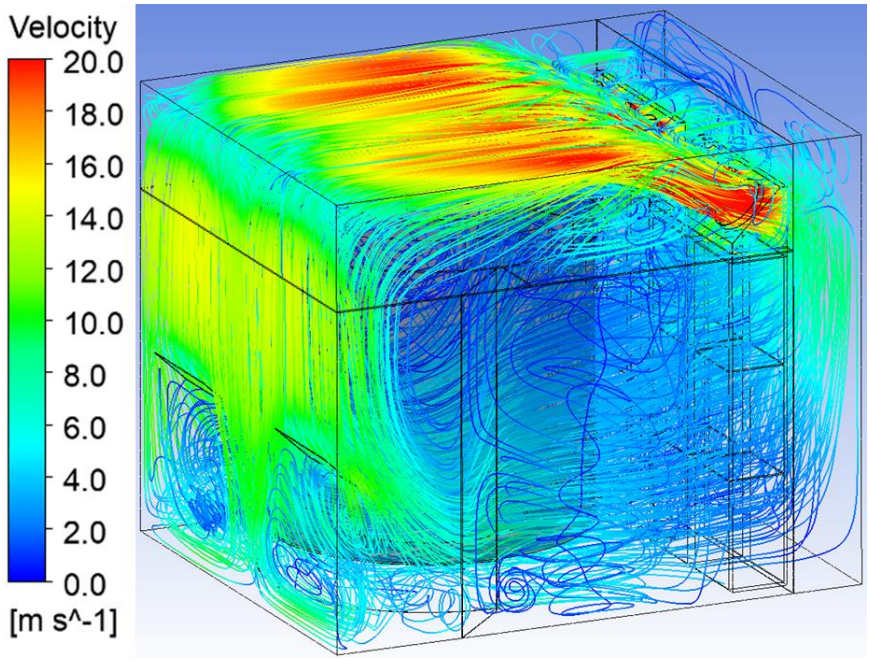

Figure (5.4): Velocity streamlines for Plant 1's base model, alternate view.

A design study, conducted on Plant 1's blast freezer, aimed to address the hypothesized improvement areas. Five designs were developed and Figure (5.5) through Figure (5.6) below, highlight key features intended to facilitate improvements in air flow within the spiral. Each permutation was evaluated and their individual effects on the performance metrics quantified.

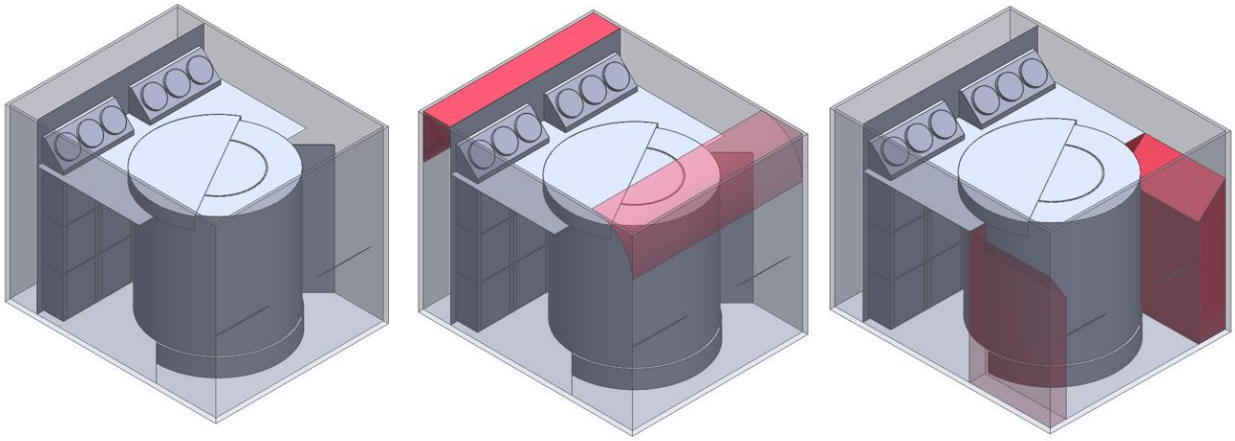

Figure (5.5): Designs 1 and 2 compared against the base model for the design study conducted on Plant 1, added baffles identified in red.

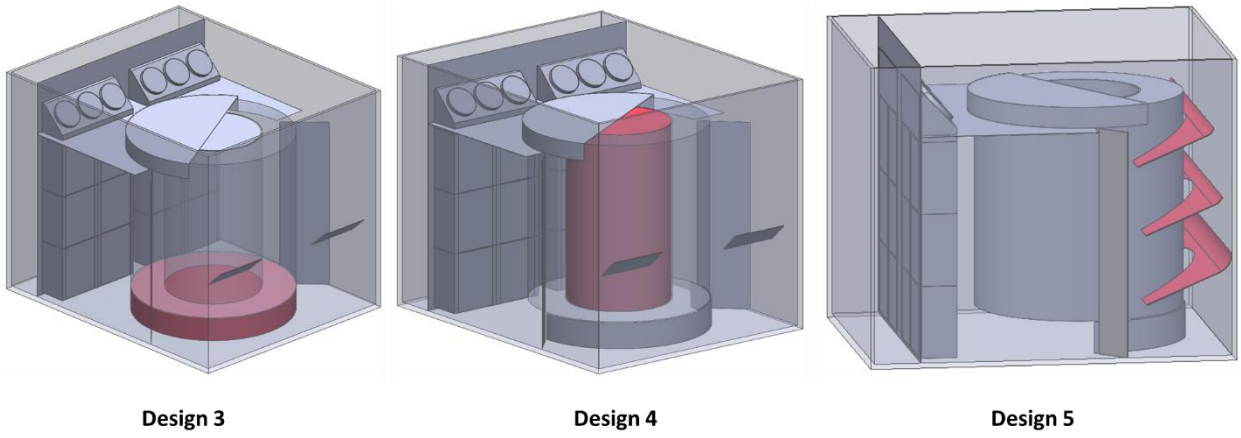

Figure (5.6): Designs 3 through 5 for the design study conducted on Plant 1, added baffles identified in red.

Design 1 incorporates two large baffles in the upper corners, perpendicular to the flow direction. These baffles feature a large radius bend, potentially mitigating the effect of hard 90-degree corners on the incoming flow.

Design 2 introduces rectangular prism baffles, situated in the lower back wall corners with inclined surfaces back swept into the side walls. This design aims to reduce the presence of empty space regions and the resultant flow recirculation within those areas.

Design 3 includes a thick “disk” below the spiral belt to prevent air flow bypass that occurs beneath the spiral. This disk is completely enclosed and hollow inside; thereby, preventing flow from passing through the last levels of the belt that was not previously possible with the semi-circle strip that only blocked flow normal to its radial surface.

Design 4 utilizes a solid baffle “drum” within the interior of the spiral belt itself and includes two solid “caps” on the top and bottom of the spiral. This design aims to prevent air flow from passing through the spiral support structure and forcing the air to flow around the spiral drum and over the product. Design 4 attempts to address both air flow bypass as well as regions of empty space.

Design 5 features three angled baffles spaced progressively closer to the back wall moving downward, with a semi-circular cut in them that wraps around the edge of the spiral. These baffles have a slight bend towards the wall side to entrain progressively greater portions of the supply flow discharging from the fans and distributing the air more evenly throughout the spiral, particularly to the upper levels of the spiral; thereby, addressing the uneven distribution of flow in the current freezing system.

All five designs were solved in Ansys® Fluent using the same inputs as Plant 1’s base model. The velocity streamline results compared against the base model can be seen in the following two figures.

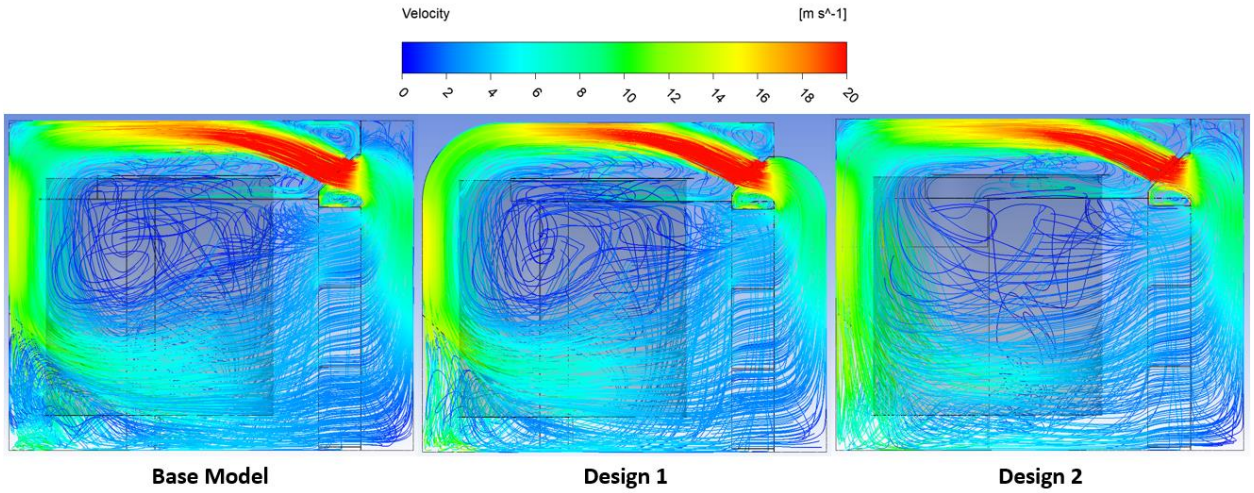

Figure (5.7): Velocity streamlines for designs 1 and 2, compared against Plant 1's base model.

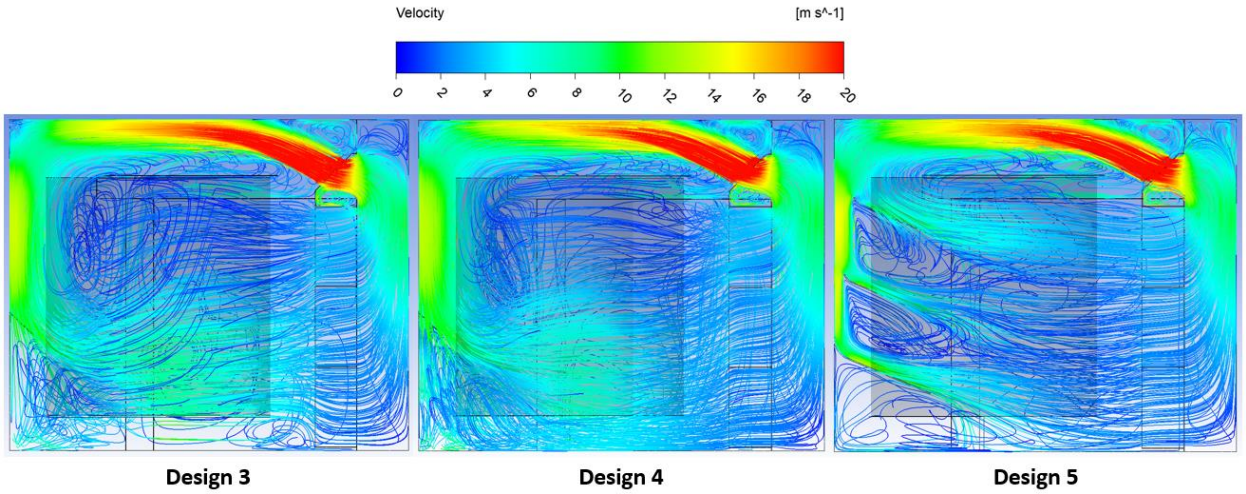

Figure (5.8): Velocity streamlines for designs 3 through 5.

Additionally, spiral velocity distributions for the six models were plotted, Figure (5.9), to better identify each designs' effect on the flow.

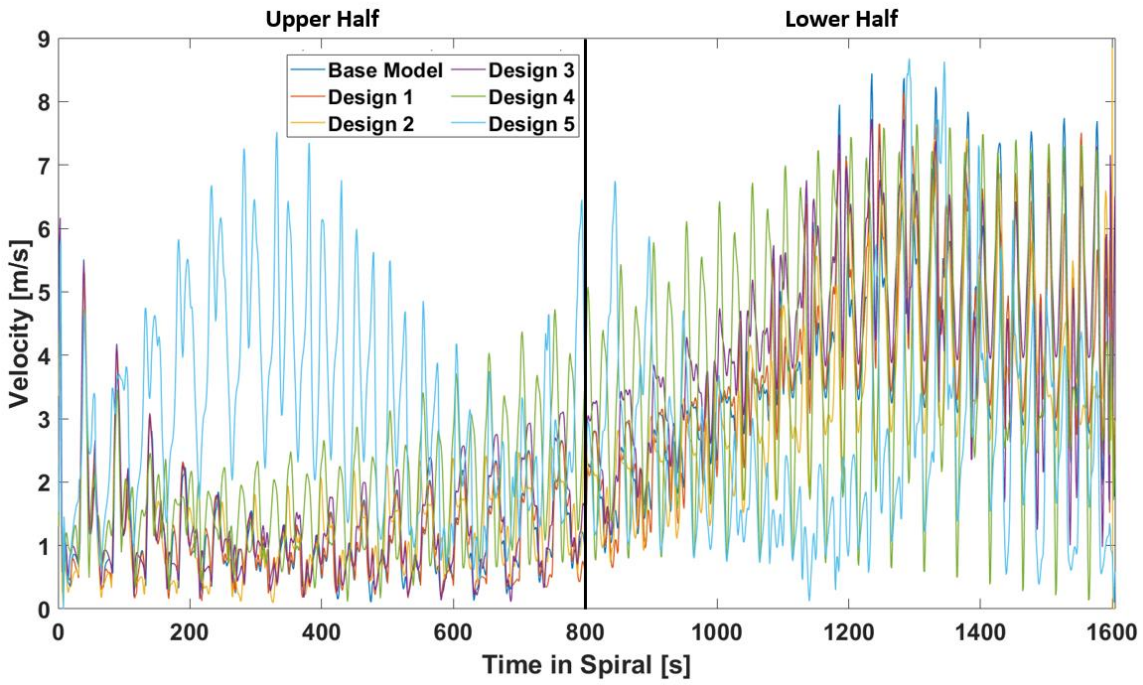

Figure (5.9): Spiral velocity distributions for designs 1 through 5 compared against the base model, for Plant 1. Lower and upper half of spiral labeled.

Because of the highly oscillatory nature of the air velocity distributions, the comparison between three or more velocity profiles makes discerning their relative behavior difficult. As such, subsequent plots that compare the air velocity temporal distributions were smoothed using a moving average defined by the number of moving points, M, included in the moving average. The base model result will still provide the full velocity detailed velocity distribution to get an understanding of the peak-to-peak range of the velocity oscillations. Figure (5.10) displays the smoothed spiral velocity distributions for the six models.

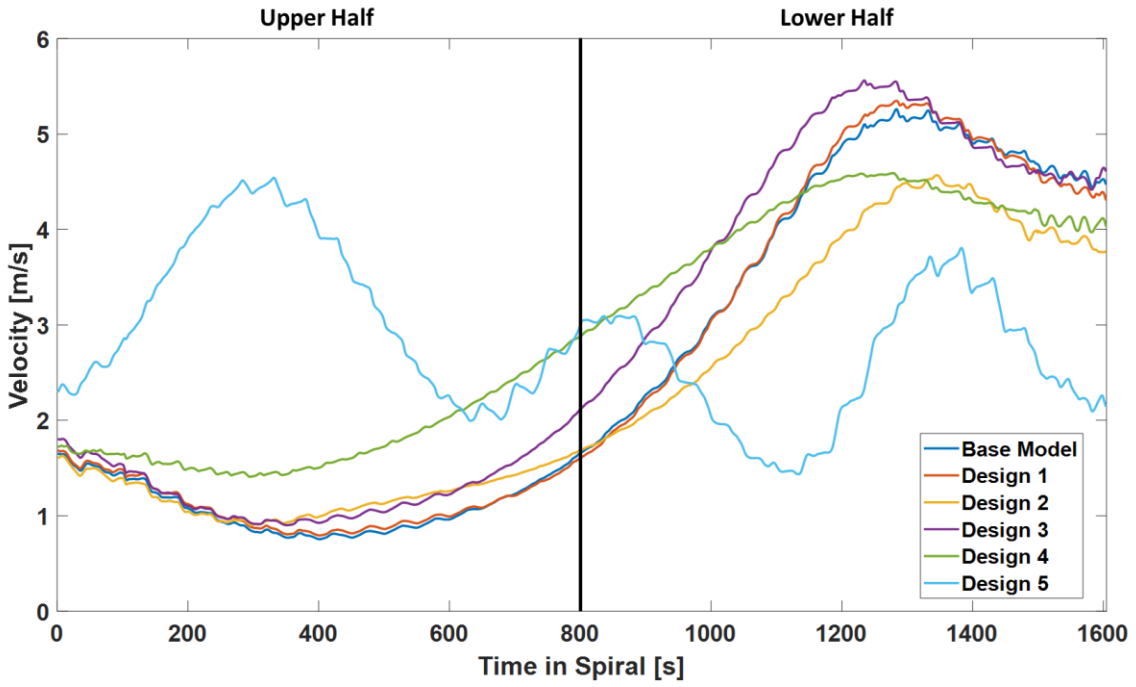

Figure (5.10): Smoothed, (M=200), spiral velocity distributions for designs 1 through 5 compared against the base model, for Plant 1. Lower and upper half of spiral labeled.

Analysis of Figure (5.7) and Figure (5.10) reveals that Design 1, which entailed rounding off the upper corners, had a negligible impact on the airflow. Surprisingly, Design 2 resulted in worse performance in the lower portion of the spiral after 850 seconds. In Figure (5.7) it can be seen that the baffles implemented in Design 2 only served to accelerate the flow along the back wall and underneath the spiral. In contrast, Design 3 displayed a slight improvement over the base case as the air flow was no longer bypassing underneath the spiral. This, in turn, caused a greater proportion of the overall airflow to pass across the spiral; thereby, shifting the velocity distribution upward in magnitude, as evidenced in Figure (5.10).

Design 4 demonstrated a meaningful change in the overall air flow distribution. Specifically, it resulted in an increase in air flow towards the upper half of the spiral, as more air was forced to travel along the curving belt instead of passing through the spiral's structural supports. Conversely, towards the bottom quarter of the spiral, the air flow takes an alternative route, passing through the belt and

underneath the spiral as it came into contact with the solid core baffle, as evidenced by the reduced air velocity.

Notably, the distribution of Design 5 appears unrecognizable from the base model. This is attributed to the three baffles, which distributed the flow more uniformly, as shown by the tri-modal pattern observed in Figure (5.10). Additionally, the incoming product, which is the warmest, experienced the largest airflow; thereby, the maximum convective heat transfer across the product.

Table (5.4) presents the summary of the CFD simulations results and the following product throughput and energy balance analyses. The table additionally identifies the percentage change of each performance metric relative to the base model.

Table (5.4): Performance metric results from design study, red/green indicates worst/best performers in respective metric. Δ% indicates the percent change relative to the base model's respective result.

Model	Spiral Velocity [m/s] (Δ%)	Coil Face Velocity [m/s] (Δ%)	Product Throughput [prod/min] (Δ%)	Energy per Product [kJ/prod] (Δ%)	Annual Emissions [lb CO_2e/year] (Savings)
Base Model	**2.56 (-)**	**2.90 (-)**	**146.6 (-)**	**223.3 (-)**	**3,446,000 (-)**
Design 1	**2.57 (0.4)**	**2.79 (-3.8)**	**147.4 (0.6)**	**222.6 (-0.3)**	**3,434,000 (12,000)**
Design 2	**2.32 (-9.4)**	**2.89 (-0.3)**	**140.0 (-4.5)**	**230.0 (3.0)**	**3,548,000 (-102,000)**
Design 3	**2.84 (10.9)**	**2.87 (-1.0)**	**157.1 (7.2)**	**213.9 (-4.2)**	**3,300,000 (146,000)**
Design 4	**2.94 (14.8)**	**2.89 (-0.3)**	**164.1 (11.9)**	**208.3 (-6.7)**	**3,214,000 (232,000)**
Design 5	**2.86 (11.7)**	**2.83 (-2.4)**	**165.8 (13.1)**	**207.0 (-7.3)**	**3,194,000 (252,000)**

The quantitative metrics show the Design 2 exhibited the poorest performance among the five designs and was the only one to observe a reduced average spiral velocity. In contrast, Designs 3 through 5 demonstrated a considerable increase in spiral air velocity, ranging between 11-15%, which resulted in an improvement in product throughput capacity of 7-13%. The spiral's capacity to process more product with the same fan power translates into a potential 4-7% reduction in the unit product energy consumption. For a fixed annual production amount, Designs 4 through 5 are estimated to save

150,000-250,000 lb of emitted CO_2e. Interestingly, Design 5 saw the largest improvement in product throughput despite not having the greatest increase in spiral air velocity. This underscores the importance of directing more airflow across the warm product entering the blast freezer to maximize the heat transfer potential.

The key findings of this study indicate that, first, baffles to reduce 90-degree corners had a negligible impact on performance of this blast freezing system. Second, removing empty space needs to be done strategically, as it should not compromise other areas of improvement for the air flow within the spiral. For instance, Design 2 would, ideally, have a solid baffle below the spiral to avoid magnifying air bypass. Third, reducing air flow bypass, either underneath, above, or through the center of the spiral, is a simple yet effective way to improve the overall freezing performance of the spiral. Fourth, distributing airflow to achieve higher velocity earlier in the product's dwell period can have the most significant potential for improvement. In other words, air flow with a uniform velocity throughout the spiral or higher velocity (front-loaded) across the product early in its dwell period will enhance overall freezing performance better than high velocity late in the dwell period (back-loaded distribution).

In summary, this study underscores the importance of implementing purposeful design enhancements that consider the interplay between various design features that aim to improve velocity distributions over the food product being frozen. Furthermore, it illuminates the specific baffle modifications that can yield the most substantial results, thus serving as a valuable guide for refining the designs of the three remaining plants.

5.2.3 Design Modifications

Elements of the five design study models were integrated together in an effort to achieve even greater overall freezing performance and energy efficiency. The two integrated designs are displayed in Figure (5.11).

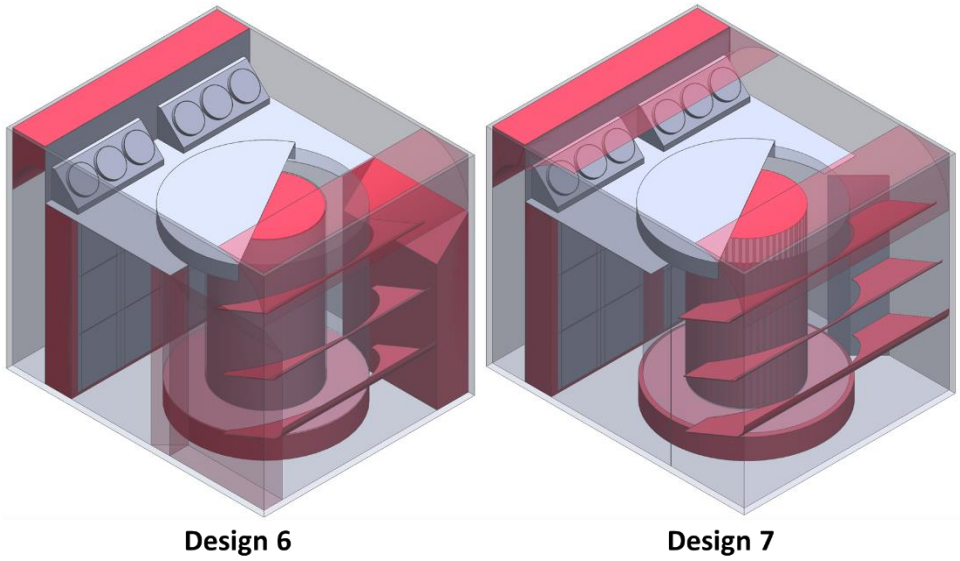

Figure (5.11): 3D models for Plant 1's designs 6 and 7.

Design 6, which utilizes all five design elements, was conceived to determine whether the degradation in performance that occurred in Design 2, side rectangular prism baffles, could be remedied by incorporating a baffle beneath the spiral to eliminate the bypass that was observed in Design 2. Design 7 incorporates the elements of Design 1 and designs 3 through 5, which have been individually shown to improve airflow performance. Additionally, Design 7 incorporates an extra curved baffle close to the fan outlet to mitigate the common recirculation that occurs in that region. Both integrated designs incorporate a baffle on either side of the coil stacks to eliminate the possibility of recirculation as the air enters the evaporator. Figure (5.12) and Figure (5.13) display the velocity streamlines and spiral velocity distribution of these two designs.

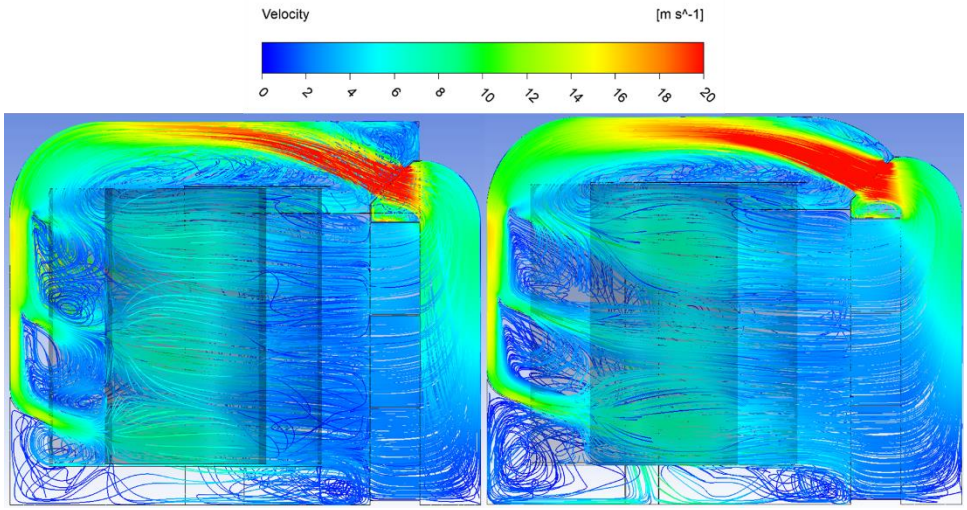

Figure (5.12): Velocity Streamlines for Plant 1's Design 6 and 7.

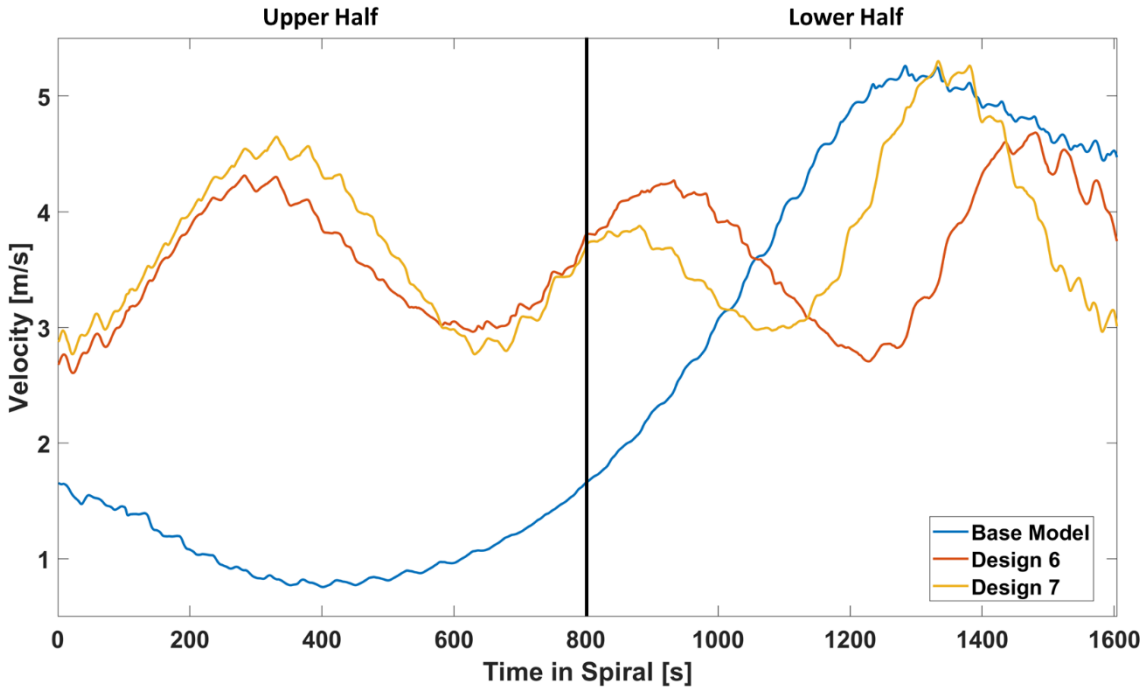

Figure (5.13): Smoothed, (M=200), spiral velocity distributions for designs 6 and 7 compared against the base model, for Plant 1. Lower and upper halves of spiral labeled.

The figures indicate that both designs achieved a substantial improvement in performance compared to the base model. Furthermore, both designs exhibit a tri-modal velocity distribution, which can be attributed to the implementation of three angled baffles on the back wall. This feature results in a notable improvement in the uniformity of airflow distribution throughout the spiral, particularly in the

upper region where warm product enters. Interestingly, it appears that the side baffles of Design 2 no longer hinders the overall air-side performance of the freezing system when used in conjunction with a baffle that prevents bypass underneath the spiral. A comprehensive summary of the performance metrics of these two designs, compared against the base model, can be found in Table (5.5).

Table (5.5): Performance metric results from Design Modification Analysis for Plant 1.

Model	Spiral Velocity [m/s] (Δ%)	Coil Face Velocity [m/s] (Δ%)	Product Throughput [prod/min] (Δ%)	Energy per Product [kJ/prod] (Δ%)	Annual Emissions [lb CO_2e/year] (Savings)
Base Model	**2.56 (-)**	**2.90 (-)**	**146.6 (-)**	**223.3 (-)**	**3,446,000 (-)**
Design 6	**3.60 (40.6)**	**2.85 (-1.7)**	**192.0 (30.9)**	**190.0 (-14.9)**	**2,931,000 (515,000)**
Design 7	**3.73 (45.7)**	**2.83 (-2.4)**	**195.7 (33.5)**	**188.0 (-15.8)**	**2,900,000 (546,000)**

The data presented in the table indicates that both designs have achieved a significant increase in average spiral velocity, ranging from 40-45%. This improvement surpasses the cumulative effect of each of the five individual design elements, suggesting that the interplay of design elements is not a linear one, but rather, each element has a mutually reinforcing effect on the others, leading to an overall freezing performance boost. With such an impressive surge in spiral velocity, it is conceivable that both of the designs could process over 30% more product, translating into a corresponding reduction in per-product energy consumption of at least 15%. This reduction could, potentially, lead to a significant decrease of up to 550,000 pounds in annual production-related CO_2e emissions; thereby, enhancing environmental sustainability of the freezing process.

5.2.4 Frost Accumulation

The accumulation of frost on component surfaces due to moisture sources that include air infiltration and water loss from products being frozen can have a significant impact on the performance of evaporator coils serving the blast freezing systems. While evaporator coils are equipped with defrost cycles to mitigate the effects of frost buildup, frost accumulating on fan guards is often overlooked.

These guards, which are installed for safety reasons, can accumulate a considerable amount of frost, reducing the area available for flow and compromising the overall performance of the freezing system. Plant 1 experienced significant challenges with frost accumulation on fan guards sited on the discharge side of the fans as evidenced by the substantial frost buildup shown in Figure (5.14). The added air-side pressure drop across the fans reduces the overall air flow rate of each fan which in turn decreases air velocity throughout the freezing system.

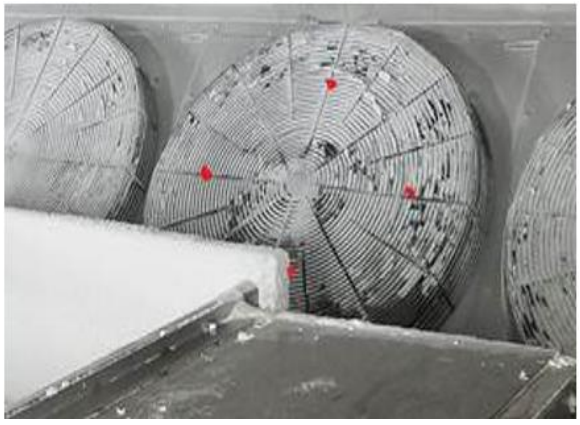

Figure (5.14): Frost accumulation on guards of fan's exhaust.

To address the problem of frost clogged fan guards, a new design featuring long throw adapters (LTAs) was proposed. These adapters are, essentially, extensions off the fan discharge that are long enough to prevent personnel limb contact with spinning fan blades, thus enabling the removal of tightly meshed fan guards currently installed. Additionally, the LTAs can be bent at a 45-degree angle to direct the flow along the ceiling of the blast freezer, offering the potential for improved supply air flow. Figure (5.15) shows the existing installation with fan guards in contrast to the proposed LTAs.

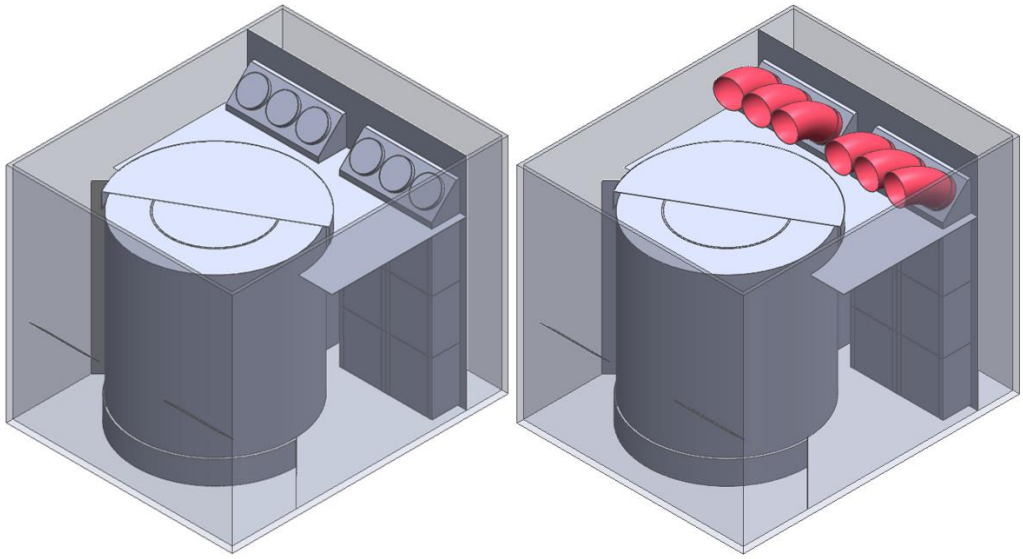

Figure (5.15): Proposed long throw adapters compared against Plant 1's base model, added baffles identified in red.

To understand the potential benefits of incorporating long throw adapters (LTAs) into a freezer design, the impact of frost buildup on fan guards must be evaluated. As such, a small-scale CFD study was conducted to determine the pressure drop through progressively frosted fan guards as a function of the discharge air velocity off the fans. The results of this small-scale study can then be scaled to adjust the fan curve used in the base blast freezer CFD model to account for the frosting of the discharge fan guard. The study involved creating a 3D model of the physical fan guards used in the current blast freezer design in Plant 1, as shown in Figure (5.16a).

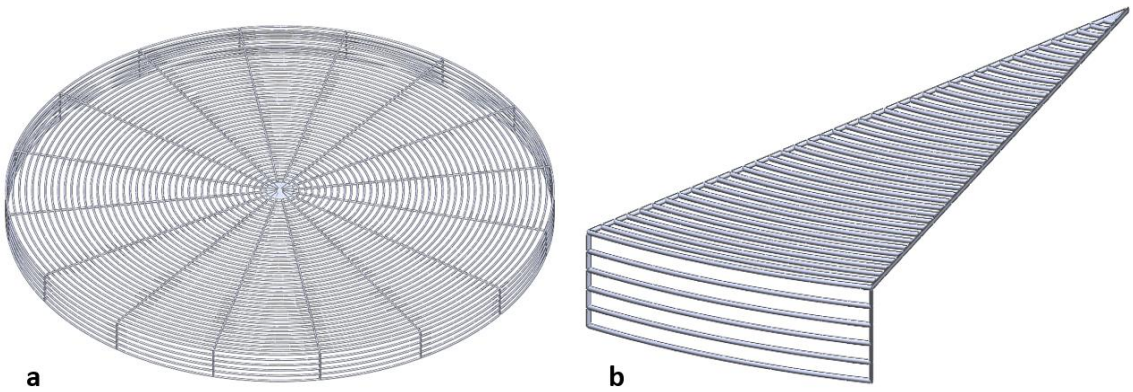

Figure (5.16): Full fan guard, reduced symmetric section.

To simplify the geometry, and therefore the CFD model, symmetry is applied by dividing the circular fan guard into 16 identical sections and only one fan guard section simulated. Air flow was directed normal to the fan guard with a uniform inlet air velocity profile. Frost accumulation was accounted for by varying the thickness of the wire loops used to construct the guard, and four different amounts of frost buildup were modeled, as depicted in Figure (5.17), where the amount of frost accumulation is defined as a radial thickness.

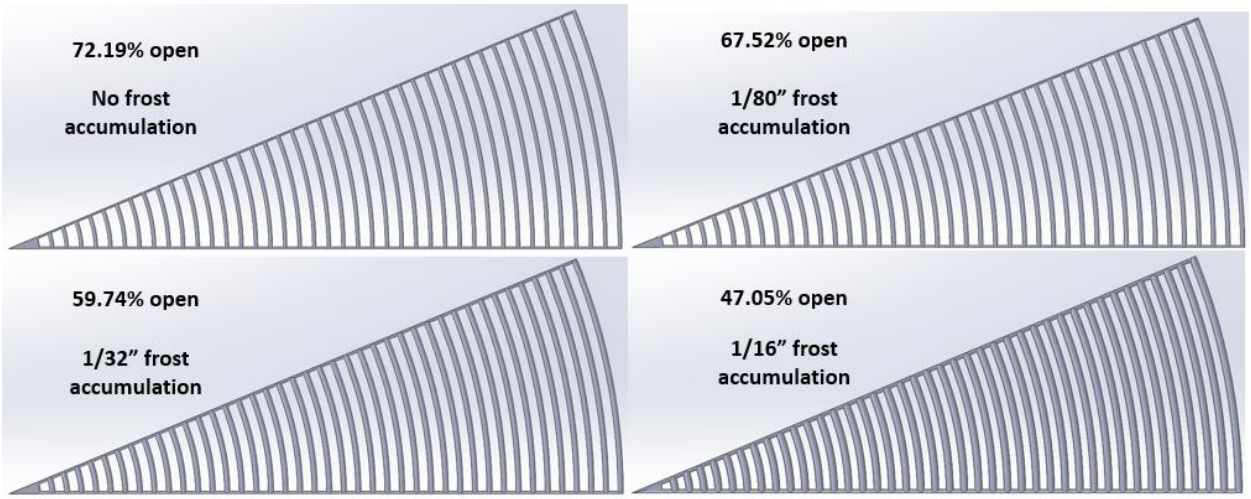

Figure (5.17): 3D models of the four different levels of frost accumulation modeled, with respective open percentages.

Additionally, the open area percentage, σ, was calculated for each case using Equation (5-4),

$$\sigma_a = \frac{A_{flow}}{A_{tot}} \qquad (5\text{-}4)$$

where A_{flow} and A_{tot} are the available area for flow and total area of the section, respectively.

To determine the air-side pressure drop across the fan guard itself, the symmetric fan guard section was enclosed in a "digital test section," as illustrated in Figure (5.18) and the pressure of air was recorded upstream and downstream of the guard. Inlet velocity was varied from 0 to 30 m/s for each of the four levels of frost accumulations and the summary of the pressure drop summarized in Table (5.6).

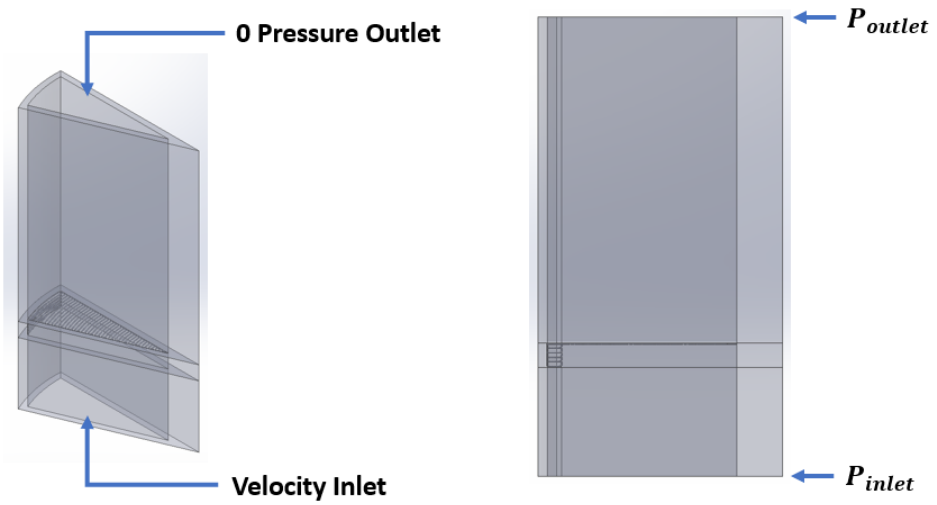

Figure (5.18): Computational domain for fan guard study.

Table (5.6): Pressure drop vs. velocity for the four frost accumulation levels.

Inlet Velocity [m/s]	Pressure drop [Pa]			
	Frost Accumulation [in]			
	No frost	1/80th	1/32nd	1/16th
0	0	0	0	0
1	0.33	0.45	0.69	1.41
2.5	1.90	2.57	3.93	8.08
5	7.32	9.96	15.07	30.47
10	26.45	36.20	57.77	116.75
15	53.16	73.21	120.54	247.76
20	86.53	119.33	200.80	419.91
25	128.34	178.82	297.15	629.28
30	176.75	247.28	411.27	875.78
35	231.86	323.95	541.88	1155.36

As expected, the experimental results indicated that the air-side pressure drop increased with both the flow velocity and the degree of frost accumulation. The pressure drop data was fitted to a 2nd order polynomial for each of the four cases and the resulting coefficients were used to modify the fan curve in the blast freezer simulation model to account for the impact of frost buildup. This alteration shifted the operating point of the fan curve to differential pressures that resulted from the increasing fan discharge

pressure due to frosting which, ultimately, reduces the volume flow rate the fan can deliver. Table (5.7) details the adjustments made to the a_1 and a_2 coefficients of Plant 1's fan curve.

Table (5.7): Modification to Plant 1's fan curve for the four amounts of frost accumulation.

Frost Accumulation [in]	Subtraction to a_1 Coefficient	Subtraction to a_2 Coefficient	Upper Limit Velocity [m/s]
No frost	**1.1455**	**0.1576**	**26.86089**
1/80th	**1.479**	**0.2239**	**25.57042**
1/32nd	**2.2933**	**0.3793**	**25.19741**
1/16th	**4.0229**	**0.8344**	**24.22196**

After implementing the adjusted fan curves, the base CFD model for Plant 1 was re-simulated, and the performance measures that include the average spiral velocities, average coil velocities, and fan flow rates were recorded in Table (5.8).

Table (5.8): Results summary of fan guard's effect on Plant 1's base model.

Frost Accumulation [in]	Open Percentage [%]	Spiral Velocity [m/s]	Coil Velocity [m/s]	Fan Flow Rate [m^3/s-fan]
No fan guards	**100.00**	**2.56**	**2.90**	**17.63**
No frost	**72.19**	**2.46**	**2.79**	**17.07**
1/80th	**67.52**	**2.43**	**2.76**	**16.88**
1/32nd	**59.74**	**2.35**	**2.69**	**16.42**
1/16th	**47.05**	**2.16**	**2.50**	**15.29**

Subsequently, the design with the proposed LTAs was simulated and the velocity streamlines can be seen in Figure (5.19). Additionally the spiral velocity distributions for the base model without fan guards, with fan guards, unfrosted and frosted, and the LTAs are plotted in Figure (5.20).

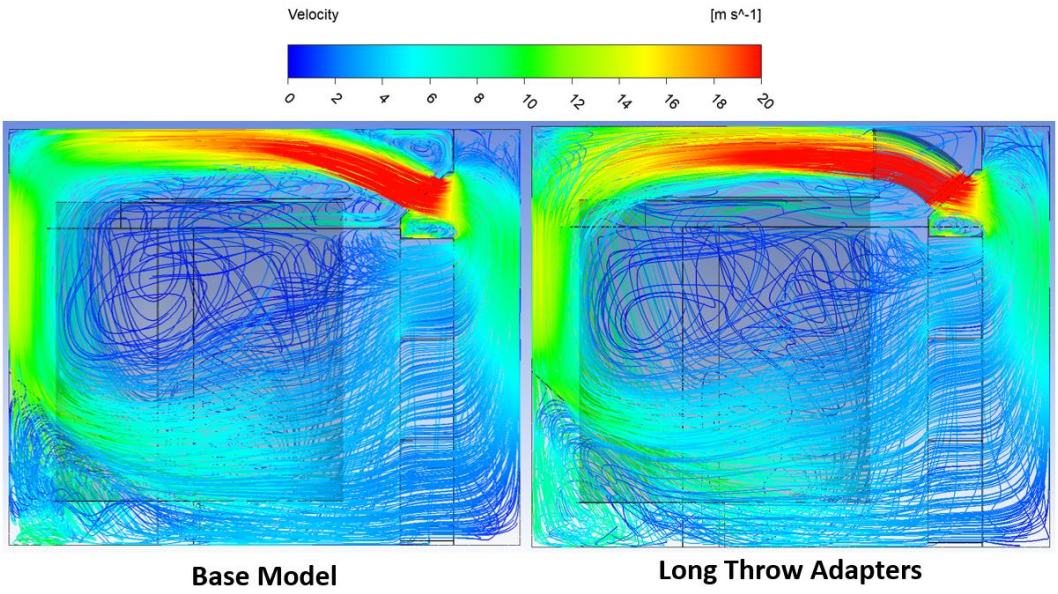

Figure (5.19): Velocity streamlines for proposed long throw adapters compared against Plant 1's base model.

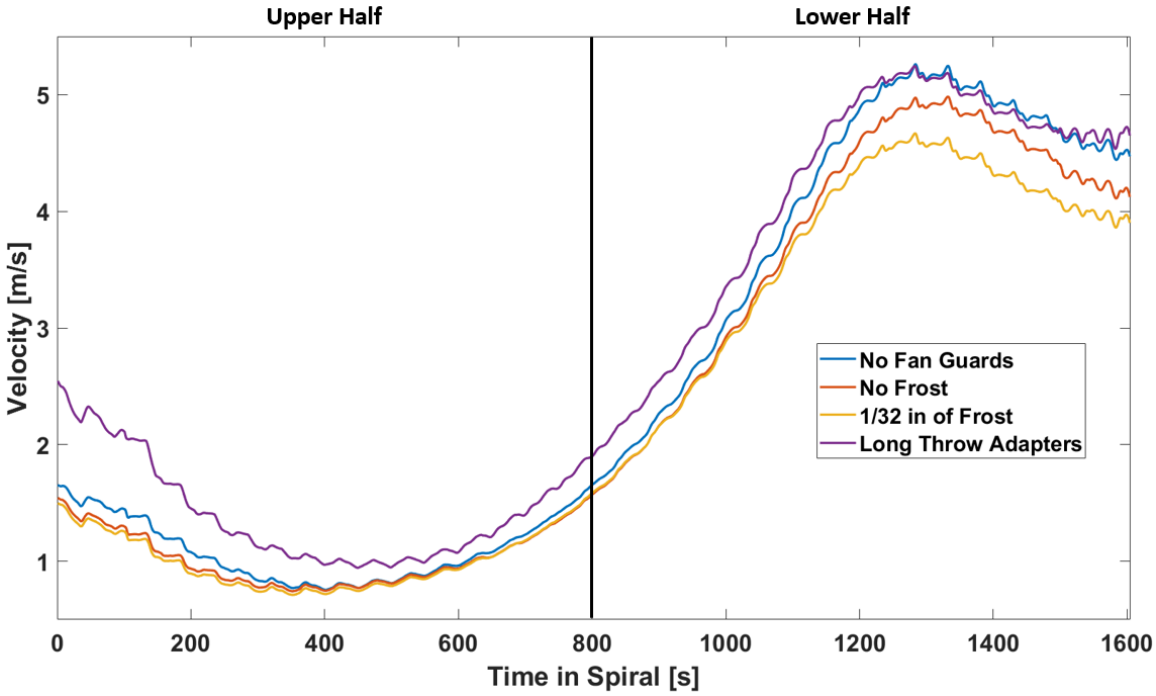

Figure (5.20): Smoothed, (M=200), spiral velocity distributions for Plant 1's base model without fan guards, with unfrosted fan guards, 1/32nd in of first accumulation, and the long throw adapters. Lower and upper halves of spiral labeled.

From Figure (5.19), it can be seen that the LTAs helped redirect the airflow off the ceiling which resulted in a slight increase in spiral velocity at the very top of the spiral as exhibited in Figure (5.20). Both the

frosted and unfrosted fan guards saw a reduction in velocity throughout the spiral. Table (5.9) details the performance metric comparison of the four models.

Table (5.9): Performance metric results of frost accumulation analysis.

Model	Spiral Velocity [m/s] (Δ%)	Coil Face Velocity [m/s] (Δ%)	Product Throughput [prod/min] (Δ%)	Energy per Product [kJ/prod] (Δ%)	Annual Emissions [lb CO_2e/year] (Savings)
Base Model (No guards)	**2.56 (5.8)**	**2.90 (3.9)**	**146.6 (3.2)**	**223.3 (-1.6)**	**3,446,000 (68,000)**
Base Model (No frost)	**2.42 (-)**	**2.79 (-)**	**142.1 (-)**	**227.0 (-)**	**3,514,000 (-)**
Base Model (1/32" frost)	**2.31 (-4.5)**	**2.69 (-3.6)**	**139.0 (-2.2)**	**230.7 (1.6)**	**3,560,000 (-46,000)**
Long Throw Adapters	**2.79 (15.3)**	**2.80 (0.4)**	**155.1 (9.1)**	**215.5 (-5.1)**	**3,326,000 (188,000)**

The findings reveal that a moderate degree of frost accumulation can cause a noteworthy decline in performance, and the degradative effects are compounded as the frost accumulation increases. More importantly, the simulation results demonstrate the effectiveness in implementing LTAs which led to a 15% increase in spiral velocity when compared to the base model with unfrosted fan guards. The addition of LTAs are projected to enhance the throughput capacity by up to 9%, resulting in a significant reduction of almost 190,000 lb of electricity-related CO_2 emissions.

5.3 Plant 2

5.3.1 Base Model

The spiral blast freezer in Plant 2 has a two-pass air flow configuration, with the first pass of air flow traversing the top half of the spiral where it makes a 180 degree turn to make a second pass through the bottom half of the spiral before returning to the inlet of the evaporator coils. The Plant 2 blast freezer is equipped with five centrifugal plug fans that pull air through the evaporator coils and

discharge the air into a “plenum” space to build static pressure to supply air to spiral’s first pass. The product infeed is located at the base of the freezer opposite the evaporators and fans. After infeed, the product travels up the spiral during the freezing process before exiting an outfeed located at the top of the spiral above the fans. The freezer has a solid walkway that serves as septum to split the height of the freezer while also providing a means for personnel to access the upper portion of the spiral and the discharge side of the evaporator coils. The walkway has a rectangular opening on the far side (opposite the evaporator coils & fans) for air to pass from the upper to the lower level. The 3D model used for CFD simulations of the Plant 2 spiral freezer is displayed in Figure (5.21).

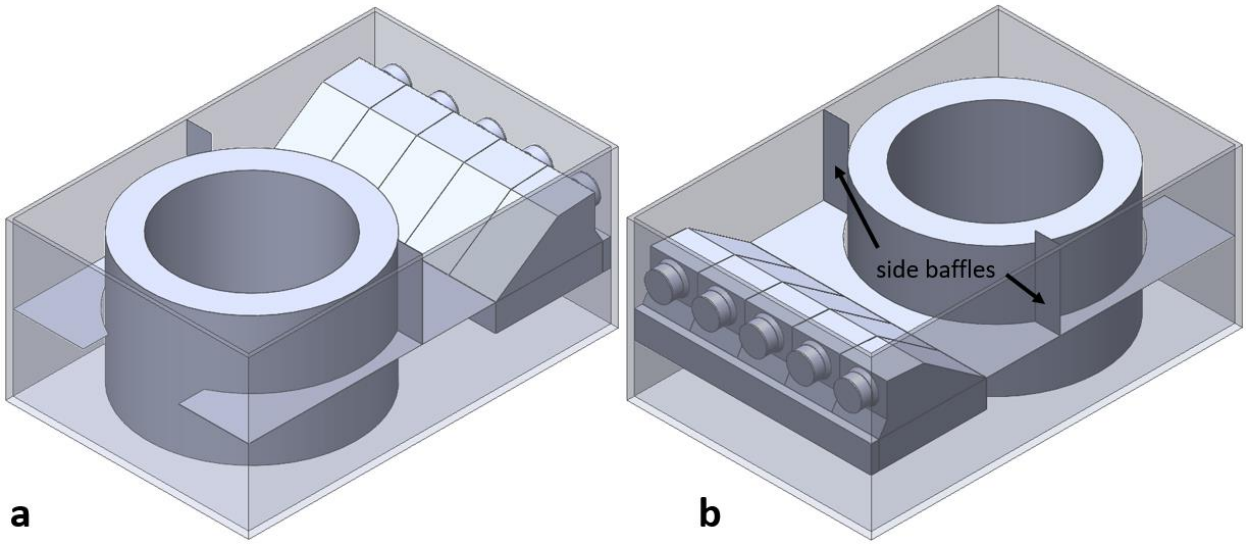

Figure (5.21): 3D model of Plant 2's spiral blast freezer back-side view (a) and front-side view (b).

From the figure, one can see that there are minimal baffling elements, only the two side baffles that attempt to prevent flow bypass on the perimeter of the spiral. There are no baffling elements on the interior of the spiral and therefore flow is unrestricted between the lower and upper levels.

The Plant 2 blast freezer processes a variety of fully cooked unpackaged poultry product that can range slightly in size and weight which enter the spiral immediately after the cooking process. The corresponding table provides details of the average entering and desired exiting temperatures, internal

energy that needs to be extracted from the product to achieve process freezing requirements and the current product throughput capacity for the spiral.

Table (5.10): Average product and throughput information for Plant 2.

Food Product	Start Temp. [K]	End Temp. [K]	Internal Energy to Cool [J/kg]	Current Throughput [kg/hr]
Poultry	**363**	**254**	**635,269**	**3,704.6**

The porous media resistances found in **Appendix A** in Table (A.2) through Table (A.4) for Plant 2, along with the fan curve coefficients found in Table (A.5), and the fluid properties in Table (A.1), the CFD simulation for Plant 2's base configuration was solved. The resulting velocity streamlines were then generated using Ansys® 's post-processing software and are presented in Figure (5.22). The spiral velocity distribution for this simulation is also displayed in Figure (5.23) for further analysis.

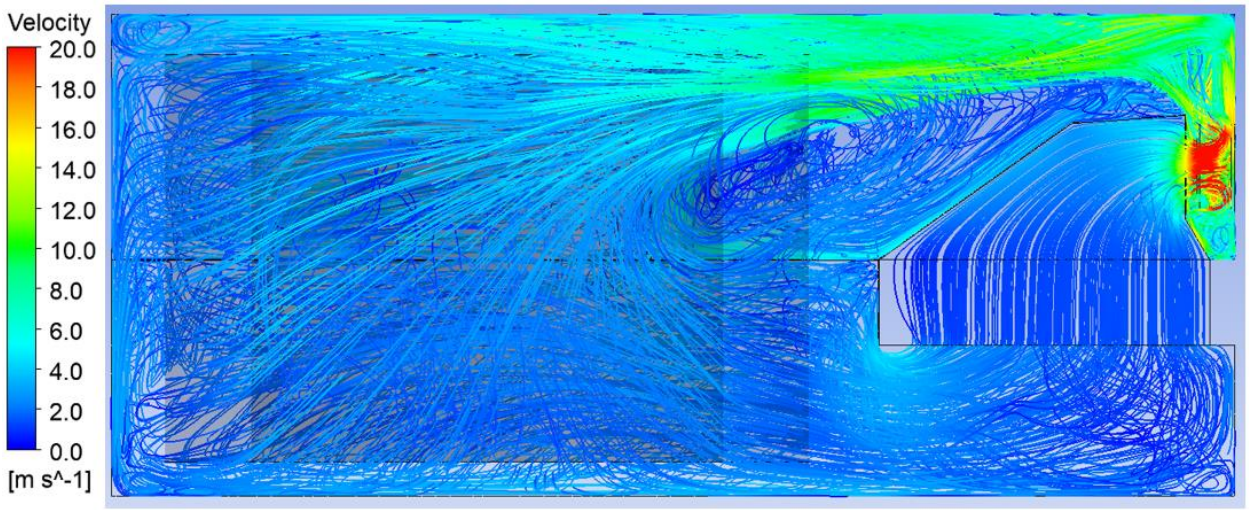

Figure (5.22): Velocity streamlines for Plant 2's base model.

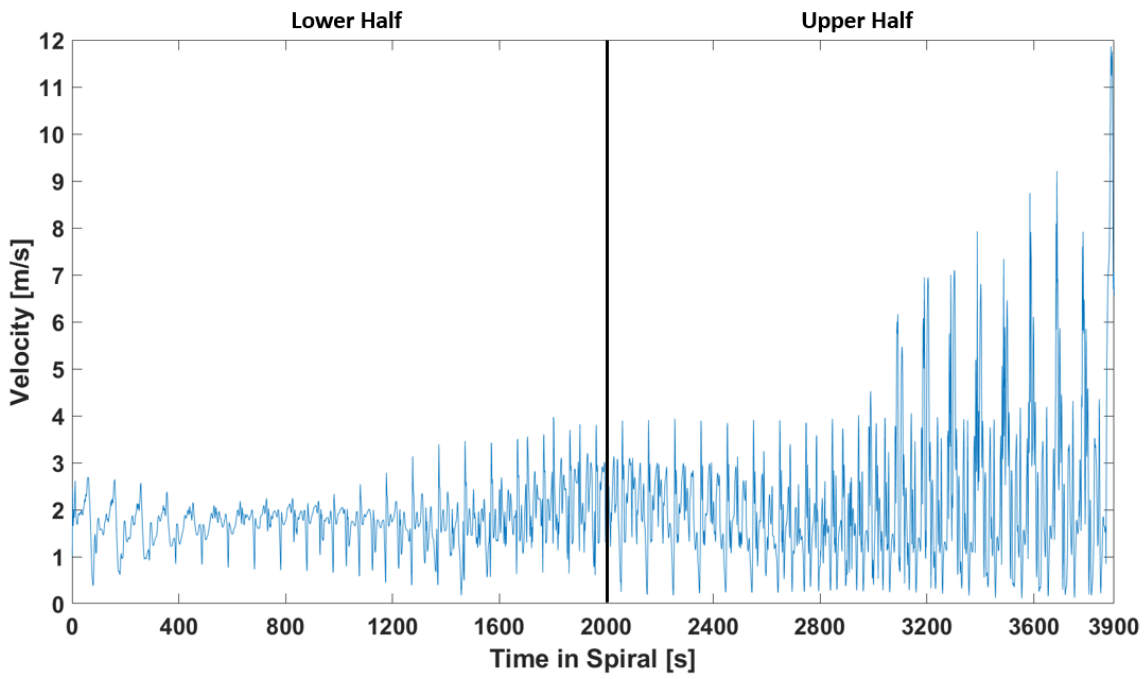

Figure (5.23): Spiral velocity distribution inside Plant 2's base model down-runner, lower and upper halves of spiral labeled.

Based on the CFD results presented, it is evident that the velocity distribution across the product within the spiral exhibits minimal variation throughout the first 3,000 s, beyond this mark there is about twice as much velocity. The sharp spike in velocity in the last 50 s is attributed to the product outfeed being located in close proximity to the discharge of the plug fans. Table (5.11) summarizes the performance metrics resulting from the simulation, the transient product model, and the energy balance program.

Table (5.11): Summary of performance metrics for Plant 2's base model.

Spiral Velocity [m/s]	Coil Face Velocity [m/s]	Product Throughput [kg/hr]	Energy per Mass [kJ/kg]	Annual Emissions [lb CO_2e/year]
1.94	**1.54**	**3,704.6**	**779.1**	**7,661,000**

5.3.2 Design Modifications

Upon examination of Plant 2's base model CFD results, two areas emerged as having the potential for performance improvement in the air-side of the freezing system. The first was to reduce

the air flow bypassing through the interior of the spiral and air flow beneath the spiral. The second was to enhance the inadequate airflow in the portion of the spiral that was opposite the fans, as well as the lower half of the spiral where product enters. Additionally, the insights gained from the design study of the blast freezer used in Plant 1 further guided proposed modifications for Plant 2. Accordingly, three distinct designs were developed, as illustrated in Figure (5.24) and Figure (5.25).

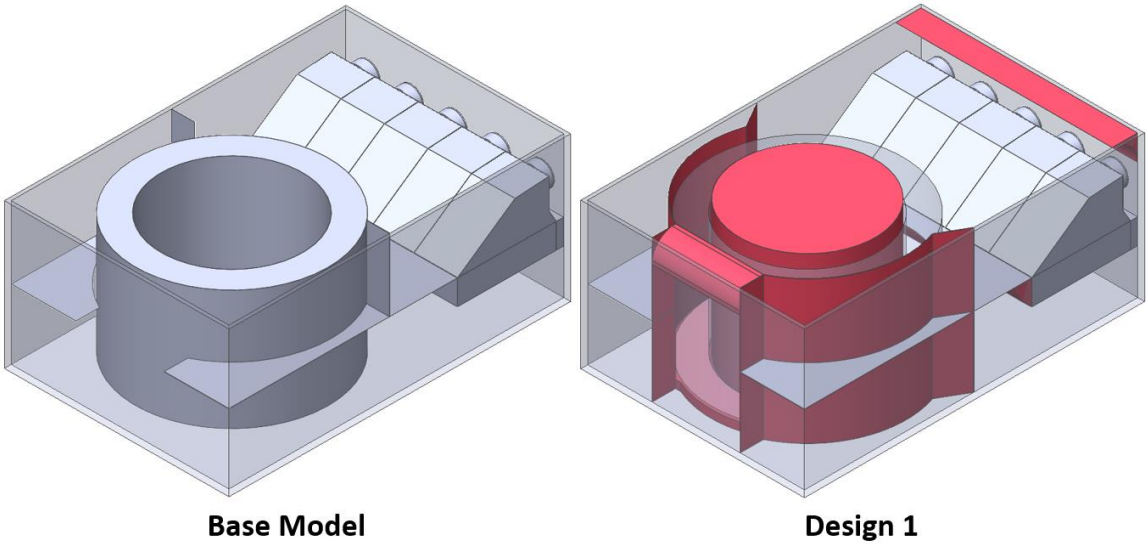

Figure (5.24): Design 1 compared against base model for the design modification analysis conducted on Plant 2, added baffles identified in red.

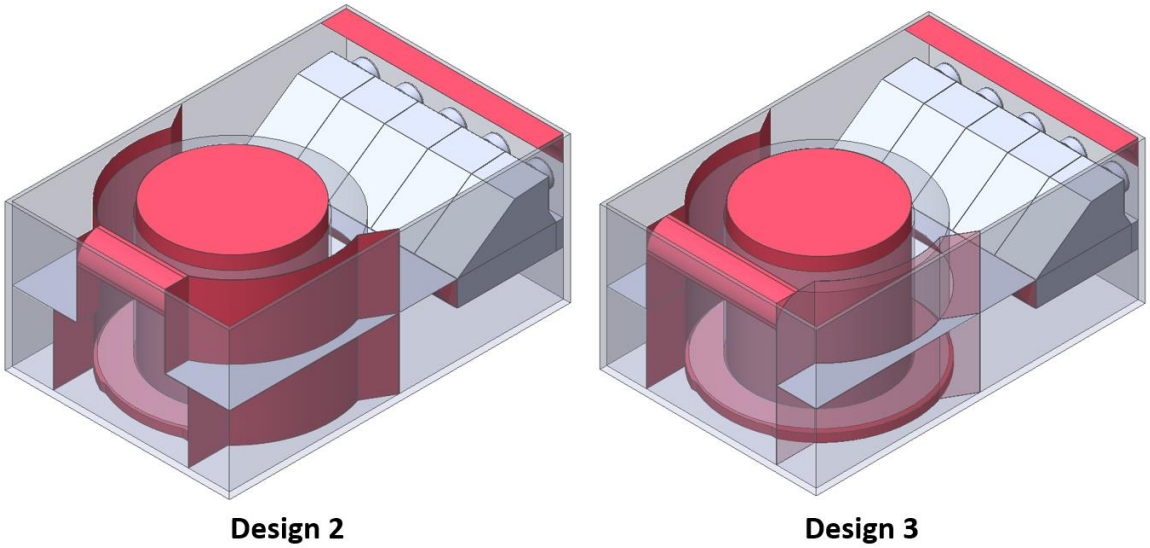

Figure (5.25): Designs 2 and 3 for the design modification analysis conducted on Plant 2, added baffles identified in red.

All three of the proposed designs utilize aspects of the Plant 1 design study, including the placement of a solid “drum” baffle inside the spiral, the installation of a baffle below the spiral to impede bypass, the use of curved baffles to ease the existing 90-degree interior corners, and the application of curved baffles outside the spiral to eliminate empty regions susceptible to local air recirculation. Unfortunately, the constricted space between the spiral and the rear wall prevented the implementation of angled wall baffles that proved effective in Plant 1. Designs 1 through 3, closely resemble each other in their effort to channel the flow towards the walkway opening, thus providing higher air velocity across the entering product. The designs, however, progress incrementally towards greater openness, with Design 2 presenting a larger opening in the lower half, and Design 3 featuring a larger opening in both halves. Design 3 would, however, necessitate a minor adjustment to the walkway opening.

The three designs were simulated in Ansys® Fluent under the same parameters as the base model, and their velocity streamlines and spiral velocity distributions are showcased in Figure (5.26) through Figure (5.28).

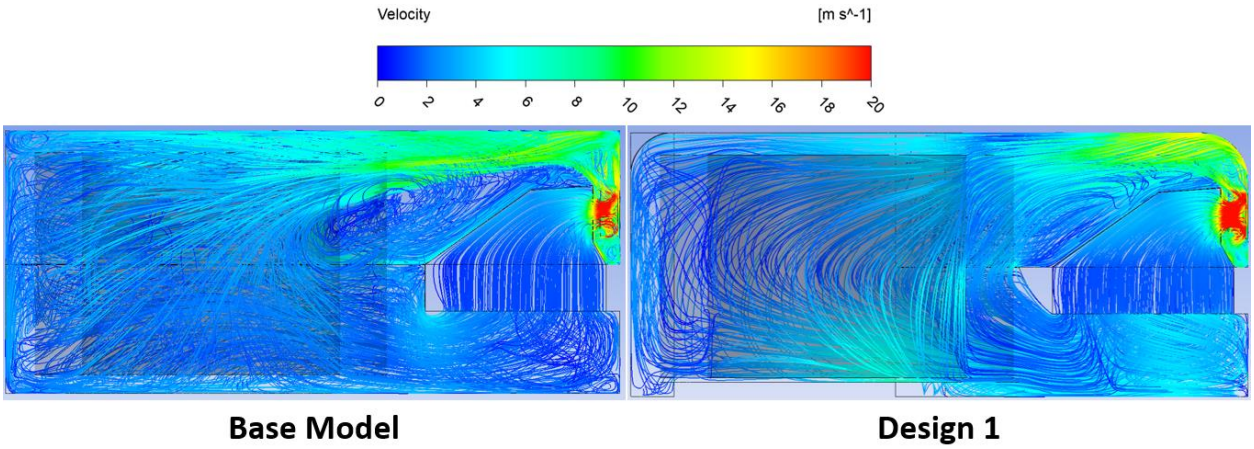

Figure (5.26): Velocity streamlines for Design 1, compared against the Plant 2’s base model.

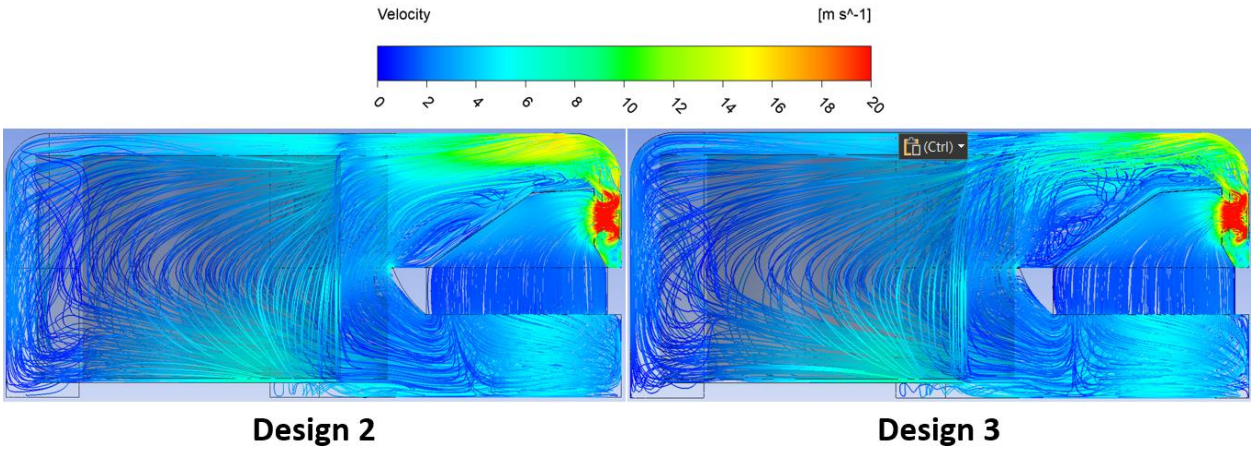

Figure (5.27): Velocity streamlines for designs 2 and 3.

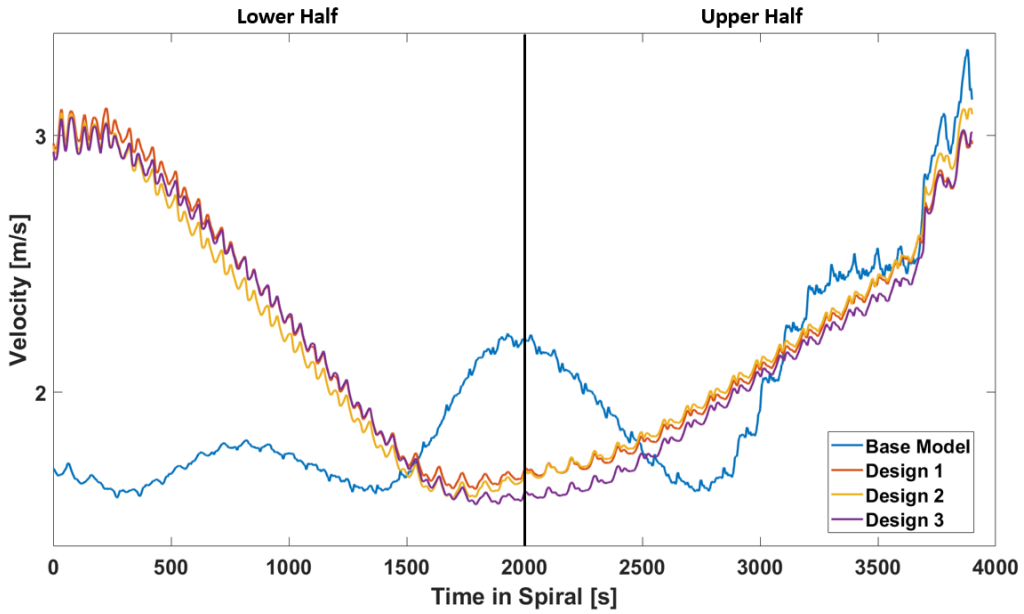

Figure (5.28): Smoothed, (M=400), spiral velocity distributions for designs 1 through 3 compared against the base model, for Plant 2. Lower and upper halves of spiral labeled.

The figures clearly demonstrate that all three designs achieved significant improvements of air velocity over the product entering the spiral, which is crucial to quickly decreasing the temperature of the entering cooked product. Upon examining the streamline results, it appears that a significant portion of the airflow bypasses through the center of the spiral. However, this observation is somewhat misleading

since what is primarily observed is the airflow inside the narrow clearance between the spiral and the central baffle and not the airflow inside the spiral itself, as demonstrated by a plan-view in Figure (5.29).

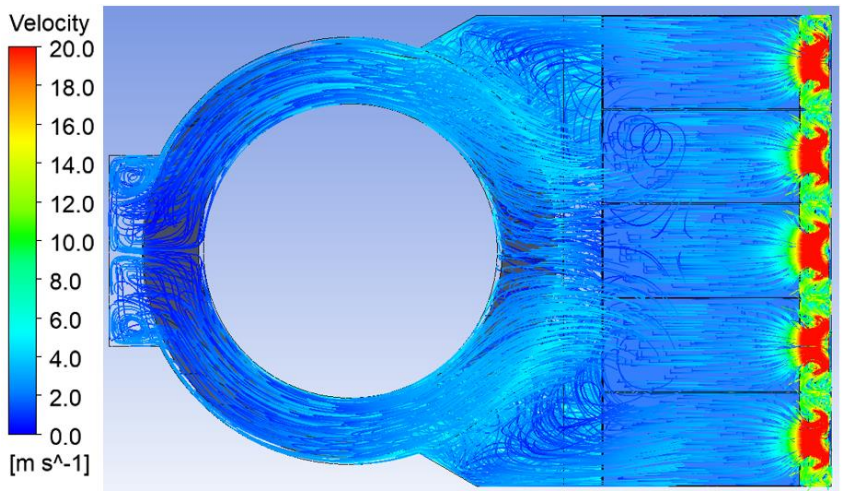

Figure (5.29): Plan-view of Design 1, demonstrating that no flow is entering center of spiral.

Nevertheless, there is still a considerable amount of airflow that fails to reach the back passage on the wall opposite the fans due to the spiral's relatively high air resistance between the successive levels of the spiral belt. This is attributed to the height of the product, which leaves little clearance between the spiral levels. Table (5.12) summarizes and compares the performance metrics of the proposed modifications against the base model for the Plant 2 blast freezing system.

Table (5.12): Performance metric results from design modification analysis for Plant 2.

Model	Spiral Velocity [m/s] (Δ%)	Coil Face Velocity [m/s] (Δ%)	Product Throughput [kg/hr] (Δ%)	Energy per Mass [kJ/kg] (Δ%)	Annual Emissions [lb CO_2e/year] (Savings)
Base Model	**1.94 (-)**	**1.54 (-)**	**3,704.6 (-)**	**779.1 (-)**	**7,661,000 (-)**
Design 1	**2.22 (14.4)**	**1.54 (0.0)**	**3,929.9 (6.2)**	**759.1 (-2.6)**	**7,463,000 (198,000)**
Design 2	**2.20 (13.5)**	**1.54 (0.0)**	**3,910.9 (5.5)**	**760.8 (-2.4)**	**7,481,000 (180,000)**
Design 3	**2.18 (12.5)**	**1.54 (0.0)**	**3,900.0 (5.3)**	**761.7 (-2.2)**	**7,489,000 (172,000)**

The table reveals that the three designs resulted in only marginal improvement in average spiral velocity, particularly when compared to the more significant performance improvements projected by

the CFD analysis of Plant 1's proposed air-side modifications. Interestingly, as the designs became increasingly open, the average air velocity within the spiral decreased. This outcome was unexpected since one might presume that a less restrictive design would enhance airflow. One possible explanation is that the concentrated design of Plant 2's Design 1 actually accelerated the airflow through the back passage, resulting in a slightly higher observed velocity. Even so, the airflow improvements achieved by the designs could potentially increase throughput by 5-6%, leading to a minor reduction in per-product energy consumption and nearly 200,000 lb reduction in CO_2e emissions.

5.4 Plant 3

5.4.1 Base Model

Plant 3's freezing system consists of two identical spiral freezers arranged side-by-side in series. Product enters an "up-runner" low and internally transitions to a "down-runner" at the top and exits low to a packaging area. Both up- and down-runners utilize a three tier two-pass air flow arrangement, with the air passing through the top two-thirds of the spiral first before being directed back through the bottom third of the spiral to the inlet of the evaporator coils. Each spiral freezer is equipped with eight axial fans in a stacked arrangement. The fans pull air through their respective evaporator coils and separately discharge air to the top two-thirds of the spiral. The tiers of the freezer are split up with solid walkway on the fan side and a square perforated walkway on the opposing side. As both freezers are identical, one 3D model was used for CFD simulations and is displayed in Figure (5.30).

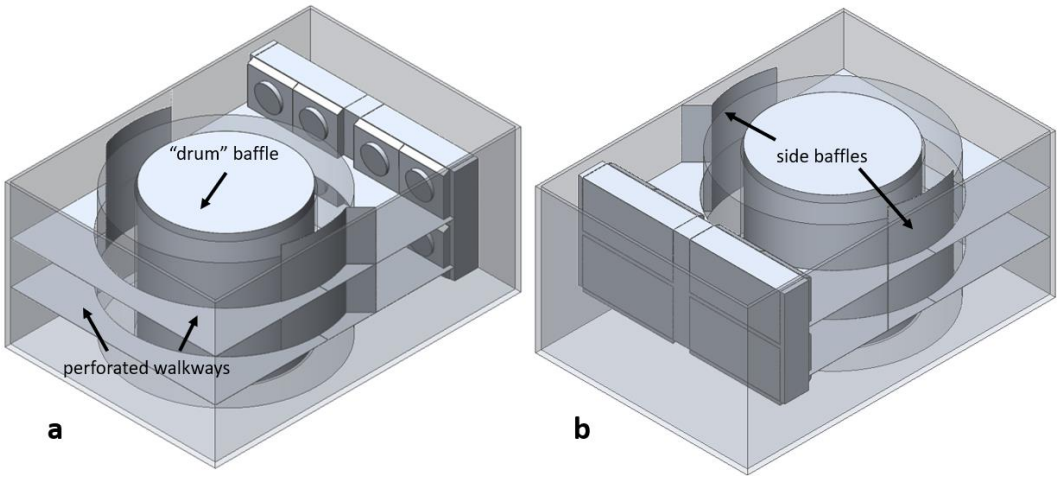

Figure (5.30): 3D model of Plant 3's spiral blast freezer front-side view (a) and back-side view (b).

The double spiral freezing systems in Plant 3 have, seemingly, been designed with more consideration of airside performance than the previously studied freezers. The Plant 3 spiral freezers feature a solid center "drum" baffle to prevent air bypass through the center of the spiral as well as strategically positioned baffles on the upper two tiers to prevent bypass around the spiral, both of which were identified from the design study of Plant 1 to improve airflow performance.

Somewhat similar to Plant 1, the specific blast freezer in Plant 3 processes a partially baked dough product and is topped with additional ingredients. Table (5.13) provides details on the entering and desired exiting temperatures, internal energy required to freeze the product, and the current throughput capacity.

Table (5.13): Product and throughput information for Plant 3.

Food Product	Start Temp. [K]	End Temp. [K]	Internal Energy to Cool [J/prod] (J/kg)	Current Throughput
Dough	**305**	**261**	**197,372 (278,038)**	**150.0 [prod/min]**

The CFD simulation for Plant 3's base case configuration was solved with the porous media resistances found in **Appendix A** defined in Table (A.2) through Table (A.4) for Plant 3, along with the fan curve coefficients presented in Table (A.5), and the fluid properties in Table (A.1). The resulting velocity

streamlines were produced with Ansys® 's post-processing software and are shown in Figure (5.31). The spiral velocity distribution for the down-runner is also displayed in Figure (5.32) for further analysis.

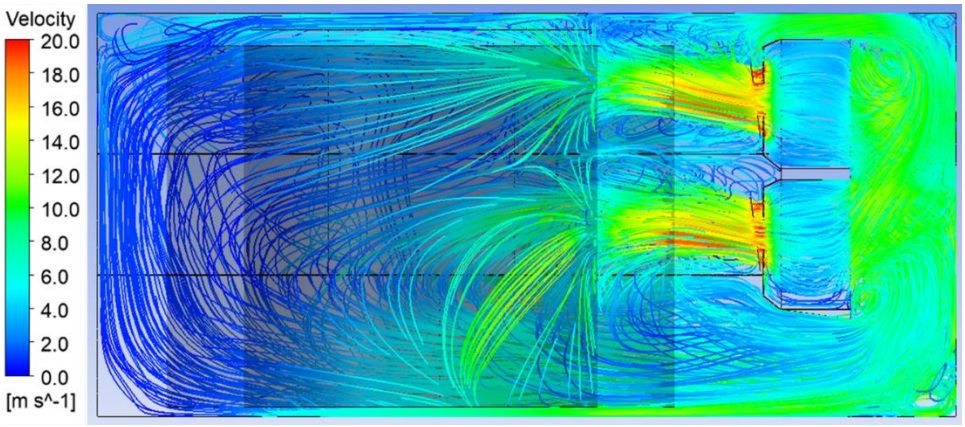

Figure (5.31): Velocity streamlines for Plant 3's base model.

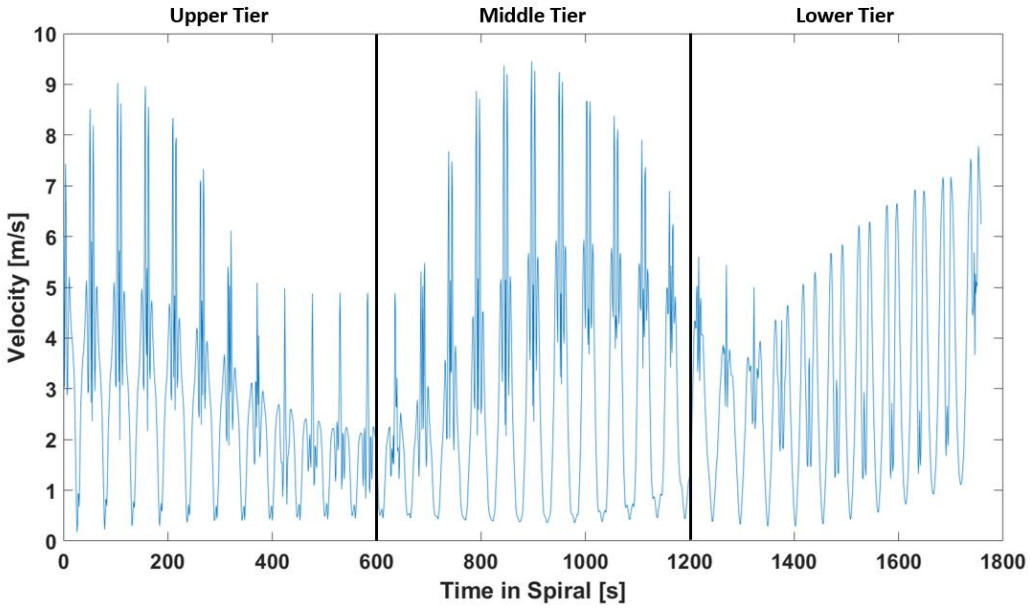

Figure (5.32): Spiral velocity distribution inside Plant 3's base model down-runner, lower, middle, and upper tiers of spiral labeled.

The analysis of the streamlines and velocity distribution demonstrates that the design of Plant 3's airflow system is characterized by relatively favorable performance. The distribution displays two prominent peaks of high velocity at the levels coincident with air leaving the evaporator fans and a third peak located towards the bottom of the spiral on the air return side. Notably, it is worth mentioning that

the air velocity distribution for the up-runner would be a mirror image of Figure (5.32), with the lower tier coinciding with the first 600 sec following the product initially entering the freezing system. Thus, the entering product experiences lower relative airflow as it is situated within the up-runner. Again there seems to be air flow bypassing through the center of the spiral, which is actually air that is flowing through an opening between the center drum baffle and the interior of the spiral belt. The shallow troughs of the air velocity oscillations indicate that little airflow is reaching the segment of the spiral opposite the fans. A summary of the simulation results, product model, and energy balance program can be found in Table (5.14).

Table (5.14): Summary of performance metrics for Plant 3's base model.

Spiral Velocity [m/s]	Coil Face Velocity [m/s]	Product Throughput [prod/min]	Energy per Product [kJ/prod]	Annual Emissions [lb CO_2e/year]
2.86	**3.94**	**150.0**	**229.9**	**5,491,000**

5.4.2 Design Modifications

After inspection of Plant 3's base model CFD results, three distinct areas were identified as candidates for potential improvements. Firstly, one goal was to prevent air flow from bypassing over the top of the spiral cage as well as an open gap above the upper coils. The latter issue was causing a portion of the flow off the fans to be immediately recirculated back into the evaporators. The second area of improvement involved increasing the velocity of air over the product on the side opposite the fans. Finally, there was a need to mitigate the recirculation occurring near the fan discharge, as well as the region behind the coils. To address these areas of improvement, two innovative designs were developed and are depicted in Figure (5.33).

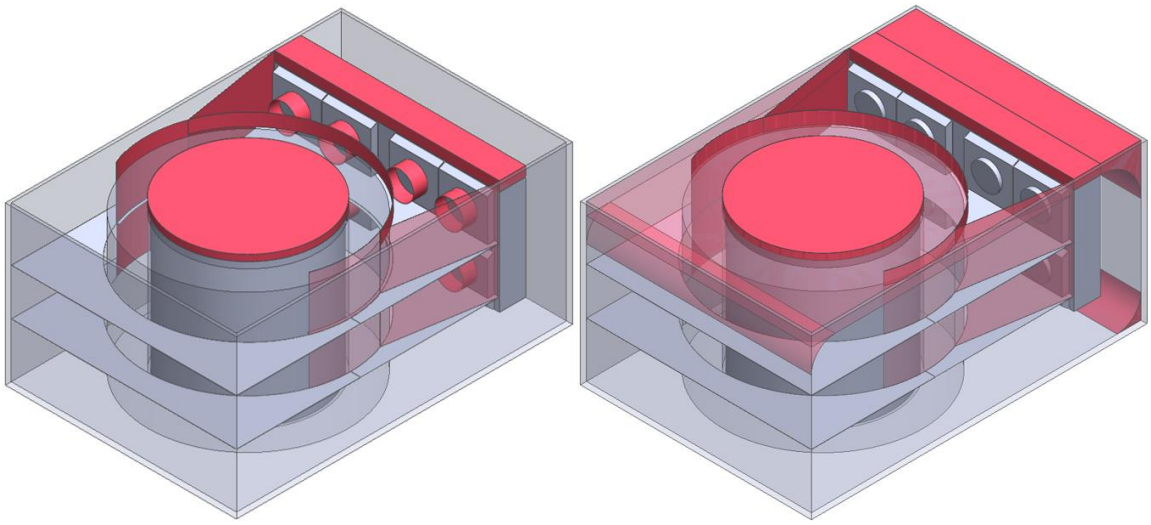

Figure (5.33): Designs 1 and 2 for the design modification analysis conducted on Plant 3, added baffles identified in red.

To mitigate air bypass, both designs incorporate a solid baffle that extends from the center to the ceiling, as well as a baffle over the coils. Moreover, both designs feature a semi-circular baffle above the perimeter of the spiral. The baffle for Design 1 is a thin strip whereas baffle for Design 2 is "filled in," effectively, lowering the ceiling height of the Plant 3 spiral freezer. Additionally, no baffle was placed beneath the spiral since it was determined that the bypass was minimal due to the tight physical clearance between the freezer floor and the bottom of the spiral. To enhance the airflow to the back portion of the spiral, long angled baffles were placed on the sides of the freezer, effectively channeling the flow across the spiral belt. These baffles were also designed to minimize the empty space in front of the fans, thus reducing local recirculation. To further reduce air recirculation, Design 1 utilized short throw adapters (STAs) on the exhaust of the fans, while Design 2 incorporated curved baffling pieces located behind the coils. The former was expected to better concentrate the flow coming off the fans, preventing spillage into the adjacent region.

The two designs were simulated in Ansys® Fluent using the base model's parameters, and their velocity streamlines and spiral velocity distributions are displayed in Figure (5.34) and Figure (5.35)

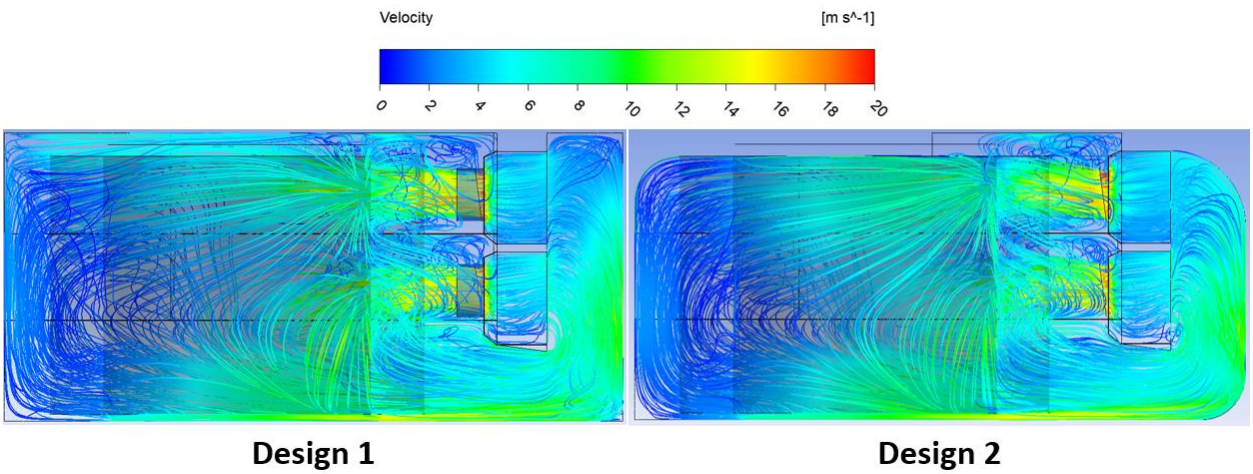

Figure (5.34): Velocity streamlines for Designs 1 and 2.

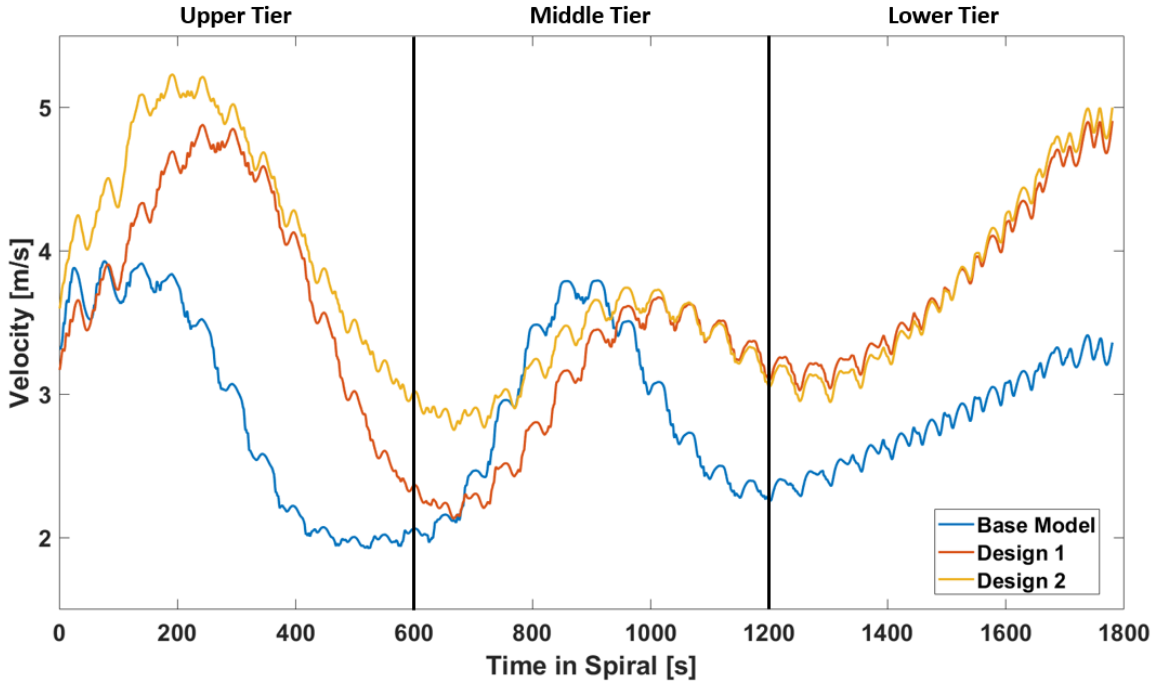

Figure (5.35): Smoothed, (M=200), down-runner spiral velocity distributions for Designs 1 and 2 compared against the base model, for Plant 3. Lower, middle, and upper tiers of spiral labeled.

Analysis of the streamlines reveal that Design 1's thin semi-circle baffle was less effective in curbing airflow bypass over the spiral, compared to Design 2's solid baffle. This observation is consistent with the results of the design study for Plant 1, where the thin semi-circle baffle, positioned below the spiral, still allowed for air bypass. Air will follow the path of least resistance, flowing through the belt before passing over the spiral. As such, Design 2's solid baffle is the only effective way to prevent air bypass, as

it provides no room for the air to travel through the belt. Moreover, the placement of the baffle above the coils, in both designs, proved to be successful in preventing recirculation off of the fans.

Both designs facilitated better flow on the back side of the spiral, as evidenced by the streamlines. Additionally, there was a significant improvement in airflow to the lower tier of the spiral, as depicted by the velocity distribution. While the use of extensions to direct discharge air off the fans did not yield significant benefits in reducing air recirculation, the curved baffles were helpful in limiting recirculation behind the coils and against the back wall. The effectiveness of the designs is detailed in Table (5.15), providing a performance metric comparison.

Table (5.15): Performance metric results from design modification analysis for Plant 3.

Model	Spiral Velocity [m/s] (Δ%)	Coil Face Velocity [m/s] (Δ%)	Product Throughput [prod/min] (Δ%)	Energy per Product [kJ/prod] (Δ%)	Annual Emissions [lb CO_2e/year] (Savings)
Base Model	**2.86 (-)**	**3.94 (-)**	**150.0 (-)**	**229.9 (-)**	**5,491,000 (-)**
Base Model (Optimal)	**2.86 (-)**	**3.94 (-)**	**211.0 (40.64)**	**198.6 (13.61)**	**4,743,000 (747,000)**
Design 1	**3.56 (24.5)**	**3.54 (-10.2)**	**243.7 (62.48)**	**188.5 (18.01)**	**4,502,000 (989,000)**
Design 2	**3.78 (32.2)**	**3.57 (-9.4)**	**255.3 (70.23)**	**185.3 (19.40)**	**4,425,000 (1,066,000)**

Plant 3's unique employment of both up-runner and down-runner components entails that the product will encounter both the velocity distribution in Figure (5.35) and its mirror image. Analysis of the base model distribution with the transient product model revealed that the current dwell time of 3,560 sec is excessively long and results in the product exiting the down-runner at temperatures below the desired range of 261 K.

Therefore, to achieve the desired product exit temperature, the optimal product throughput rate was determined, and added to Table (5.14), resulting in a remarkable 41% improvement. The table indicates that both designs yielded an approximately 30% increase in spiral velocity, with Design 2

having a slight advantage. Despite a reduction in average coil face velocity for both designs, the impact on coil capacity is anticipated to be minimal and does not warrant concern.

The increased air velocity within the spiral enhances freezing performance, enabling the system to process 60-70% more product while consuming 19% less energy per product. With the increase in efficiency, the freezer has a potential 1 million lb reduction in CO_2e emissions!

5.5 Plant 4

5.5.1 Base Model

The spiral blast freezer in Plant 4 is another two-pass configuration, wherein the supply air passes through the top half of the spiral and then directed back through the bottom half before returning to the evaporator coils. Similar to the fans used in Plant 2, the Plant 4 freezer is fitted with six centrifugal plug fans that push air, instead of pulling, through the evaporator coils. The infeed of product is located at the base of the freezer and moves up the spiral during the freezing process before exiting the outfeed at the top of the spiral. To provide access to the upper section of the spiral, the freezer has a solid walkway that splits the height of the freezer. The walkway includes a large rectangular opening on the far side for air to flow through to the lower level. The 3D model used for CFD simulations is displayed Figure (5.36).

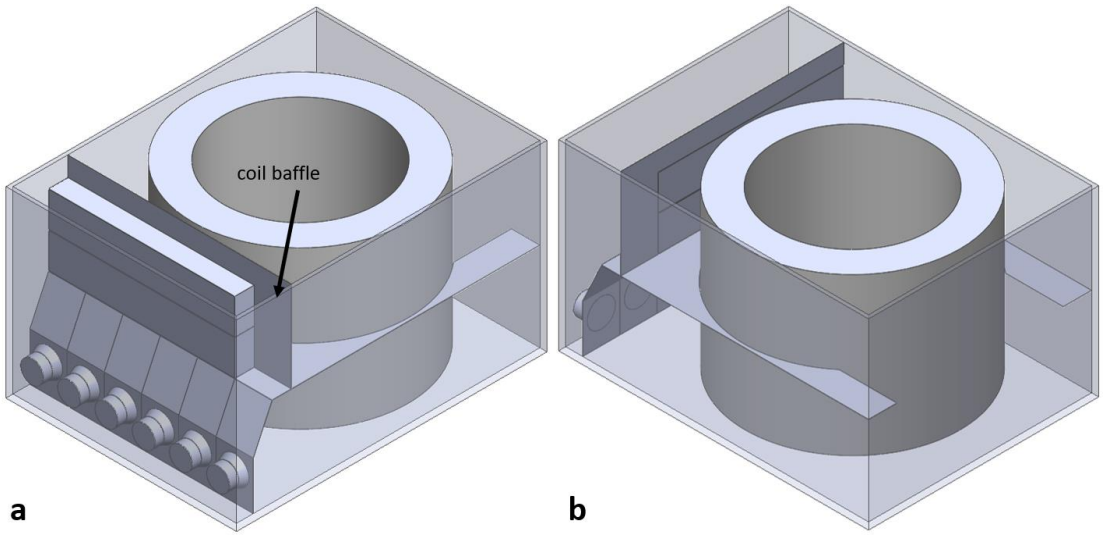

Figure (5.36): 3D model of Plant 4's spiral blast freezer front-side view (a) and back-side view (b).

From the figure, one can see that there are no baffling elements, aside from the baffle over the evaporator coils. Flow between the upper and lower portion is unrestricted through the center of the spiral.

This specific blast freezer within Plant 4 processes raw cut-up poultry that is packaged and plastic-sealed with a goal of achieving a "crust freeze" but not fully frozen. The corresponding table provides details of the average entering and desired exiting temperatures, internal energy that needs to be extracted from the product to achieve the temperature difference, and the current product throughput capacity.

Table (5.16): Product and throughput information for Plant 4.

Food Product	Start Temp. [K]	End Temp. [K]	Internal Energy to Cool [J/kg]	Current Throughput [kg/hr]
Poultry	**280**	**270**	**293,110**	**5,897.6**

As highlighted by the table, the poultry products undergo a relatively small temperature change.

Utilizing the porous media resistances found in **Appendix A** in Table (A.2) through Table (A.4) for Plant 4, alongside the fan curve coefficients available in Table (A.5), and the fluid properties in Table

(A.1), the CFD simulation for Plant 4's base model was successfully solved. Thereafter, velocity streamlines were created, and the results are presented in Figure (5.37). Furthermore, Figure (5.38) presents the spiral velocity distribution attained from this simulation.

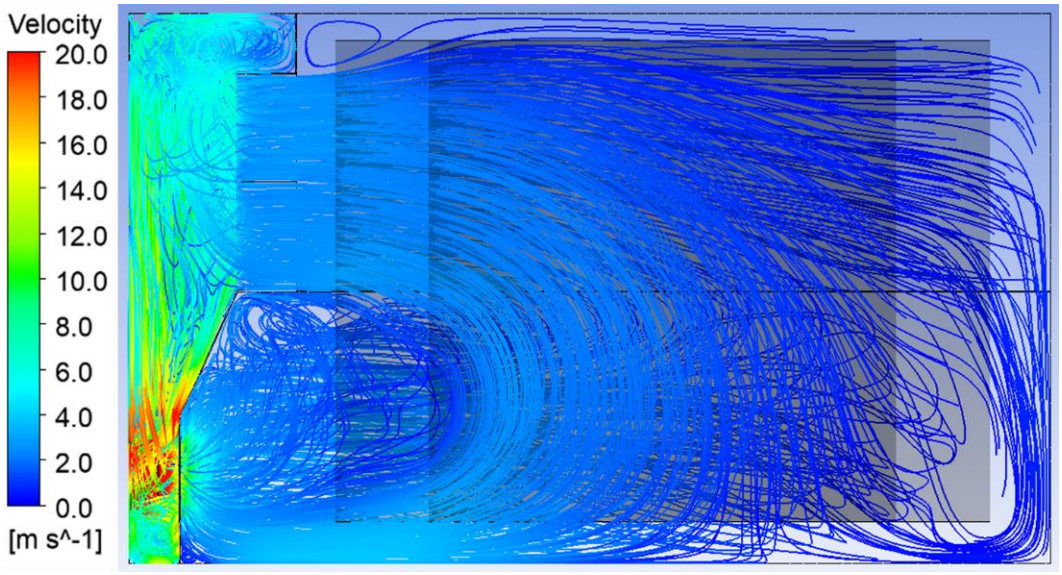

Figure (5.37): Velocity streamlines for Plant 4's base model.

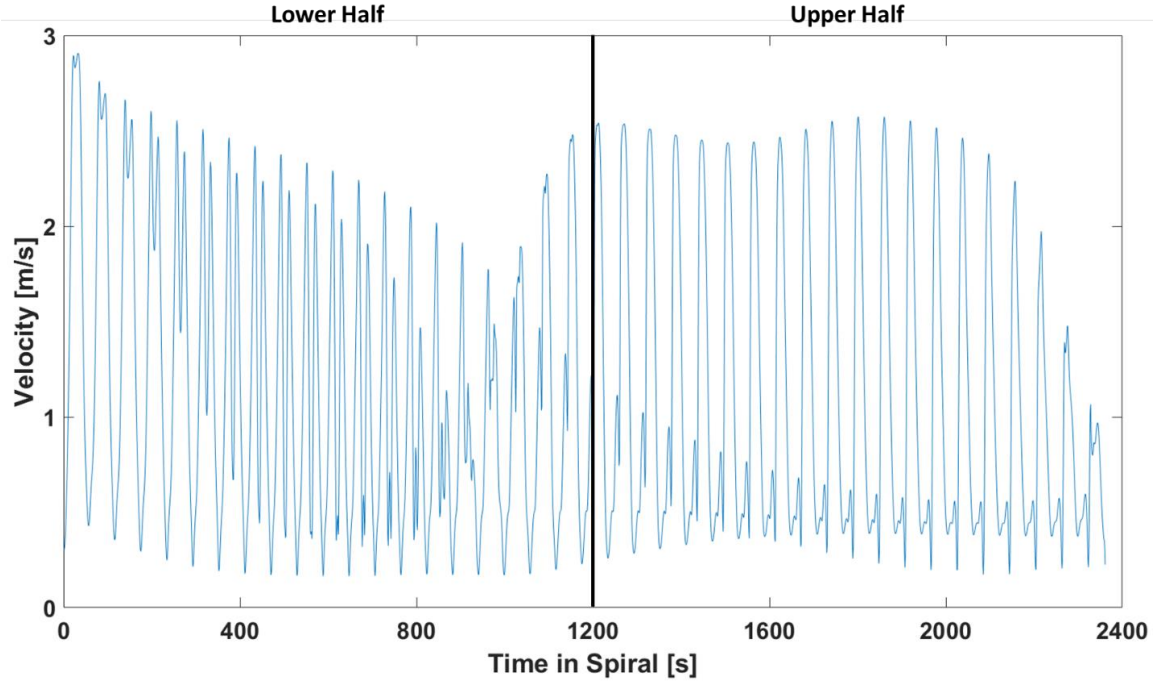

Figure (5.38): Spiral velocity distribution inside Plant 4's base model. Lower and upper halves of spiral labeled.

The figures indicate that the air velocity distribution along the entire length of the spiral remains relatively consistent, except for a minor decrease below the walkway. The streamlines reveal that the air experiences challenges when it turns 90 degrees through the evaporator coils. Moreover, a significant proportion of the air flow bypasses the spiral through both the core and between the bottom of the spiral belt and freezer floor. Finally, the oscillatory low points in the velocity distribution suggest that the section of the spiral opposite the fans receives little airflow. A summary of the simulation results, product model, and energy balance program can be found in Table (5.17).

Table (5.17): Summary of performance metrics for Plant 4's base model.

Spiral Velocity [m/s]	Coil Face Velocity [m/s]	Product Throughput [kg/hr]	Energy per Pound [kJ/kg]	Annual Emissions [lb CO_2e/year]
1.13	**2.80**	**5,897.6**	**426.2**	**4,201,000**

5.5.1 Design Modifications

After further analysis of the CFD results for the base model of Plant 4, three areas were identified as potential for air-side performance improvement. The first pertained to reducing the flow of air that bypassed through the interior of the spiral and between the bottom of the spiral and the freezer floor. The second area for improvement required enhancing the insufficient airflow in the section of the spiral that was opposite the fans. Lastly, there was a need to optimize the airflow through the coils. Three designs, shown in Figure (5.39) and Figure (5.40) were developed for Plant 4's spiral which were guided by the identified improvement areas and design study findings.

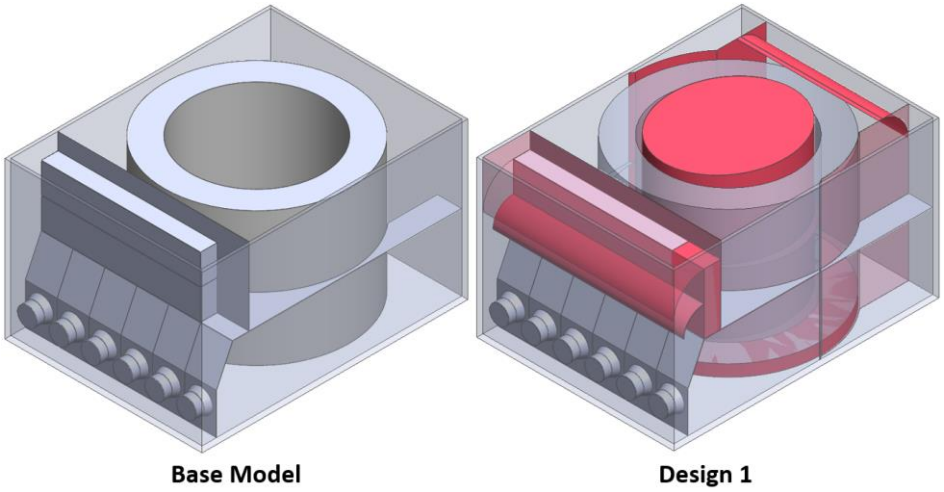

Figure (5.39): Design 1 compared against the base model for the design modification analysis conducted on Plant 4, added baffles identified in red.

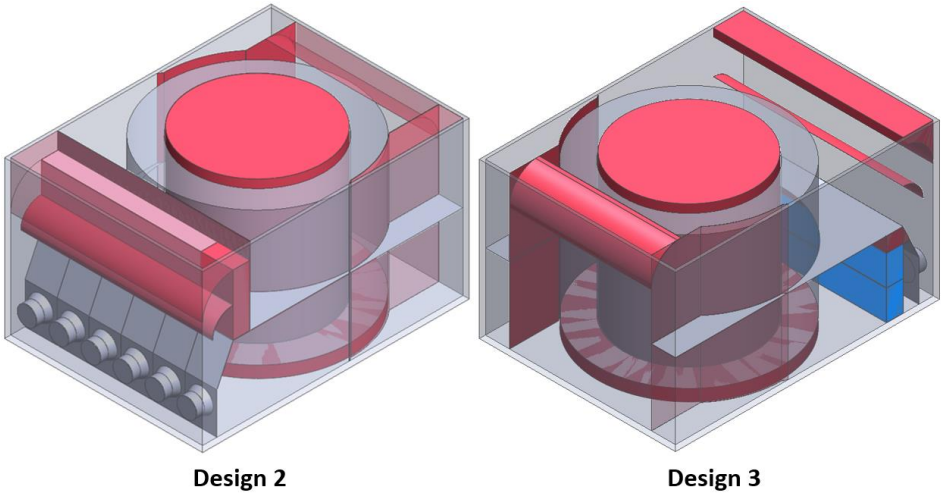

Figure (5.40): Designs 2 and 3 for the design modification analysis conducted on Plant 4, added baffles identified in red, relocated components identified in blue.

In order to address the issue of air flow bypass, solid baffles were incorporated in the interior (drum baffle) and beneath the spiral. Design 1 sought to examine the impact of the shape of the interior baffle, leading to the utilization of an elliptic cylinder. This design was considered to evaluate whether the enhanced airflow of a streamlined baffle would compensate for the potential bypass resulting from the extra clearance of incongruent shapes. A circular fin was placed at the walkway elevation on the elliptic baffle to prevent bypass to the lower level.

To promote greater airflow in the back portion of the spiral, curved baffles were introduced on the sides of the freezer, guiding air into the walkway opening. This method has been shown to be advantageous based on changes made to Plant 2. Additionally, two curved baffles have been placed above the fans in order to direct flow of air into the coils and eliminate the recirculation observed in the upper left corner of Figure (5.37).

In Design 3, the coils were relocated to the lower floor, as it was theorized that a "pull-through" approach would outperform "pushing" the air through. Although this design would be impractical for Plant 3 to adopt, it was intended to provide a better understanding of the benefits and drawbacks of such a configuration. These three designs were simulated in Ansys® Fluent with base model parameters, and their velocity streamlines and spiral velocity distributions are presented in Figure (5.41) through Figure (5.43).

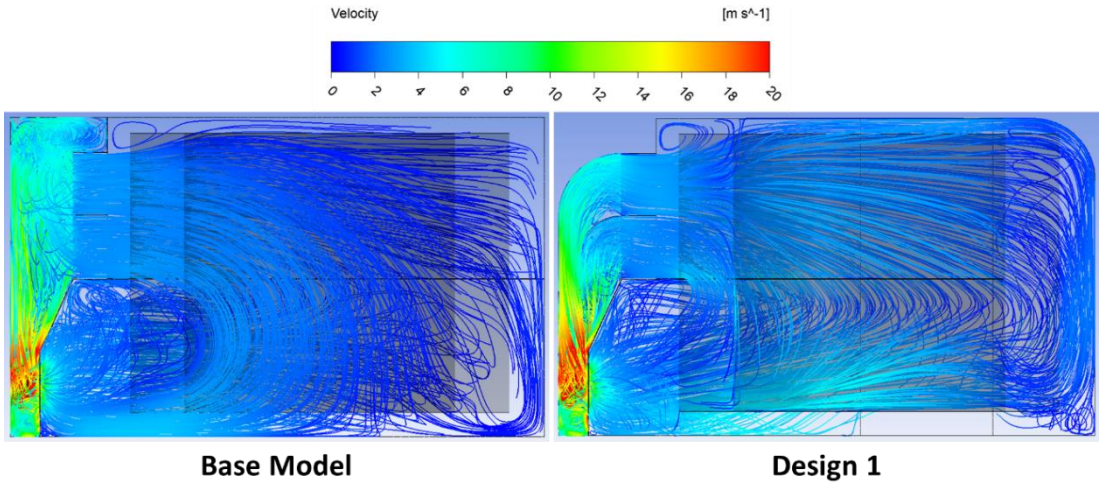

Figure (5.41): Velocity streamlines for Design 1, compared against the base model.

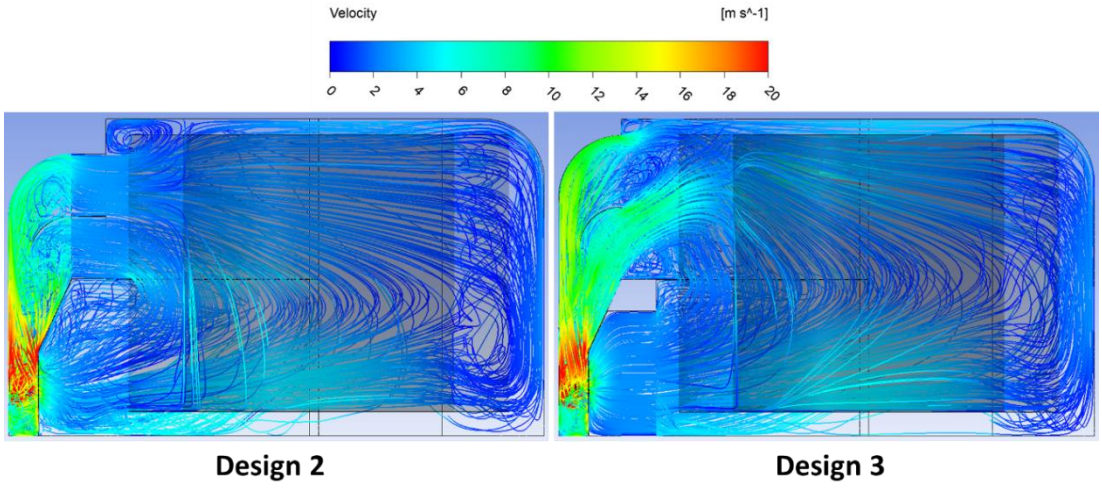

Figure (5.42): Velocity streamlines for designs 2 and 3.

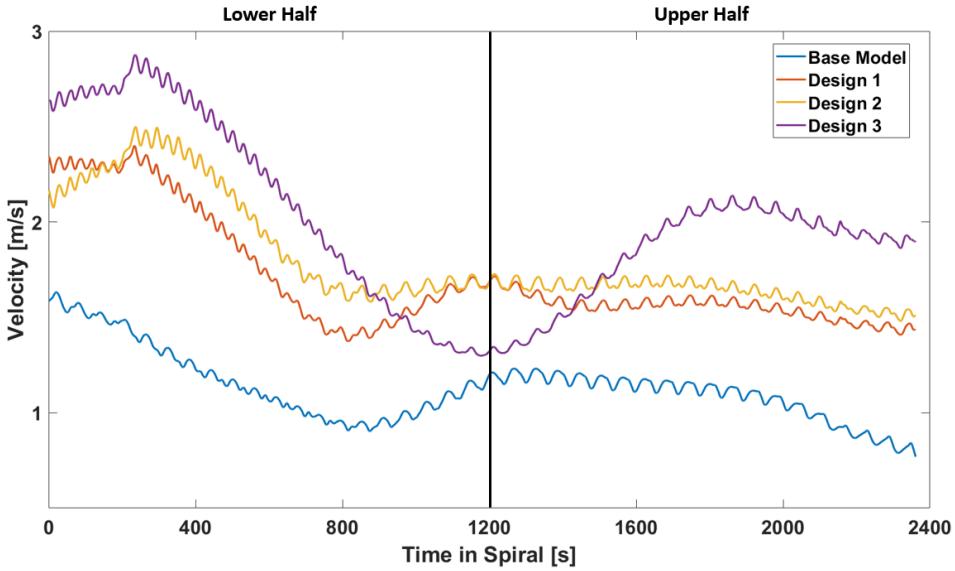

Figure (5.43): Smoothed, (M=400), spiral velocity distributions for designs 1 through 3 compared against the base model, for Plant 4. Lower and upper halves of spiral labeled.

Upon examining the velocity streamlines and spiral velocity distributions, it is evident that each of the three designs exhibited enhanced airflow throughout the entirety of the spiral, particularly during the first and last 800 sec of the freezing process. However, it is noteworthy that the employment of the interior baffle seems to have exacerbated the issue of bypass over the spiral, a problem that was not observed in the base model. This can be attributed to the outgoing flow colliding with the baffle, which results in its upward redirection through the top level of the spiral. This could be remedied by

incorporating a baffle that is positioned above the spiral. The implementation of side baffles has again been proven effective in promoting greater airflow in the rear section of the spiral. In Design 3, it appears that the length of the curved baffles ought to be extended at the trailing edge as the flow through them appeared to experience an upward tendency. Table (5.18) provides a performance metric comparison of the three designs.

Table (5.18): Performance metric results from design modification analysis for Plant 4.

Model	Spiral Velocity [m/s] (Δ%)	Coil Face Velocity [m/s] (Δ%)	Product Throughput [kg/hr] (Δ%)	Energy per Mass [kJ/kg] (Δ%)	Annual Emissions [lb CO_2e/year] (Savings)
Base Model	**1.13 (-)**	**2.80 (-)**	**5,897.6 (-)**	**426.2 (-)**	**4,201,000 (-)**
Design 1	**1.70 (50.4)**	**2.84 (1.4)**	**6,450.1 (9.4)**	**403.9 (-5.2)**	**3,981,000 (220,000)**
Design 2	**1.80 (59.3)**	**2.87 (2.5)**	**6,545.3 (11.0)**	**401.0 (-5.9)**	**3,953,000 (248,000)**
Design 3	**1.99 (76.1)**	**2.74 (-2.1)**	**6,681.4 (13.3)**	**395.5 (-7.1)**	**3,900,000 (301,000)**

The proposed designs demonstrated exceptional performance, exhibiting an increase in average spiral velocity of 50-75%. Interestingly, the utilization of an elliptic cylinder in Design 1 for the interior baffle proved to be inferior compared to the plain cylinder. Further investigation revealed that the elliptic cylinder allowed greater air bypass, resulting in decreased efficiency.

The results showed that the pull-through method in Design 3 outperformed the push-through approach utilized in Design 2. This can be attributed to the added resistance that the coils impose on the airflow, coupled with the sharp change in direction that was necessitated. Pulling the air through the coils, normal to the front face, proved to be the least resistive path. One potential drawback to the pull-through configuration is it leads to a slight increase in the air temperature that the product is exposed to, as air is exiting the fans and not the evaporator, thus absorbing heat. As such, a 2°F increase in ambient temperature was factored in the transient product model. Nonetheless, Design 3 still exhibited superior performance, yielding a 2.3% increase in throughput compared to Design 2.

In summary, the three designs experienced a significant increase in throughput of approximately 9-13%, translating to a reduction in per-product energy consumption by 5-7%. Consequently, the heightened efficiency of the proposed designs could potentially lead to a substantial reduction of 200,000-300,000lbs in electricity-related CO_2e emissions.

Chapter 6 NEW-BUILD DESIGNS

The proposed modifications to the air-side of the blast freezers operating within the four plants previously discussed in this thesis suggest a significant opportunity to enhance their freezing performance. The potential improvement in performance translates to increased production and better energy efficiency. Some of the proposed changes, such as the addition of a drum within the core of the spiral, are difficult to implement in an existing blast freezing system and would likely require a significant capital cost. Hence, this chapter pursues a motivation to explore alternative configurations of blast freezing systems with a “clean sheet of paper” approach that can be pursued by manufacturers of blast freezing systems.

To address this motivation, this chapter intends to answer the question: "*With the knowledge previously gained, how would one construct a more productive and efficient blast freezing system?*" The response to this has led to the creation of two "new-build" spiral blast freezer designs that leverage the insights obtained from the previous chapter's findings. These innovative designs seek to surpass the performance capabilities of the previous models without incurring the additional costs associated with incorporating extra baffling elements in existing freezing systems. To conduct a comparative analysis, the proposed configurations feature the same spiral conveying system, evaporator coils, and evaporator fans that are utilized in Plant 1. Moreover, in the product throughput model, the exact same product is assumed to be frozen, and in the energy balance program the same inputs are provided, aside from the enclosure’s size specifications.

6.1 Tornado

The first of the two blast freezing system configurations, called the “Tornado,” was named based on the flow pattern that is produced. One major challenge observed in all spiral freezer designs that were evaluated across the four plants is that the air is forced to move up and over the spiral instead of following its natural curvature. This flow path results in a greater loss in momentum, as it traverses through the dense belt material experiencing significant flow resistance compared to the flow between the vertical levels of the spiral’s belt. In contrast, the Tornado's design uses cross-opposing fan towers, as depicted in Figure (6.1), in order to allow the internal air flow to “swirl” around the spiral; thereby, producing a vortex or tornado-like effect.

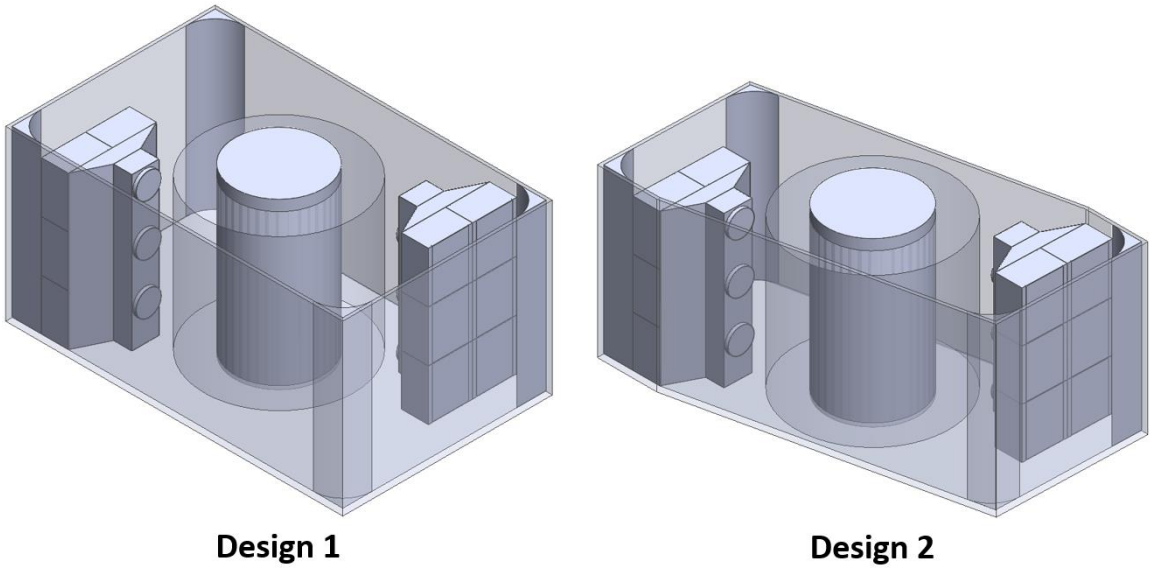

Figure (6.1): 3D models of new-build Tornado designs 1 and 2.

Both designs incorporate a solid drum baffle situated at the core of the spiral, spanning the entire height of the blast freezer’s enclosure. Additionally, the blast freezer enclosure has been engineered to be eight inches taller than the spiral itself, leaving limited space for air bypass both above and below the spiral. The key innovation of these related designs is the incorporation of two opposed stacks of evaporator coils and fans, placed diagonally across from each other. In front of the evaporator coils are

slightly modified versions of the fans used in Plant 1, which have been intentionally spaced along the height of the enclosure. The opposing side's fans have the same distribution but are vertically staggered, such that the discharge of one fan aligns with the gap in the opposing fans, as illustrated in Figure (6.2).

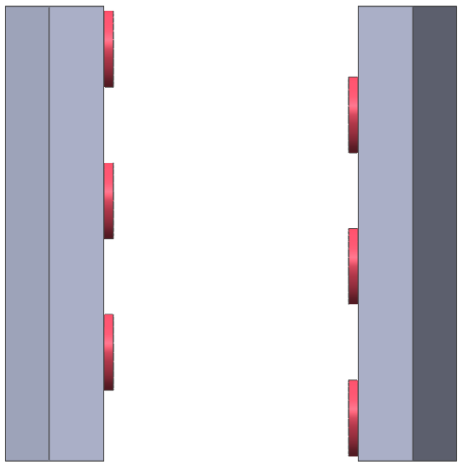

Figure (6.2): Side-view of the two opposing fan and fan shrouds.

A shroud is placed between the evaporator coils and the inlet to each fan in order to channel air into the fan with minimal pressure loss. The enclosure design also includes curved baffles positioned at each vertical corner, effectively directing the flow around the perimeter of the enclosure. While Design 1 and Design 2 share many similarities, the latter features angled side walls that reduce available area on the sides, limiting the potential for air to bypass flowing over product being conveyed on the spiral belt. This feature could be achieved through the insulated walls being angled inward or by utilizing the same enclosure as Design 1 with two flat baffles spanning the height and length of the freezer connecting to the curved transitions.

It is important to consider the size of the enclosure when designing a new blast freezer, as large floor plans can be problematic for facilities with limited square footage. A blast freezer that occupies too much floor space will pose layout challenges within existing food processing plants, as the extra room that a large freezer requires could be better utilized for storage, production areas, and other purposes. Moreover, the volume of the freezer is also an important factor to consider. A freezer that takes up

more volume may run into overhead clearance issues. Table (6.1) provides information for both designs including their required floor area, volume, and effective area and volume (the effective area and volume are related to the size of the smallest rectangular that could encompass the entire floor plan of the freezer).

Table (6.1): Floor plan area, volume, and effective area and volumes of Tornado designs 1 and 2 compared against Plant 1.

Model	Floor Plan Area [ft^2] ($\Delta\%$)	Volume [ft^3] ($\Delta\%$)	Effective Floor Plan Area [ft^2] ($\Delta\%$)	Effective Volume [ft^3] ($\Delta\%$)
Plant 1	**1,050 (-)**	**30,373 (-)**	**1,050 (-)**	**30,373 (-)**
Tornado Design 1	**1,305 (24.3)**	**29,913 (-1.5)**	**1,305 (24.3)**	**29,913 (-1.5)**
Tornado Design 2	**992 (-5.5)**	**22,738 (-25.1)**	**1,305 (24.3)**	**29,913 (-1.5)**

As shown in the table, Design 1 does have a larger footprint compared to the blast freezer operating in Plant 1; however, it does have slightly smaller volume because the height of the enclosure is several feet shorter. Design 2, as currently configured, has both a smaller footprint and volume, although its effective size is the same as Design 1.

Using the same parameters for the porous media representing the evaporator coils and the spiral and the same fan curve as Plant 1's blast freezing system, the two models were simulated, and their velocity streamlines and spiral velocity distribution are shown in Figure (6.3) through Figure (6.5).

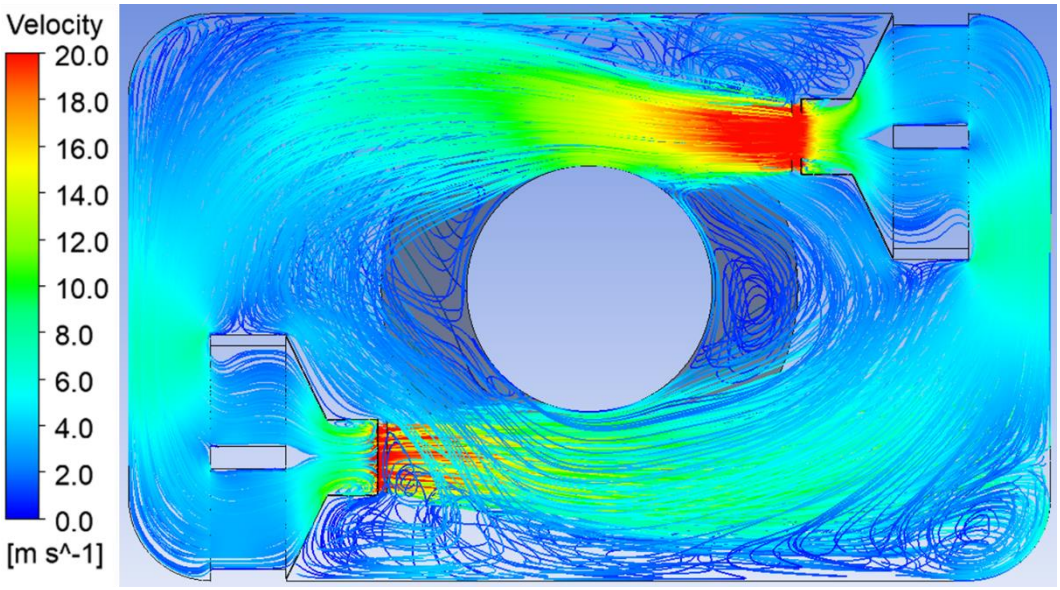

Figure (6.3): Velocity streamline of Tornado Design 1.

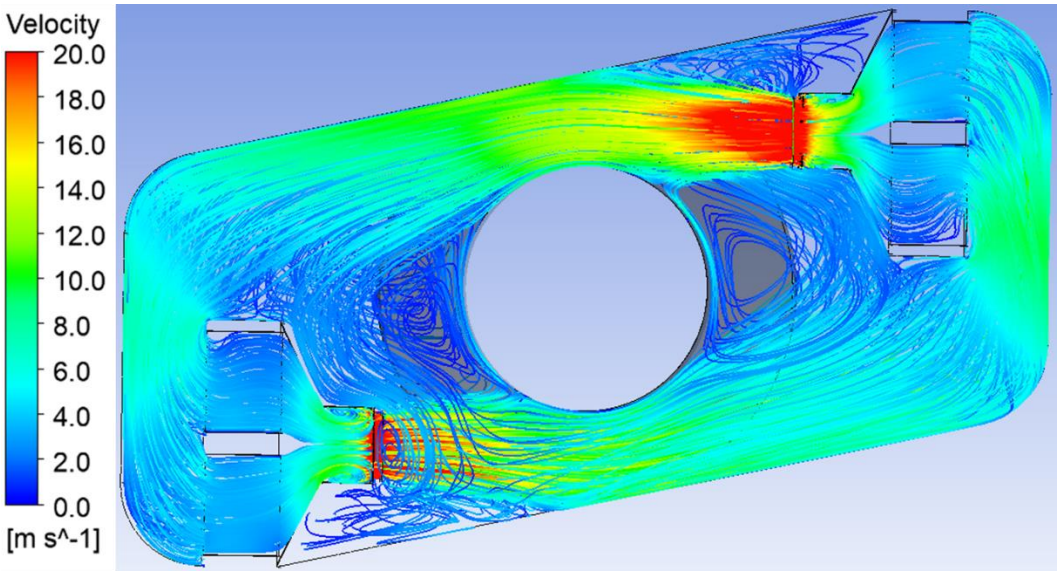

Figure (6.4): Velocity streamline of Tornado Design 2.

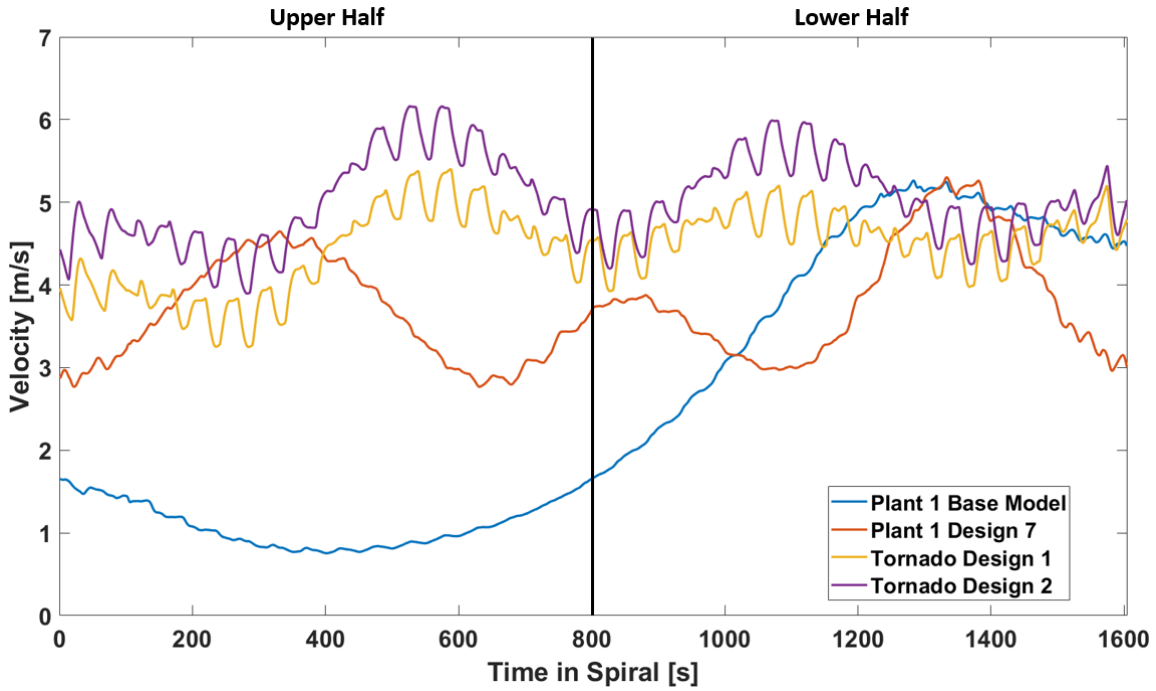

Figure (6.5): Smoothed, (M=200), spiral velocity distributions for Tornado Designs 1 and 2 compared against the Plant 's 1 base model and best performing baffling modification, Design 7. Lower and upper halves of spiral labeled.

The streamlines for both designs demonstrate the intended "tornado effect," with the airflow revolving around the curvature of the spiral. Additionally, they show the spiral experiences high air velocities, in the range of 6-12 m/s, for approximately two-thirds of each revolution, followed by low velocity regions for the remaining one third. It is important to note that the visual difference observed at the two fan discharges in Figure (6.3) and Figure (6.4) can be attributed to the specific elevation at which the image was taken, at the height of the center of the fans in the upper right corner.

Design 2's angled enclosure proved effective in minimizing the airflow bypass along the sides of the enclosure past the spiral as the magnitude of the air velocity distribution is shifted up indicating greater airflow through the spiral. The air velocity distribution also reveals that a greater consistency of velocity throughout the spiral with several peaks near the outlet of the fans. The performance metrics for both designs, compared against the base model and the best performing baffling modification, are shown in Table (6.2).

Table (6.2): Performance metric results for Tornado Designs 1 and 2 compared against Plant 1's base model and Design 7.

Model	Avg. Spiral Velocity [m/s] (Δ%)	Coil Face Velocity [m/s] (Δ%)	Product Throughput [prod/min] (Δ%)	Energy per Product [kJ/prod] (Δ%)	Normalized Annual missions [lb CO2e/yea (Savings)
Plant 1 Base Model	**2.56**	**2.90**	**146.6**	**223.3**	**3,446,000 (-)**
Plant 1 Design 7	**3.73 (45.7)**	**2.83 (-2.4)**	**195.7 (33.5)**	**188.0 (-15.8)**	**2,900,000 (546,000)**
Tornado Design 1	**4.45 (73.8)**	**3.01 (3.8)**	**208.2 (42.0)**	**181.0 (-18.9)**	**2,793,000 (652,000)**
Tornado Design 2	**5.03 (96.5)**	**3.03 (4.5)**	**224.9 (53.4)**	**173.7 (-22.2)**	**2,679,600 (765,400)**

The findings demonstrate that the Tornado designs resulted in a substantial enhancement of the airflow over the base model, and even outperformed the best performing Plant 1 modification, Design 7. Notably, the Tornado Design 2 was found to be superior to the Tornado Design 1, which emphasizes the significance of minimizing routes for airflow to bypass the spiral. The improved average spiral air velocity achieved through these designs is projected to deliver a 42-53% increase in product throughput with a 19-22% reduction in per-product energy consumption. Therefore, implementing these designs can lead to a significant reduction of 650,000-750,000 lb in electrical-related CO_2 emissions.

6.2 ReCirc

The "ReCirc" Design is the last clean-sheet-of paper blast freezer design concept studied. The ReCirc combines the Tornado's fundamental design principles learned from the Plant 1 design study to further elevate the Tornado's already exceptional performance. The ReCirc design approach utilizes some similarities of the Tornado designs by ensuring the recirculating airflow is directed through a greater proportion of the spiral; thereby, addressing one of the primary factors that has hindered performance in the four plants – air bypassing the spiral. The ReCirc design options also endeavor to mitigate the two regions of low velocity that were identified within the Tornado designs, seen in Figure

(6.3) and Figure (6.4). To this end, two unique variants of the ReCirc, as illustrated in Figure (6.6), have been developed and evaluated.

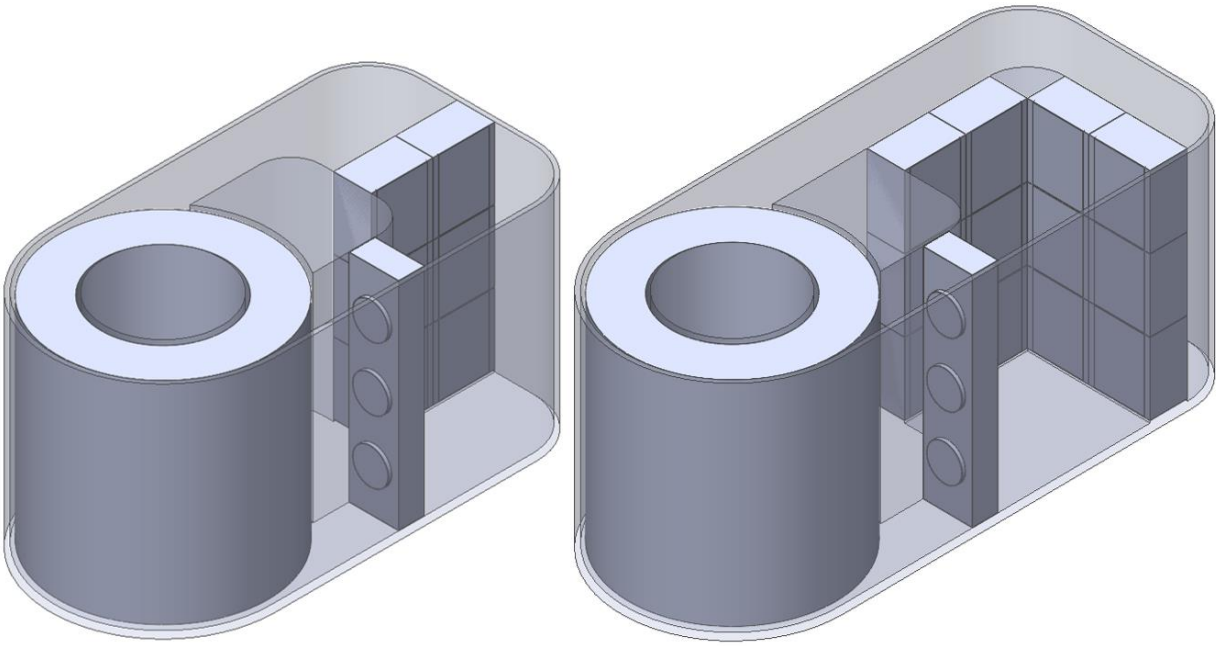

Figure (6.6): 3D models of new-build ReCirc designs 1 and 2.

The key feature of the ReCirc designs is the use of a closed airflow passage that forces the circulation of airflow through the spiral. This design feature prevents air from bypassing around the spiral, limiting it to a single path for air to circulate within the blast freezer's enclosure. This is made possible by incorporating a solid baffle on the interior radius of the spiral and the walls of the freezer encompassing the perimeter of the spiral, with openings only for the air to flow in to and out of the spiral belt. The baffles span the height of the blast freezer's enclosure, leaving a clearance of three inches above and below the spiral; thereby, mitigating available avenues for air bypass.

Another key feature of the ReCirc designs is the reduction in the number of fans used to circulate airflow, from six (6) to three (3). This reduction results in a two-fold benefit as less electrical power is needed to operate the fans and, therefore, less parasitic heat is generated inside the enclosure.

The fan housing, a modified version of the fan housing utilized in Plant 1, spaces the discharge air flow more uniformly throughout the height of the spiral.

The distinguishing factor between the two ReCirc designs lies in the incorporation of an additional stack of evaporator coils in Design 2. It is possible that Design 1's single stack of coils could, potentially, be insufficient to meet the required cooling capacity, thus necessitating the implementation of two complete stacks in Design 2.

The construction of the ReCirc can be executed in two ways, the first would be to have the walls of the insulated enclosure form the large curves depicted in Figure (6.6). Second, the enclosure would have a rectangular floor plan and uses appropriately contoured baffles to create the curves in each end of the freezer. The latter approach is more viable, not only for ease of construction but also for providing better access to the spiral for maintenance, cleaning, or product blockages. In either method the ReCirc designs have a comparable floor space requirement with the Plant 1's blast freezing system, thanks, in part, to the width of the enclosure being only marginally wider than the spiral itself. Table (6.3) compares the floor area, volume, and effective sizes of the ReCirc designs against Plant 1's blast freezer.

Table (6.3): Floor plan area, volume, and effective area and volumes of Tornado designs 1 and 2 compared against Plant 1.

Model	Floor Plan Area [ft^2] ($\Delta\%$)	Volume [ft^3] ($\Delta\%$)	Effective Floor Plan Area [ft^2] ($\Delta\%$)	Effective Volume [ft^3] ($\Delta\%$)
Plant 1	**1,050 (-)**	**30,373 (-)**	**1,050 (-)**	**30,373 (-)**
ReCirc Design 1	**847 (-19.3)**	**18,102 (-40.4)**	**911 (-13.3)**	**19,465 (-35.9)**
ReCirc Design 2	**1,036 (-1.3)**	**22,154 (-27.1)**	**1,077 (2.6)**	**23,517 (-22.6)**

The table shows that both ReCirc designs, in their current modeled form, boast a smaller floor space and volume when compared to the freezing system at Plant 1. Although it is worth noting that Design 2,

would realistically occupy a floor area that is approximately 2.6% larger than Plant 1's. Both ReCirc designs offer a reduced size compared to the Tornado with a footprint virtually equivalent to Plant 1 while occupying a smaller volume.

Utilizing the same porosity values for the coils and spiral, and the fan curve of Plant 1's freezer, the two ReCirc models were simulated, resulting in the velocity streamlines and spiral velocity distributions showcased in Figure (6.7) through Figure (6.9).

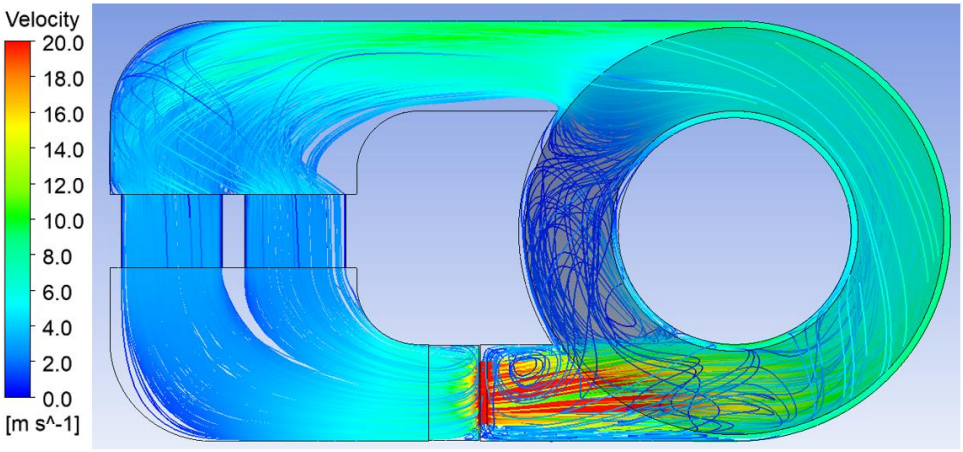

Figure (6.7): Velocity streamline of Recirc Design 1.

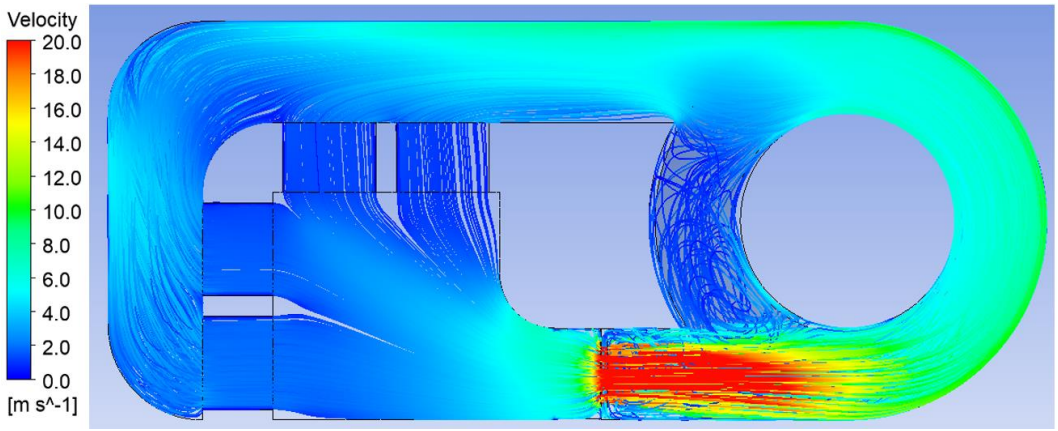

Figure (6.8): Velocity streamline of Recirc Design 2.

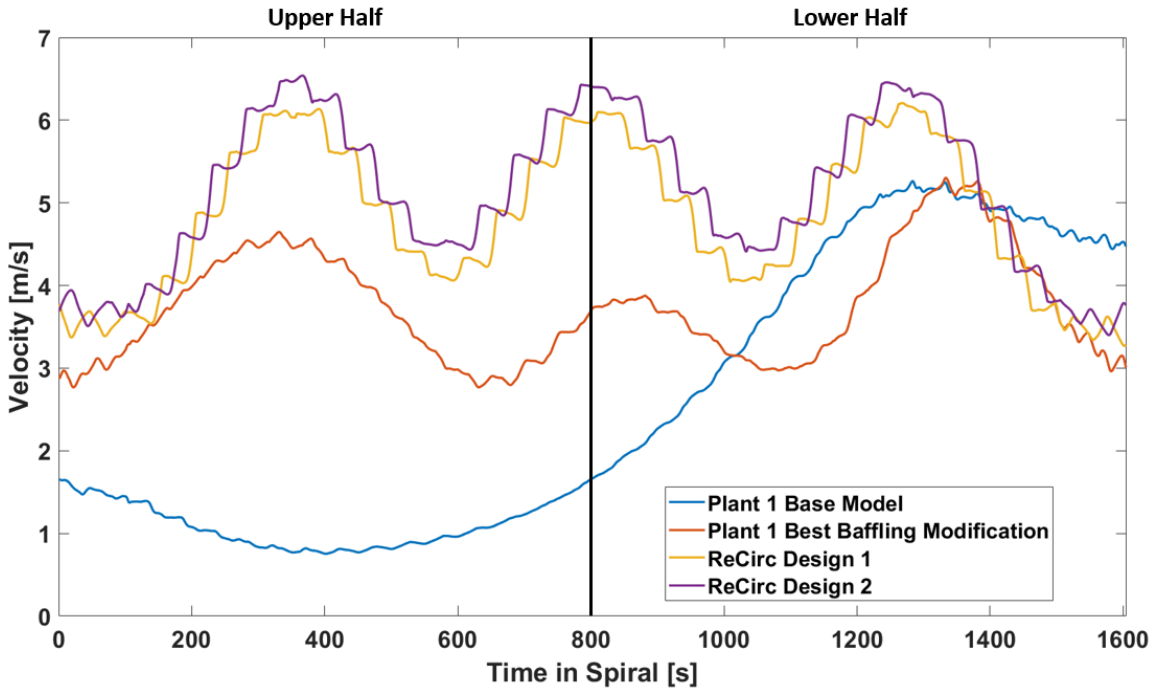

Figure (6.9): Smoothed, (M=200), spiral velocity distributions for Recirc designs 1 and 2 compared against the Plant 's 1 base model and best performing baffling modification, Design 7. Lower and upper halves of spiral labeled.

The ReCirc design demonstrates the substantial impact that a closed passage can have on airflow, as evidenced by the streamlines. As such, only a fraction of the spiral experiences a region of low velocity at the nine o'clock position on the spiral, emphasizing the critical role of limiting available flow paths. This restriction results in the conveyed product receiving a larger proportion of the volume flow rate of air generated by the fans. An examination of the velocity distribution highlights three distinct peaks, aligned with the three fan discharges. There exists a noticeable difference of approximately 2 m/s in the relative height between the peaks and troughs in the distribution. To achieve a more balanced velocity profile and to further enhance overall freezing system performance, the incorporation of a flow distributor at the fan discharge could prove to be a valuable addition. The performance metrics for both designs are compared against the base model and the best-performing baffling modification, with the results shown in Table (6.4): Performance metric results for Recirc designs 1 and 2 compared against Plant 1's base model and Design 7. *Assumes evaporators meet load capacity.Table (6.4).

*Table (6.4): Performance metric results for Recirc designs 1 and 2 compared against Plant 1's base model and Design 7. *Assumes evaporators meet load capacity.*

Model	Avg. Spiral Velocity [m/s] (Δ%)	Coil Face Velocity [m/s] (Δ%)	Product Throughput [prod/min] (Δ%)	Energy per Product [kJ/prod] (Δ%)	Normalized Annual Emissions [lb CO2e/year] (Savings)
Plant 1 Base Model	**2.56**	**2.90**	**146.6**	**223.3**	**3,446,000 (-)**
Plant 1 Design 7	**3.73 (45.7)**	**2.83 (-2.4)**	**195.7 (33.5)**	**188.0 (-15.8)**	**2,900,000 (546,000)**
ReCirc Design 1	**4.85 (89.0)**	**2.91 (0.3)**	**225.7 (53.9)***	**132.8 (-40.53)***	**2,083,000 (1,362,000)***
ReCirc Design 2	**5.12 (100.0)**	**1.2, 1.76 (-58.6, -39.3)**	**233.6 (59.3)***	**131.0 (-41.3)***	**2,048,000 (1,397,000)***

The data presented highlights the substantial enhancements that the ReCirc designs have achieved in the average spiral air velocity, surpassing not only the base model of Plant 1 but also outperforming the best design modification, Design 7. Notably, this elevated performance was accomplished through the use of only three (3) fans, demonstrating that excessive use of fans is not a necessity to achieve high air velocities, provided that the enclosure design limits the flow solely to the spiral.

Reducing the number of fans does lead to a decrease in face velocity of air at the evaporator coils, as typical enclosures are already designed to minimize bypass around the evaporators. This trade-off between the two designs highlights that while Design 1 produces higher coil face velocities, it only has half the number of evaporators and hence half the capacity of Plant 1's base model coils, given they have the same face velocity. On the other hand, Design 2 has two sets of coils, doubling the frontal area, but with approximately half the average face velocity, as observed in the table.

The data shown in the table is based on the idealized scenario where the evaporator coils have sufficient capacity to meet predicted throughput rates, respectively. As such, the implementation of these designs can lead to a 54-60% increase in product throughput and a 41% reduction in per-product

energy consumption, which, in turn, can reduce 1.4 million lb of CO_2e emissions, representing a commendable advancement towards environmentally sustainable blast freezing.

Further analysis of the cooling capacity is necessary when considering the feasibility of these designs given the reduction of either the number of evaporator coils or average face velocity. Regardless, the ReCirc designs have demonstrated that improved air flow patterns achieved by strategic interior design can significantly enhance freezing performance.

Chapter 7 CONCLUSIONS AND RECOMMENDATIONS

7.1 Conclusions

This thesis examined potential avenues for improving the energy efficiency and production capacity of blast freezers through the investigation of the spiral freezing systems currently operating in four different food processing plants. A comprehensive energy balance was conducted on all four blast freezers to identify the key sources of energy consumption, and to further determine which sources would be the focus of this work. The results of the energy balances revealed that, apart from the heat load of products being frozen, the heat load from air infiltration and the cumulative heat and power load required to operate the fans, were the largest available avenues for improving system performance and were deemed the main focus of this research.

7.1.1 Air Infiltration

An overabundance of air infiltration inside a blast freezer can result in a considerable decrease in the performance. The infiltration of warm air into the system increases both the sensible and latent heat load on the evaporator coils and the latent load from infiltration compounds the formation of frost on specific surfaces, ultimately reducing overall performance. The buildup of frost on the evaporator coils can lead to greater pressure losses and thermal resistance, curtailing heat transfer with the cold evaporator surfaces which decreases freezing capacity. Furthermore, excessive air infiltration raises the rate of frost accumulation, requiring more frequent coil defrost cycles; thereby, impeding airside performance. As illustrated in **Section 5.2.4**, even 1/32nd of an inch of frost accumulation can potentially reduce the average spiral velocity by 4.5%. Therefore, the mitigation of air infiltration is vital to ensure efficient operation of the system.

Completely eliminating the unwanted infiltration of warm plant air into a spiral freezer is an infeasible task as the enclosure requires infeed and outfeed openings for dynamic loading of product. Nonetheless, several measures and techniques can be implemented to limit infiltration to acceptable levels. The initial step is performing a test to determine the amount of air infiltration that a system is currently permitting. In this regard, CO_2 was utilized as a tracer gas to conduct infiltration tests on the four blast freezing systems. The findings from these tests revealed that Plants 2 through 4 boasted below-average to exceptionally low levels of infiltration, thereby necessitating no further investigation. Conversely, Plant 1 exhibited elevated levels of infiltration and, therefore, was assessed for potential sources of infiltration.

Upon investigation, it was discovered that the primary drivers of infiltration into the freezer were plant air pressure imbalances resulting from the infeed and outfeed being situated in two distinct processing rooms. This pressure disparity between the two physically segregated spaces was the consequence of make-up air unit operation as well as several zone doors within the plant that exacerbated air imbalance. In order to mitigate infiltration, it is highly recommended that the placement of product openings (blast freezing system infeed and outfeeds) be in the same contiguous plant space/room, whenever possible. Furthermore, Plant 1's freezer incorporated an Automatic Pressurization System (APS) designed to help balance the pressure within the enclosure, which was not being utilized during operation. By balancing air pressure relationships between the plant zones where the infeed and outfeed were located, principally, along with utilizing the APS, secondarily, enabled Plant 1 to reduce its infiltration levels significantly from 2.99 ACH to a more acceptable level of 0.77 ACH. Lastly, it is advised to keep the physical openings for both the infeed and outfeeds as small as possible, as larger openings into the enclosure result in a greater entrainment of air as product enters and exits the freezer.

7.1.2 Modeling Method

The parasitic heat and power load of the fans, when combined, constitute nearly half of the energy consumption necessary to operate a blast freezing system. While decreasing fan speed can lower power consumption, it also leads to extended freezing times and reduced product throughput. Thus, the optimal approach for enhancing both throughput capacity and energy efficiency necessitates improving airflow within the freezer so that the fan power is used most effectively. To this end, CFD models of the four blast freezers were developed to analyze and enhance the airside performance.

Capturing the intricate features of a blast freezer through fully-detailed modeling is impractical, as it requires an overwhelming number of elements and computational power. Therefore, this work utilized a simplified method of modeling blast freezers that could effectively examine the impact of these components on the larger scale flow field. This was achieved through the utilization of porous media, which reduced the intricate features to simple geometries within the computational domain. The resulting effect of these components on the flow field was captured by a resistance to flow, characterized by porosity coefficients. These coefficients were obtained from pressure drop vs. velocity data, acquired from small-scale CFD studies, manufacturer's data, or correlations of similarly shaped geometries, respectively.

In order to establish validity and reliability of the assumptions and simplifications made in the modeling of blast freezers, an experimental apparatus, known as the "Phantom", was utilized. The aim was to compare the predicted heat transfer coefficients, derived from the CFD velocities, with the data collected by the Phantom. The predicted heat transfer coefficients were calculated through the use of convection correlations and radiation. Upon comparing the CFD heat transfer values with the Phantom data, a qualitative agreement was observed, leading to the conclusion that the application of porous media was a valid method of simplifying the simulation process of blast freezing systems.

7.1.3 Existing Designs

A series of design studies were conducted on all four of Plant's blast freezers. A detailed analysis was performed on the CFD results of the base model's airside performance to identify and guide the implementation of baffling elements that could enhance air velocity over the conveyed product. The findings of these studies is summarized in Table (7.1) and compares the base model of each plant's freezing system (current state) with the predicted performance should recommended modifications be made to each freezing system to yield improved performance.

Table (7.1): Summary of performance metrics for all four plants base models compared against their best performing design modification.

Model	Spiral Velocity [m/s] (Δ%)	Coil Face Velocity [m/s] (Δ%)	Product Throughput (Δ%)	Energy per Product/Mass (Δ%)	Annual Emissions [lb CO_2e/year] (Savings)
Plant 1 Base Model	**2.56 (-)**	**2.90 (-)**	**146.6 (-) [prod/min]**	**223.3 (-) [kJ/prod]**	**3,446,000 (-)**
Plant 1 Design 7	**3.73 (45.7)**	**2.83 (-2.4)**	**195.7 (33.5)**	**188.0 (-15.8)**	**2,900,000 (546,000)**
Plant 2 Base Model	**1.94 (-)**	**1.54 (-)**	**3,704.6 (-) [kg/hr]**	**779.1 (-) [kJ/kg]**	**7,661,000 (-)**
Plant 2 Design 1	**2.22 (14.4)**	**1.54 (0.0)**	**3,929.9 (6.2)**	**759.1 (-2.6)**	**7,463,000 (198,000)**
Plant 3 Base Model	**2.86 (-)**	**3.94 (-)**	**150.0 (-) [prod/min]**	**229.9 (-) [kJ/prod]**	**5,491,000 (-)**
Plant 3 Design 2	**3.78 (32.2)**	**3.57 (-9.4)**	**255.3 (70.23)**	**185.3 (-19.40)**	**4,425,000 (1,066,000)**
Plant 4 Base Model	**1.13 (-)**	**2.80 (-)**	**5,897.6 (-) [kg/hr]**	**426.2 (-) [kJ/kg]**	**4,201,000 (-)**
Plant 4 Design 3	**1.99 (76.1)**	**2.74 (-2.1)**	**6,681.4 (13.3)**	**395.5 (-7.1)**	**3,900,000 (301,000)**

It is evident from the table that strategically placed baffling elements can be expected to significantly improve the airside performance of each existing blast freezing system. The improved performance

observed in each plant's design modification is expected to result in enhanced throughput capabilities and lower per-product energy consumption. This translates into a substantial reduction in electricity-related CO_2e emissions, thus highlighting the potential environmental benefit of such an approach.

It should be noted that the selection of baffling elements to enhance airside performance is highly dependent on the existing design configuration, as some types of elements offer greater advantages than others. For instance, the impact of baffles intended to mitigate recirculation zones would be negligible on a design with already minimal flow recirculation. In general, the most impactful measures for improving airside performance involve the deployment of baffles that evenly distribute flow throughout the spiral, or those that effectively prevent flow bypass in various directions, such as through, around, over, or under the spiral. The former is especially important when the uneven flow distribution is focused on the product that is further along in the freezing process. Maximizing the air velocity over product that has just entered, which is the warmest, will take advantage of the greater heat transfer potential. Reducing flow bypass is important as it leads to more efficient use of the fans' energy consumption, by directing a greater proportion of it towards cooling the conveyed product rather than simply circulating air around the enclosure.

7.1.4 New-Build Designs

The development of two "new-build" design configurations, namely the "Tornado" and the "ReCirc", was accomplished by employing a "clean sheet of paper" approach. The goal was to tackle the question: "*With the knowledge previously gained, how would one construct a more productive and efficient blast freezing system?*" Utilizing the same spiral, coils, and fan components as Plant 1's blast freezer, the two designs were aimed at exploring whether airside enhancements could be made without requiring numerous baffling elements. The designs utilized the concept of an alternative flow path, one that follows the curvature of the spiral, which was thought to be more effective than the current flow

path over and around the spiral, which was used in the four blast freezers that were studied. Moreover, the fans were arranged vertically in a distributed manner throughout the height of the spiral, thereby facilitating a more uniform airflow without necessitating the incorporation of an additional baffling component. Table (7.2) presents a summary and comparison of the performance metrics for the most successful iteration of each of the two designs with Plant 1 and its most efficient design modification.

*Table (7.2): Summary of performance metrics for Plant 1's base model and best performing design modification compared against best performing new-build design modification. *Assumes evaporators meet load capacity.*

Model	Spiral Velocity [m/s] (Δ%)	Coil Face Velocity [m/s] (Δ%)	Product Throughput [prod/min] (Δ%)	Energy per Product [kJ/prod] (Δ%)	Annual Emissions [lb CO2e/year] (Savings)
Plant 1 Base Model	**2.56 (-)**	**2.90 (-)**	**146.6 (-)**	**223.3 (-)**	**3,446,000 (-)**
Plant 1 Design 7	**3.73 (45.7)**	**2.83 (-2.4)**	**195.7 (33.5)**	**188.0 (-15.8)**	**2,900,000 (546,000)**
Tornado Design 2	**5.03 (96.5)**	**3.03 (4.5)**	**224.9 (53.4)**	**173.7 (-22.2)**	**2,679,600 (765,400)**
ReCirc Design 2	**5.12 (100.0)**	**1.2, 1.76 (-58.6, -39.3)**	**233.6 (59.3)***	**131.0 (-41.3)***	**2,048,000 (1,397,000)***

The results of the table demonstrate that the two new-build design configurations outperformed Plant 1's best design iteration by a substantial margin. This serves as a compelling indication that the airflow path around the spiral, as proposed by these designs, represents the optimal flow pattern.

In conclusion, the development of the "Tornado" and "ReCirc" new-build designs, and the design modifications of the four plants, represent a significant advancement in the pursuit of a more efficient and productive blast freezing process. The adoption of these designs or similar configurations holds the potential to significantly reduce energy consumption and carbon footprint, thereby paving the way for a more environmentally conscious and economically viable blast freezing process. It is recommend that

blast freezer manufacturers prioritize the implementation of these, or similar designs, to meet the evolving demands of the food industry and reduce the environmental impact of their operations.

7.1 Recommendations for Future Work

Future research efforts may be directed towards advancing the present work by exploring the following avenues: refining fan modeling techniques, enhancing correlations for forced convection heat transfer coefficients, conducting sub-scale CFD studies on the spiral as an alternative to pressure drop correlations, and analyzing the evaporator coils' suitability in the ReCirc designs.

7.1.1 Fan Modeling

A more sophisticated approach to the fan boundary conditions currently employed within Ansys® Fluent would enhance the accuracy of CFD modeling of blast freezing systems. The current limitations of the fan boundary conditions used in the CFD models is likely attributable to the assumption of uniform flow normal to the fan discharge surfaces, which is not representative of the actual velocity profile for the fan types commonly applied to blast freezing systems. Axial fans, for instance, have a hub that limits velocity at the center, resulting in a parabolic velocity profile with low velocity at the center and the perimeter of the housing and high velocity in between. Similarly, un-ducted centrifugal plug fans create a highly swirling flow due to the rotation of the impeller and therefore, the velocity profile has a large tangential velocity component that is not captured. Neglecting this swirling component is one possible explanation for the observed disagreement between the Phantom and CFD model results for Plant 2 and Plant 4, both of which use centrifugal plug fans.

To achieve more accurate modeling of the fans, two promising methods can be explored: incorporating radial and tangential velocity components into the boundary condition or adopting a

Multiple Reference Frame (MRF) CFD simulation. The former method would involve conducting a detailed analysis of the fan blade geometry to determine the radial and tangential components as a function of spatial position at the discharge plane. The latter approach entails fully modeling the fan geometry and defining a region around the blades or impeller, which will be split into multiple reference frames by the CFD software. These reference frames will then rotate around the stationary mesh at the rotational speed of the fan, and the solutions for each reference frame will be combined to generate the flow field for the domain around the fans [34]. While it is important to note that modeling fan blades with the level of detail required for an MRF simulation will increase the computational expense, it will ultimately provide more accurate results compared to the present 2D fan boundary condition.

7.1.2 Forced Convection Correlations

The discrepancy observed between the CFD models and the Phantom could be attributed to three potential sources. First, the CFD model is somewhat limited in its ability to capture specific, local and small scale, flow phenomena; this was necessary in order to enable making the problem computationally tractable. Second, the assumption that the temporally-averaged velocities collected in the models can be used to approximate the instantaneous heat flux data acquired by the Phantom could be incorrect. Lastly, there may exist some inherent errors in the method employed to predict heat transfer coefficients solely from the velocity magnitude.

To address the latter disparity, employing more representative forced convection correlations would potentially improve the comparison between the CFD models and the Phantom. The current recipes used to predict the forced convection heat transfer over the food product being frozen assumes that the direction of the air velocity over product is parallel to the exposed product surface. However, in the CFD models, the vertical component of the velocity vector at a given location throughout the point cloud is almost always non-zero, as such, the individual contribution of the vertical component to heat

transfer is not adequately accounted when using the existing forced convection correlations. In addition, the Reynolds numbers for the air flow across the product is in a transitional regime in many locations which compounds the inability of established correlations to accurately predict the convective heat transfer coefficient at the product surface.

Therefore, it is proposed that new correlations should be developed that account for the incoming air angle relative to the surface of interest. These correlations would be utilized to predict the forced convective heat transfer coefficient. This approach would ensure that the vertical component's contribution to the heat transfer is appropriately incorporated, thereby reducing one possible source of discrepancy in the comparison.

7.1.3 Sub-Scale CFD Studies

The substitution of sub-scale CFD studies, in lieu of pressure drop correlations, presents a promising opportunity for more accurately determining the porosity coefficients required by the surrogate porous media models. The pressure drop correlations, designed to predict pressure drop as a function of velocity, are intended to be representative of the simplified geometry utilized in the model. However, a more precise method involves modeling the specific geometry of interest with CFD to determine the pressure drop as a function of velocity. The spiral porous region would particularly benefit from this approach, given the distinct geometries of the two flow paths, through the belt and between successive levels of the belt, which were the most dissimilar from the geometries of the correlations employed.

7.1.4 Evaporator Coil Analysis

Further investigation is required to evaluate the suitability of the evaporator coils in the ReCirc designs with respect to meeting the necessary cooling capacity. The reduction in the number of

evaporator coils in ReCirc Design 1, as well as the low face velocities observed in ReCirc Design 2, has the potential of substantially decreasing the cooling capacity of evaporator coils typically selected for these low temperature freezing systems. Therefore an investigation of the cooling capacity of the coils as a function of face velocity in each design, is required. However, it is doubtful that the current coils modeled will be a satisfactory fit, as the expected increase in throughput, coupled with the drop in face velocity, would exacerbate the gap between available and required capacity.

The next step would be to assess whether the throughput rate can be reduced sufficiently to allow the evaporator coils to meet the cooling load required. If this measure fails to yield the desired outcome, then alternative coils need to be identified. Employing an evaporator coil with a larger surface area, while simultaneously slowing down the throughput, may potentially increase the available cooling capacity enough to meet the required loads.

References

[1] P. Dempsey and P. Bansal, “The art of air blast freezing: Design and efficiency considerations,” *Applied Thermal Engineering*, vol. 41, pp. 71–83, Aug. 2012, Doi: 10.1016/J.APPLTHERMALENG.2011.12.013.

[2] U.S. Energy Information Administration, “U.S. Energy Facts Explained,” 2021.

[3] U.S. Energy Information Administration, “TOTAL ENERGY,” 2023.

[4] Office of ENERGY EFFICIENCY & RENEWABLE ENERGY, “Manufacturing Energy and Carbon Footprints,” 2018.

[5] United Nations, “GLOBAL ISSUES Population,” 2022.

[6] IPCC, “Framing and Context,” in Global Warming of 1.5°C: IPCC Special Report on Impacts of Global Warming of 1.5°C above Pre-industrial Levels in Context of Strengthening Response to Climate Change, Sustainable Development, and Efforts to Eradicate Poverty, Cambridge: Cambridge University Press, pp. 68–69, 2022.

[7] M. Odey, "Meat carton blast chilling/freezing cabinet performance improvements," Refrigeration Science and Technology Series, vol. 1, pp. 118-124, 2006.

[8] E. Kolbe, Q. Ling, and G. Wheeler, "Conserving energy in blast freezers using variable frequency drives," in National Industrial Energy Technology Conference, [Texas A&M University], 1999, 2004.

[9] A. Khenien, A. Benattayallah, and G. Tabor, “CFD Simulation of an Industrial Spiral Refrigeration System,” Energies, vol. 12, no. 17, p. 3358, Aug. 2019, Doi: 10.3390/en12173358.

[10] Don J. CLELAND, “Prediction of Food Thermal Properties to Enable Accurate Design of Food Refrigeration Processes,” in *International Congress of Refrigeration*, 2019.

[11] W. M. Rohsenow, J. P. Hartnett, and Y. I. Cho, *Handbook of Heat Transfer*. McGraw-Hill, 1998.

[12] S. W. Churchill and R. Usagi, “A general expression for the correlation of rates of transfer and other phenomena,” AIChE Journal, vol. 18, no. 6, pp. 1121–1128, Nov. 1972, Doi: 10.1002/aic.690180606.

[13] W. F. Stoecker, *Industrial Refrigeration* , vol. 2. Troy: Business News Publishing Company, 1995.

[14] D. T. Reindl and T. B. Jekel, “Infiltration Rate Determination for Low Temperature Freezing Systems,” ASHRAE, vol. 114, no. 2, Jul. 2008.

[15] R. Kent, “Services,” *Energy Management in Plastics Processing*, pp. 105–210, Jan. 2018, Doi: 10.1016/B978-0-08-102507-9.50004-0.

[16] Heat Transfer G.F. Nellis and S.A. Klein Cambridge University Press, 2009

[17] FAO, "The future of food and agriculture - Drivers and triggers for transformation," The Future of Food and Agriculture, no. 3, Rome, 2022. Doi: 10.4060/cc0959en

[18] ANSYS Inc., "ANSYS Fluent 12.0 User's Guide," 2012R1, Section 7.2.3 Porous Media Conditions.

[19] S.A. Klein, "Engineering Equation Solver (EES)," Professional V11.531. [Online]. Available: https://fChartSoftware.com.

[20] W.M. Kays and A.L. London, Compact Heat Exchangers, 3rd ed. Malabar, FL: Krieger Publishing, 1984.

[21] R.L. Webb, "Entrance and Exit Losses for Developing Flow in Parallel Plate Channels," Heat Transfer Engineering, vol. 27, no. 10, pp. 17-26, 2006.

[22] “Modeling Turbulence,” *Washington University*, no. 10. pp. 12–19, Sep. 29, 2006.

[23] ANSYS Inc., "ANSYS Fluent 12.0 User's Guide," 2012R1, Section 4.12.4 Enhanced Wall Treatment.

[24] H. Versteeg and W. Malalasekera, An Introduction to Computational Fluid Dynamics: The Finite Volume Method, 2nd ed. Essex, UK: Pearson Education Limited, 2007.

[25] ANSYS Inc., "ANSYS Fluent 12.0 User's Guide," 2012R1, Section 18.1.1 Pressure-Based Solver.

[26] ANSYS Inc., "ANSYS Fluent 12.0 User's Guide," 2012R1, Section 18.3.1 Spatial Discretization.

[27] J. W. Slater, “Examining Spatial (Grid) Convergence,” *NASA.gov*, Feb. 10, 2021.

[28] A. ElCheikh and M. ElKhoury, “Effect of Local Grid Refinement on Performance of Scale-Resolving Models for Simulation of Complex External Flows,” *Aerospace*, vol. 6, no. 8, p. 86, Aug. 2019, Doi: 10.3390/aerospace6080086.

[29] E. Alar, D. T. Reindl, G. F. Nellis, and T. Young, “Optimizing Airflow in Spiral Blast Freezers”, 2023 [Submitted for Publication] Author Contact: alar@wisc.edu

[30] E. Alar, D. T. Reindl, G. F. Nellis, and T. Young, “Optimizing Airflow in Spiral Blast Freezers,” in *International Refrigeration and Air Conditioning Conference* , Purdue-West Lafayette, Jul. 2022.

[31] J. H. Lienhard V, “Heat Transfer in Flat-Plate Boundary Layers: A Correlation for Laminar, Transitional, and Turbulent Flow,” *J Heat Transfer*, vol. 142, no. 6, Apr. 2020, Doi: 10.1115/1.4046795.

[32] ANSYS Inc., "ANSYS Fluent 12.0 User's Guide," 2012R1, Section 7.3.18 Fan Boundary Conditions.

[33] U.S. Environmental Protection Agency, "eGRID2021 Summary Tables," Jan. 2023.

[34] A. Wimshurst, "[Fluid Mechanics 101]. Multiple Reference Frame (MRF) Approach for Turbomachinery," [Video]. May 24, 2020.

Appendix A

Table (A.1): Operating air conditions and thermal properties for Plants 1 through 4.

Plant	Operating Air Temperature [K] (°F)	Operating Air Pressure [Pa]	Density ρ [kg/m^3]	Viscosity μ [Pa-s]
1	241.5 (-25)	101,325	1.462	1.57E-05
2	235.9 (-35)	101,325	1.497	1.54E-05
3	239.8 (-28)	101,325	1.472	1.56E-05
4	243.2 (-22)	101,325	1.452	1.58E-05

Table (A.2): Porous media coefficients for plants 1 through 4.

Plant	Resistance Term	x-dir	y-dir	z-dir
1	Viscous [1/m^2]	411,073	411,073	0
	Inertial [1/m]	8.143	8.143	1,000
2	Viscous [1/m^2]	0	760,912	760,912
	Inertial [1/m]	1,000	11.74	11.74
3	Viscous [1/m^2]	0	946,111	946,111
	Inertial [1/m]	1,000	4.245	4.245
4	Viscous [1/m^2]	0	270,473	270,473
	Inertial [1/m]	1,000	17.18	17.18

Table (A.3): Porous media coefficients of plants 1 through 4's spiral.

Plant	Belt Coverage [%]	Resistance Term	x-dir	y-dir	z-dir
1	50	Viscous [1/m^2]	92.64	68801	92.64
		Inertial [1/m]	0.3631	5.618	0.3631
2	67	Viscous [1/m^2]	183.2	83322	183.2
		Inertial [1/m]	0.4645	7.991	0.4645
3	50	Viscous [1/m^2]	388	78024	388
		Inertial [1/m]	0.6201	7.549	0.6201

4	50	Viscous [1/m^2]	183.2	92998	183.2
		Inertial [1/m]	0.4645	7.213	0.4645

Table (A.4): Walkway and spiral support structure porosity coefficients for plants 1 through 4.

Component		Walkway			Spiral Support Structure		
Plant	Resistance Term	x-dir	y-dir	z-dir	θ-dir	r-dir	z-dir
1	Viscous [1/m^2]	0	2.056E+06	0	0	115,610	0
	Inertial [1/m]	1000	153.1	1000	1000	11.55	0
2	Viscous [1/m^2]	0	0	0	-	-	-
	Inertial [1/m]	1000	25.63	1000	-	-	-
3	Viscous [1/m^2]	0	0	0	-	-	-
	Inertial [1/m]	1000	135.1	1000	-	-	-
4	Viscous [1/m^2]	0	0	0	0	115,610	0
	Inertial [1/m]	1000	25.63	1000	1000	11.55	0

Table (A.5): Fan curve-fit coefficients with correspond lower and upper velocity bounds for Plants 1 through 4.

Plant	a_0	a_1	a_2	a_3	a_4	a_5
1	1589.89634	-71.6094163	-0.16975422	0.36175799	-0.0209997577	0.000313021173
	Lower Limit [m/s]			Upper Limit [m/s]		
	0			26.8608913		
2	1768.58568	-95.7538238	22.2130497	-1.33511228	0.001698469	-
	Lower Limit 1 [m/s]			Upper Limit 1 [m/s]		
	0			13.4486893		
	-469829.052	149633.826	-18767.2359	1164.59898	-35.8323948	0.437592891
	Lower Limit 2 [m/s]			Upper Limit 2 [m/s]		
	13.4486893			21.1737491		
3	1677.54354	-93.7271296	-16.3383774	3.04828413	-0.174700111	0.00319191514
	Lower Limit [m/s]			Upper Limit [m/s]		

	0			**19.3397275**		
4	2304.064	-67.8854249	24.8770341	-6.21151154	0.834802372	-0.040870711
	Lower Limit 1 [m/s]			**Upper Limit 1 [m/s]**		
	0			**10.2127214**		
	112019.025	-46346.1147	7646.98261	-614.998002	24.0676505	-0.367958038
	Lower Limit 2 [m/s]			**Upper Limit 2 [m/s]**		
	10.2127214			**17.9743845**		

Appendix B

Table (B.1): Data summary of the Mesh Sensitivity Analysis for Plant 1.

Mesh	Global Mesh Size [mm]	Element Count	Avg. Spiral Velocity [m/s]	Avg. Coil Velocity [m/s]	Total Fan Flow Rate [m^3/s]
Coarse	156.25	7,575,811	2.663 ± 0.267	2.852 ± 0.058	104.7 ± 2.81
Medium	125	12,933,027	2.646 ± 0.025	2.879 ± 0.022	105.6 ± 0.05
Fine	100	22,381,892	2.617 ± 0.062	2.879 ±0.026	105.5 ± 0.05
Very Fine	80	39,575,137	2.595 ± 0.094	2.881 ± 0.021	105.8 ± 0.04

Table (B.2): Data summary of the Mesh Sensitivity Analysis for Plant 2.

Mesh	Global Mesh Size [mm]	Element Count	Avg. Spiral Velocity [m/s]	Avg. Coil Velocity [m/s]	Total Fan Flow Rate [m^3/s]
Coarse	156.25	8,072,237	1.705 ± 0.168	1.327 ± 7.12E-03	66.71 ± 1.27
Medium	125	13,934,729	2.007 ± 0.020	1.550 ± 1.94E-03	65.13 ± 0.15
Fine	100	24,727,716	1.909 ± 0.095	1.532 ± 9.04E-03	63.91 ± 0.50
Very Fine	80	44,372,887	2.032 ± 0.113	1.527 ± 0.0329	63.29 ± 0.68

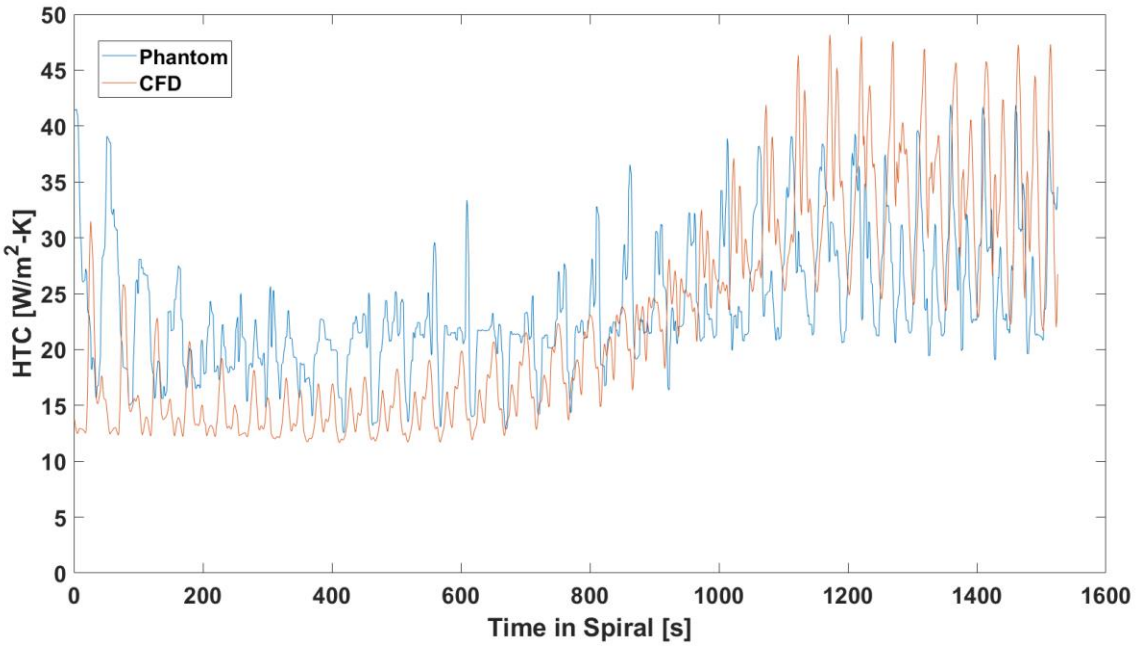

Figure (B.1): Heat transfer coefficient comparison between Phantom and CFD results for Plant 1.

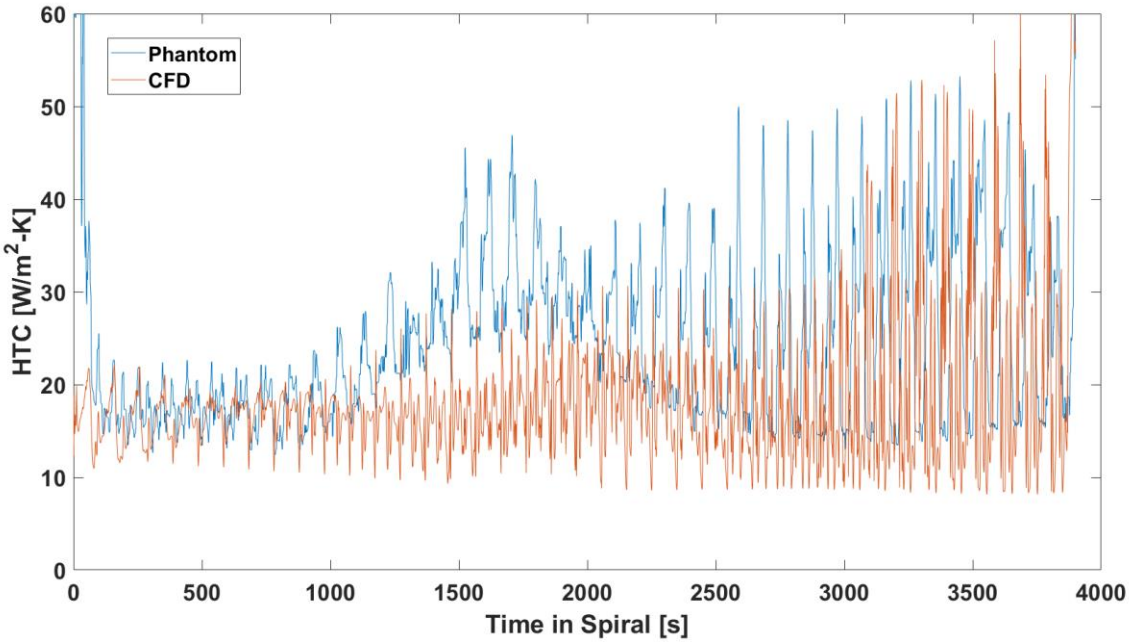

Figure (B.2): Heat transfer coefficient comparison between Phantom and CFD results for Plant 2.

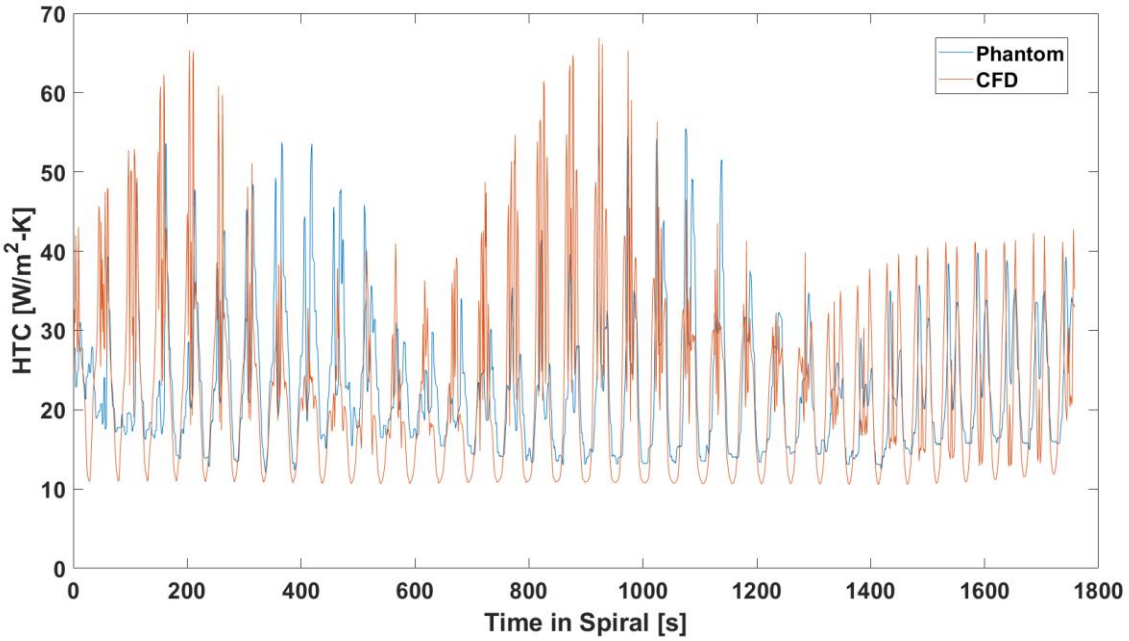

Figure (B.3): Heat transfer coefficient comparison between Phantom and CFD results for Plant 3.

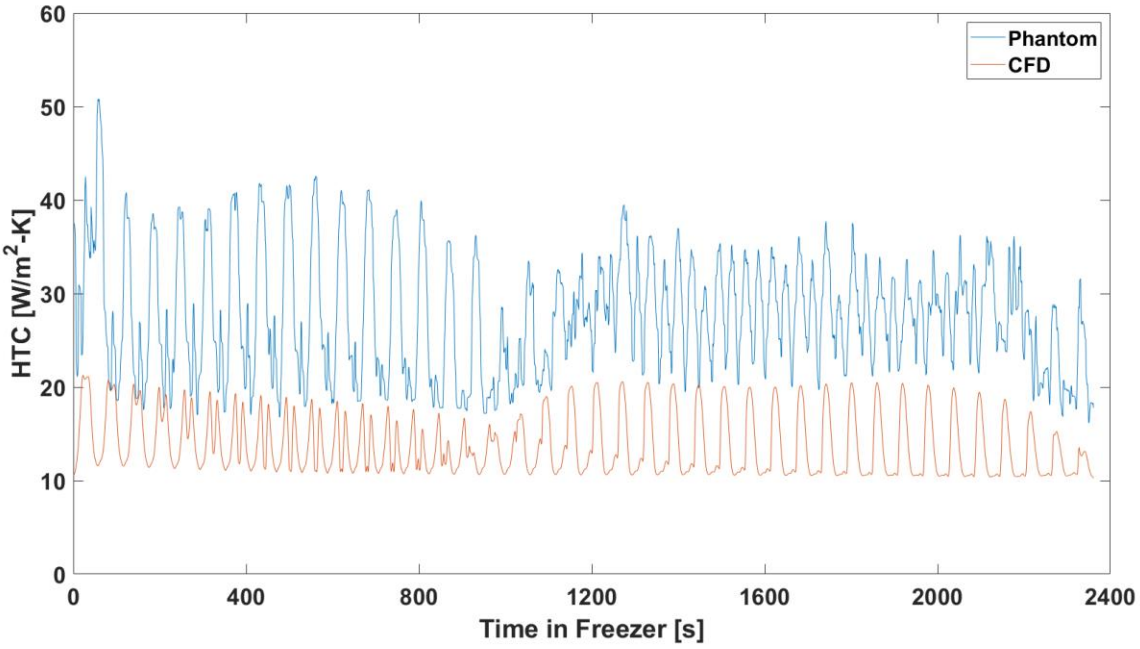

Figure (B.4): Heat transfer coefficient comparison between Phantom and CFD results for Plant 4.